

Medium and Pressure Effects on the Reactivity and Spectra of Iron(II)–diimine Complexes

A Thesis submitted by
Nicholas J. Blundell
for the degree of
Doctor of Philosophy
in the
Faculty of Science
of the
University of Leicester

Department of Chemistry,
The University,
Leicester.
LE1 7RH

February 1991

UMI Number: U038881

All rights reserved

INFORMATION TO ALL USERS

The quality of this reproduction is dependent upon the quality of the copy submitted.

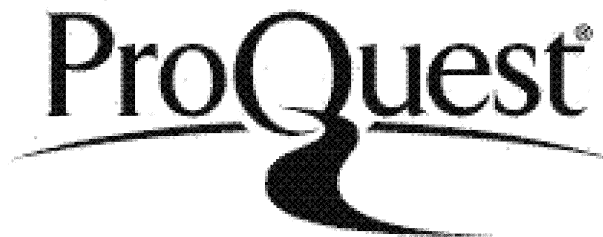
In the unlikely event that the author did not send a complete manuscript and there are missing pages, these will be noted. Also, if material had to be removed, a note will indicate the deletion.



UMI U038881

Published by ProQuest LLC 2015. Copyright in the Dissertation held by the Author.
Microform Edition © ProQuest LLC.

All rights reserved. This work is protected against
unauthorized copying under Title 17, United States Code.



ProQuest LLC
789 East Eisenhower Parkway
P.O. Box 1346
Ann Arbor, MI 48106-1346



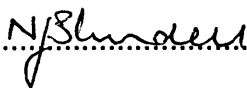
7500732522

X-75-174789X

Statement

This thesis is based upon work conducted by the author, in the Department of Chemistry of the University of Leicester, during the period between October 1987 and September 1990.

All the work in this thesis is original unless otherwise acknowledged in the text or by references. This work is not being presented for any other degree.


.....

Nicholas J. Blundell

University of Leicester

February 1991

Acknowledgements

I am indebted to my supervisor, Dr. J. Burgess, for his continual guidance, encouragement, patience and enthusiasm throughout the period of my research.

I would also like to express my appreciation to Dr C. D. Hubbard, Dr P. Guardado, Dr D.R. Russell and his group, Dr. G. Griffiths, Dr. M. J. Blandamer, to Ann Crane who helped with the preparation of the diagrams, and to Phil Acton for maintaining the spectrophotometers.

In addition, I would also like to thank the members of the Chemistry Department at the University of the West Indies, Jamaica, especially Prof. T.P. Dasgupta, my colleagues and friends here in Leicester, and the Leicester University Computer Centre for the use of their facilities.

I am also very grateful to Lucas Ltd and to the European Community who provided financial support.

Finally, and most of all, I would like to thank my family, for their love and encouragement over the years, and without whom this thesis would never have been possible.

Medium and Pressure Effects on the Reactivity and Spectra of Iron(II)–diimine Complexes

Abstract

Solvation trends of ternary iron(II)–cyanide–diimine complexes in binary aqueous media are examined using spectroscopic and thermodynamic techniques. The observed trends are discussed in terms of the solvent–solute interactions present, and how the relative importance of these interactions varies with the technique and the complex. Crystallographic data for two of these structures are reported and show the effect of the solvate molecules on the structure. Pressure effects on MLCT frequencies are investigated, and the correlation between piezochromic and solvatochromic effects for mono- and binuclear iron(II) and iron(III)–diimine complexes is shown.

Pressure and solvent modification of the rate of oxidation of a series of iron(II)–diimine complexes are interpreted and discussed in terms of the solvation changes that occur upon transition state formation. Complementary partial molar volume data for these complexes are also reported, and combined to form a volume profile for one reactant pair.

The structure of a binuclear iron(II)–diimine complex is examined in the solid state and in solution. Solvation trends in binary aqueous media are reported for this binuclear cation, and comparisons are made with mononuclear iron(II) and cobalt(III), and with binuclear cobalt(III) complexes.

Kinetics of base hydrolysis of several binuclear iron(II)–diimine complexes are discussed in terms of the structural differences between these complexes. The effects of added organic cosolvents on the rate constants for one of these binuclear complexes is also reported. Spectroscopic evidence for a ligand substituted intermediate is found. The structure of such intermediates is discussed with respect to existing data for mononuclear iron(II)–diimine complexes.

Finally, a preliminary chemical and electrochemical redox investigation is made on the most suitable binuclear iron(II)–diimine complex in light of the base hydrolysis reactivity patterns established.

Contents

1	Introduction.	1
1.1	Introduction.	1
2	Experimental and Theoretical.	8
2.1	Introduction.	8
2.2	Preparation of Complexes.	8
2.3	Instrumentation.	9
2.3.1	HP 8451A Diode Array Spectrophotometer.	9
2.3.2	Pye–Unicam SP 8–100 Spectrophotometer.	9
2.3.3	Pye–Unicam SP 1800 Spectrophotometer.	10
2.3.4	Shimadzu UV160 Spectrophotometer.	10
2.3.5	Perkin Elmer 1100B Atomic Absorption Spectrophotometer.	10
2.3.6	Cyclic Voltametry.	11
2.4	High Pressure Apparatus.	11
2.4.1	Piezochromism.	11
2.4.2	Activation Volumes.	11
2.5	Physical Measurements.	16
2.5.1	Solvent Mixtures.	16
2.5.2	Solubilities.	16
2.5.3	First–order Rate Constants.	17
2.6	Transfer Chemical Potentials.	18
2.6.1	Single Ion Assumptions.	19
2.7	Solvent Effects on Reactivity.	20
2.7.1	Principles of the Analysis.	23
2.8	Pressure Effects on Reactivity.	25
2.9	Partial Molar Volumes.	28
2.10	Volume Profiles.	30
3	Structure, Solvation, Solvatochromism and Piezochromism of Ternary Iron(II)–diimine complexes.	31
3.1	Introduction.	31

3.2	Experimental.	33
3.3	Results and Discussion.	35
3.3.1	Solvation.	35
3.3.2	Solvent Sensitivities.	48
3.3.3	Piezochromism.	56
3.3.4	Crystal Structures.	60
3.4	Concluding Remarks.	73
4	Volumes of Activation, Partial Molar Volumes and Solvent Effects Related to the Peroxodisulphate Oxidation of Ternary Iron(II)–diimine Complexes.	75
4.1	Introduction.	75
4.2	Experimental.	77
4.3	Results and Discussion.	79
4.3.1	Volumes of Activation.	79
4.3.2	Partial Molar Volumes.	83
4.3.3	Volume Profile	88
4.3.4	Initial State—Transition State Analysis.	91
4.4	Concluding Remarks.	99
5	Structure and Solvation of Binuclear Iron(II)–diimine Complexes.	101
5.1	Introduction.	101
5.2	Experimental.	104
5.3	Results and Discussion.	106
5.3.1	Crystal Structure.	106
5.3.2	Solution NMR.	113
5.3.3	Metal–metal Interaction.	120
5.3.4	Solvation.	121
6	Reactivity of Binuclear Iron(II)–diimine Complexes.	130
6.1	Introduction.	130
6.2	Experimental.	132
6.3	Results and Discussion.	133
6.3.1	Nucleophilic Attack.	133
6.3.2	Redox Behaviour.	150
7	References	156
A	Crystal Structure Data for $K_2[Fe(CN)_4(en)].3H_2O$.	170
B	Crystal Structure Data for $H[Fe(CN)_4(bipy)].2H_2O$.	174
C	Crystal Structure Data for $[Fe_2(pmk)_3]I_4.3H_2O$.	178

Ligand Abbreviations

apmi	: 1, 2-dimethyl-1-(2-pyridyl)-2-azaethene
bipy	: 2, 2'-bipyridyl
bmi	: 3, 4-dimethyl-2, 5-diazahexa-2, 4-diene
bqdi	: benzoquinonediimine
bpz	: 2, 2'-bipyrimidine
Bcxcage	: tris- μ [(1, 2-cyclohexanedione dioximato)-O:O]-difluoro dibromato(2-)]-N, N ¹ , N ² , N ³ , N ⁴ , N ⁵]
C₃N₃cage	: 5, 6, 14, 15, 20, 21-hexamethyl-1, 3, 4, 7, 8, 10, 12, 13, 16, 17, 19, 22-dodecaazatetracyclo-[8.8.4.1 ^{3,17} .1 ^{8,12}]tetracos-4, 6, 13, 15, 19, 21-hexaene-N ⁴ , N ⁷ , N ¹³ , N ¹⁶ , N ¹⁹ , N ²²
C₃N₃cxcage	: 5, 6, 14, 15, 20, 21-triscyclohexane-1, 3, 4, 7, 8, 10, 12, 13, 16, 17, 19, 22-dodecaazatetracyclo-[8.8.4.1 ^{3,17} .1 ^{8,12}] tetracos-4, 6, 13, 15, 19, 21-hexaene-N ⁴ , N ⁷ , N ¹³ , N ¹⁶ , N ¹⁹ , N ²²
cp	: cyclopenta-1, 3-dienyl
cx	: 1, 2-diaminocyclohexane
cpa	: 1, 2-diamionocyclopentane
en	: 1, 2-diaminoethane
ein	: 1, 4-diazabuta-1, 3-diene
fz	: 3-(2-pyridyl)-5, 6-bis(4-sulphonatophenyl)-1, 2, 4-triazine
gda	: 1, 4-bis(phenyl)-1, 4 diazobuta-1, 3-diene
gmi	: 2, 5-diazahexa-2, 4-diene
hxsbH	: 1, 12-bis(2-pyridyl)-2, 5, 8, 11-tetraazadodeca-1, 11-diene
Me₂bsb	: 1-(2-pyridyl), 1-phenyl, 2-(3, 4-dimethylphenyl)-2-azaethene
ox	: 1,2-ethanedioate
paa	: 1, 4-bis(2-pyridyl)-2, 3-diazabuta-1, 3-diene
pah	: 1, 8-diamino-2, 3, 6, 7-tetramethyl-1, 4, 5, 8-tetrazaocta-

	1, 3, 5, 7-tetraene
phen	: 1, 10-phenanthroline
pbk	: 1, 4-bis(phenyl)bis(2-pyridyl)-2, 3-diazabuta-1, 3-diene
pmk	: 2, 5-bis(2-pyridyl)-3, 4-diazahexa-2, 4-diene
py	: pyridine
pz	: pyrazine
PzMe	: N-methylpyrazinium
terpy	: 2, 2'; 6', 2''-terpyridine
tripod	: tris-[4-(2-pyridyl)-3-aza-3-butenyl]amine

Other Abbreviations

AN	: acceptor number
BBD	: broad-band decoupled
COSY	: correlation spectroscopy
CRT	: cathode-ray tube
DEAE	: diethylaminoethyl
DEPT	: distortionless enhancement by polarisation transfer
DN	: donor number
DSS	: sodium-2, 2-dimethyl-2-silapentane-5-sulphonic acid
EXAFS	: extended x-ray fine structure
IS	: initial state
LMCT	: ligand to metal charge transfer
MLCT	: metal to ligand charge transfer
MMCT	: metal to metal charge transfer
NHE	: normal hydrogen electrode
NOE	: nuclear Overhauser effect
OSET	: outer sphere electron transfer
TBAP	: tetrabutylammoniumphosphate
TLC	: thin-layer chromatography
TS	: transition state
SWAG	: Savage-Wood additivity group

List of Publications

1. N.J.Blundell, J.Burgess, P.M.Cullis, C.D.Hubbard and R.Misra,
J.Am.Chem.Soc., 110, 7 900 (1988) "Evidence for 'Free'
Thiometaphosphate in Aqueous Solution."
2. N.J.Blundell, J.Burgess and C.D.Hubbard, *Inorg.Chim.Acta*, 155, 1
65 (1989). "Volumes of Activation for Peroxodisulphate Oxidation of
Ternary Iron(II) Complexes."
3. M. J. Blandamer, N. J. Blundell, J. Burgess, H. J. Cowles, J. B. F. N.
Engberts, I. M. Horn, and P. Warrick Jnr., *J.Am.Chem.Soc.*, 112, 6854
1990. " Analysis of Solvent Effects on the Kinetics of Reactions in
Solution Using Kirkwood-Buff Integral-functions — Alkaline-hydrolysis
of the Diazabutadiene Complex Tris(glyoxal
bis(methyl-immine))Iron(II) and Spontaneous Hydrolysis of
4-Methoxyphenyl 2,2-Dichloropropionate in Water
(2-Methyl-2-Propanol Mixtures at 298.2 K)."
4. N.J.Blundell and J.Burgess, *Inorg.Chim.Acta*, 173, 5 (1990).
"Solvation and reactivity in the ferrocene — ferricinium electron
exchange reaction."
5. M.J.Blandamer, N.J.Blundell, J.Burgess, H.J.Cowles, I.M.Horn,
J.Chem.Soc., Faraday Trans. I, 86, 283 1990. " Ultrasonic-absorption
Properties and Kirkwood-Buff Integral-functions for Hydrogen-peroxide
Water and Propanone Water Mixtures at 298.2 K."

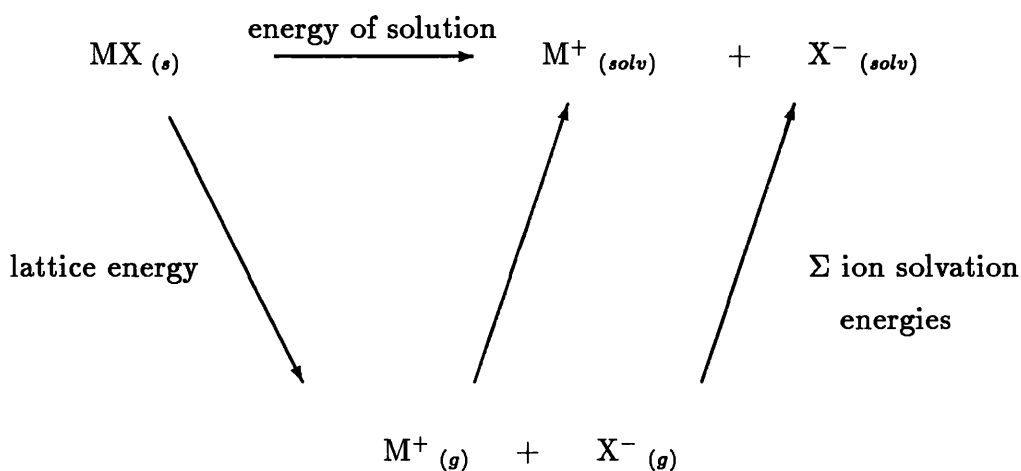
6. M.J.Blandamer, N.J.Blundell, J.Burgess, H.J.Cowles, I.M.Horn,
J.Chem.Soc., Faraday Trans. I, 86, 277 1990. “ An Inverse
Kirkwood–Buff Treatment of the Thermodynamic Properties of DMSO
Water Mixtures and Cyanomethane Water Binary-liquid Mixtures at
298.2 K.”
7. C.Minero, E. Pramauro, E.Pelizzetti, N.J.Blundell, J.Burgess, and
S.Radulovic, *Inorg.Chim.Acta*, 173, 43 1990. “ Hexachloroiridate(IV)
Oxidation of Benzenediols in Binary Aqueous Solvent Mixtures –
Solvation and Reactivity.”
8. accepted for publication in *J.Chem.Soc., Dalton Trans.*, “Partial
molar volumes of ternary iron(II)-cyanide-diimine complexes.”
9. to be submitted to *Inorg.Chem.*, “Structure, solvation and reactivity
of an encapsulated and a binuclear iron(II) complex; ligand effects on
the stereochemistry at a low–spin d^6 centre.”
10. to be submitted to *Inorg.Chim.Acta.*, “ Solvato– and piezochromism
of ternary iron(II)–cyanide–diimine complexes”

Chapter 1

Introduction

1.1 Introduction.

Reactions in solution are fundamentally different from those in the gas phase because of the interactions that occur between solvent and reactant molecules. These interactions can be seen from a simple energy cycle of the type shown below;



The solubility of a solute in a solvent is therefore determined by the energy of solution. This represents the small difference between the large amount of energy required to separate the ions in a crystal lattice and the energy gained when these ions are introduced into solution (solvation energy). It is the nature and strength of these solvation interactions, and how they vary between the gas phase and in solution and between different solvent media, that affects reaction rates and spectra. Some idea of the effect of the reaction environment on rate constants for two different reactions can be seen from Table 1.1.

Thus for N_2O_5 decomposition, there is a factor of about 2 between the rate constant in the gas phase and in organic solvents. In contrast, the ferrocene–ferricinium exchange reaction is some 10^4 times slower in solution than in the gas phase. In addition, it can be seen from Table 1.1 that relative to this large difference in rate constants between the gas phase and in solution, there is a factor of only about 3 in rate constants between the solvent systems.

Reaction	Medium	Rate constant ^a	Ref.
N_2O_5 decomposition		$(10^5 k_1 / \text{s}^{-1})$	
	gas phase	0.79	[1]
	CH_3NO_2	1.35	[2]
	CCl_4	1.83	[2]
$[\text{Fe}(\text{cp})_2]^{0/+}$ exchange		$(10^{-6} k_2 / \text{mol}^{-1} \text{dm}^3 \text{s}^{-1})$	
	gas phase	13000	[3]
	$(\text{CH}_3)_2\text{CO}$	8	[4]
	MeOH	18	[4]
	PhNO_2	30	[4]
	MeCN	9	[4]
	DMSO	9.5	[4]

^a Measured at 298.2 K.

Table 1.1 General view of medium effects on rate constants
between the gas- and liquid-phase.

Since Menschutkin's initial observations ^[5], medium effects on reaction rates have been of interest; since not only do rates vary with solvent, but product distribution and reaction mechanisms have, in some cases been shown to be solvent dependent ^[6-10]. The data given in Table 1.2 give a general view of the scale of solvent modification of rate constants for a variety of reactions.

Clearly the extent of solvent modification of rate constants depends not only upon the reaction type but also on the solvation of the participating reactants.

Reaction	Solvent	Rate constant ^a	Range ^b	Ref.
t-BuCl solvolysis		(10 ⁵ k ₁ / s ⁻¹)		[11]
	water	3300	>10 ⁶	
	methanol	0.082		
	ethanol	0.009		
Menschutkin :		(10 ⁵ k ₂ / dm ³ mol ⁻¹ s ⁻¹)		[12]
		(373 K)		
Et ₃ N + EtI	nitrobenzene	1380	10 ⁴	
	acetone	265		
	hexane	0.5		
Me ₄ Sn + Br ₂		(10 ³ k ₂ / dm ³ mol ⁻¹ s ⁻¹)		[13]
	acetic acid	9600	5 x 10 ⁴	
	chlorobenzene	117		
	carbon tetrachloride	0.18		
<i>trans</i> - [PtCl ₂ (pip) ₂] + thiourea		(10 ³ k ₂ / dm ³ mol ⁻¹ s ⁻¹)		[14]
	acetone	10600	22	
	methanol	3800		
	dimethyl sulphoxide	480		

^a 298.2 K unless otherwise stated.

^b Value quoted covers all of rate constants cited in the relevant reference.

Table 1.2 General view of solvent effects on rate constants.

The analysis of such dramatic changes in reaction rates has been successfully achieved using the initial state–transition state approach (Section 2.6) for a wide variety of reaction types.

The dissection of the solvent effects into the component effects on the initial– and transition–states has given considerable insight not only into the role of solvation in determining reaction rates, but also to a lesser extent, to a more detailed understanding of the involvement of solvent molecules in the mechanism. In this latter respect new, more quantitative treatments, such as the SWAG approach ^[15,16], or that developed by Kirkwood and Buff ^[17] have considerably more potential ^[18].

In contrast to what can be extremely large medium effects on reactivity, pressure effects are in general considerably smaller. Differences in rate constants of only about a factor of 2 or 3 occur within the pressure window of currently available equipment ^[19]. This corresponds to activation volumes generally lying in the range -30 to $+30$ cm³ mol⁻¹. The largest activation volume so far recorded is $+60$ cm³ mol⁻¹, where the rate constant changed by a factor of ca. 6 up to 1 kbar ^[20].

The activation volume (derived from the pressure dependence of the rate constant) can also give one considerable insight into either the reaction mechanism, or the changes in solvation of the reactants on reaching the transition state for a particular reaction. In many ways it provides a complementary view of a reaction to the IS/TS analysis mentioned above.

Solvent and pressure changes can also alter the energetics of photodriven intramolecular electron transfer processes (solvato– and piezo–chromism respectively). Such changes alter charge distribution within the structure and can consequently alter physical properties such as oxidation state stability (redox po-

tentials) and chemical reactivity. Examples of the latter include the photosubstitution reaction mechanisms in the $[\text{Rh}(\text{NH}_3)_5\text{Cl}]^{2+}$ ^[21,22] and $[\text{W}(\text{CO})_5(\text{py})]$ complexes ^[23].

Recently, several different research areas seem to be converging. Firstly, links between solvato- and piezo-chromism of mononuclear MLCT/LMCT and polynuclear MMCT processes are being explored ^[24]. This so-called solvent and pressure tuning of the mixed valence state has been primarily for binuclear complexes ^[25,26]. Secondly, the delocalisation in mixed valence trinuclear complexes has been shown to be dependent on temperature ^[27] and on the dynamics of the solvate molecules ^[28,29]. Indeed this seems to be an area of converging interest with pressure induced phase transition in crystal lattices ^[30].

The work involved in this Thesis involves the effects of solvent and pressure on the spectra and reactivity of, primarily, iron(II)-diimine complexes.

Chapter 3 examines the solvation of a series of these iron(II) complexes in mixed solvents by thermodynamic and spectroscopic methods. Comparisons between the results obtained by the two methods used highlight the importance of specific solvent effects for these complexes, which are illustrated further in single crystal structure determinations. Finally, pressure and solvent effects on the MLCT spectra of these compounds are measured and discussed in terms of the metal-ligand bonding, and compared with MMCT transitions.

The following Chapter explores pressure and solvent effects on the kinetics of peroxodisulphate oxidation of these iron(II) complexes. Activation and partial molar volume data and IS/TS analyses are reported and discussed in terms of the solvation changes that occur during the reaction and the possible mechanistic implications.

The last two chapters involve binuclear iron(II) complexes. Chapter 5 ex-

amines the structure of one of these binuclear complexes in the solid state by single crystal structure determination, and in solution by ^1H and ^{13}C nmr spectroscopy. The final Chapter reports the reactivity of several binuclear complexes. On the basis of these results, the redox chemistry of suitable candidates is explored electrochemically to determine the possibility of forming mixed valence complexes.

Chapter 2

Experimental and Theoretical

2.1 Introduction.

This Chapter describes briefly the experimental and theoretical details required to collect and analyse much of the data recorded in this thesis.

2.2 Preparation of Complexes.

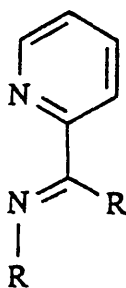
The vast majority of complexes used in this thesis are low spin iron(II) containing the bidentate diimine unit (1), and involve ligands of aliphatic, semi aromatic, and aromatic character (2)→(4) respectively;



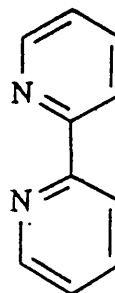
1



2



3



4

The synthesis of such Schiff-base ligands (2 → 3) involves the reaction of the appropriate primary amine and either a ketone or aldehyde *via* the following reaction;



More detailed preparations of the individual complexes are integrated into the experimental section of the relevant Chapters.

2.3 Instrumentation.

2.3.1 HP 8451A Diode Array Spectrophotometer.

This is a single beam instrument with a wavelength range of 190 nm to 820 nm. A temperature probe is embedded into the block and connected via a temperature control unit to a digital display unit.

The instrument is controlled by two microcomputers; the Z80 which controls the internal hardware of the instrument and the HP85A which deals with the data and acts as an interface between the user and the spectrophotometer.

The instrument is capable of recording absorbance readings at up to 0.1 s intervals. The software and more detailed operational information are described elsewhere ^[31].

2.3.2 Pye–Unicam SP 8–100 Spectrophotometer.

The instrument is capable of measuring absorbances from 0.000 to 2.000 (± 0.001) over the wavelength range 200 nm to 800 nm. The four-cell block holder is thermostatically controlled by circulating water from a built in temperature controller. The temperature is monitored by a platinum resistance thermometer placed in the cell holder, which gives a digital display (± 0.1 K).

In addition, the cell holder can be removed, and replaced with the high-pressure cell described in more detail in Section 2.4.1. This then enables spectra to be recorded at high pressures.

2.3.3 Pye–Unicam SP 1800 Spectrophotometer.

The SP–1800 is a double beam instrument operating in the UV/visible region over the range 190 to 820 nm. It is capable of monitoring 3 sample and 3 reference cells simultaneously. The instrument is interfaced to an IBM PC. The software was developed by Dr. M. J. Blandamer, and is described elsewhere [32].

2.3.4 Shimadzu UV160 Spectrophotometer.

This is a microcomputer–controlled double beam recording spectrophotometer consisting of a monochromator, keyboard, screen and thermal printer. It is capable of measuring absorbances from 0.000 to 2.500 (± 0.002) over a range of 200 nm to 1100 nm (± 0.5 nm). Incorporated within the hardware are routines enabling peak picking, spectral manipulation, repeat scan spectra, and data storage.

2.3.5 Perkin Elmer 1100B Atomic Absorption Spectrophotometer.

This is a microcomputer–controlled single beam atomic absorption/emission spectrophotometer with a CRT screen and keyboard. The control of the photomultiplier gain, lamp current, signal processing, and data processing are automatic. The spectrophotometer is capable of operating with either a graphite furnace or a flame to effect atomisation. All work undertaken in this Thesis involved the use of an air/acetylene flame following the manufacturer's recommendations [33].

2.3.6 Cyclic Voltametry.

This consisted of a PAR174 polarographic analyser coupled to a PAR programmer unit controlling the sweep width and the scan rate. The equipment was able to scan between -2.5 V and $+2.5$ V with scan rates of between 50 mV s^{-1} to 200 mV s^{-1} . Output from the analyser was obtained on a X-Y recorder.

The electrochemical cell consisted of a 10 ml glass cell fitted with a teflon stopper in which were apertures for the various electrodes (a platinum disk working electrode, a platinum wire auxiliary, and a calomel reference electrode).

TBAP (tetrabutylammoniumphosphate) was used as the supporting electrolyte for all of the experiments conducted in this Thesis.

2.4 High Pressure Apparatus.

2.4.1 Piezochromism.

This consists of a high pressure cell (Figure 2.1) located in the SP 8-100 spectrophotometer. The application of pressure into the cell was achieved using a modified KBr press (Figure 2.2) as described previously ^[34], and was capable of producing pressures up to 1 kbar.

A hollow closely fitting brass jacket was connected into the thermostating system of the spectrophotometer, with a platinum resistance thermometer located inside the cell connected to the spectrophotometer's digital display unit.

2.4.2 Activation Volumes.

The apparatus is based on a design by Prof. D. R. Stranks and was manufactured within the department. The high pressure cell consists essentially of a

thermostatted ‘bomb’ which sits in a water bath maintained at 298.2 K. The cell is pressurised by the transference of pressure from a nitrogen powered hydraulic pump, with water transmitting pressure to the teflon plunger in the cell (Figure 2.3). The pressure in the line is monitored using a high pressure guage, with the pressure maintained by the hydraulic pump (Madan type).

Aliquots of the reaction mixture were withdrawn from the cell. The absorbance of each sample was measured in the SP 8–100 spectrophotometer. More detailed procedures for the operation of the equipment are described elsewhere ^[35].

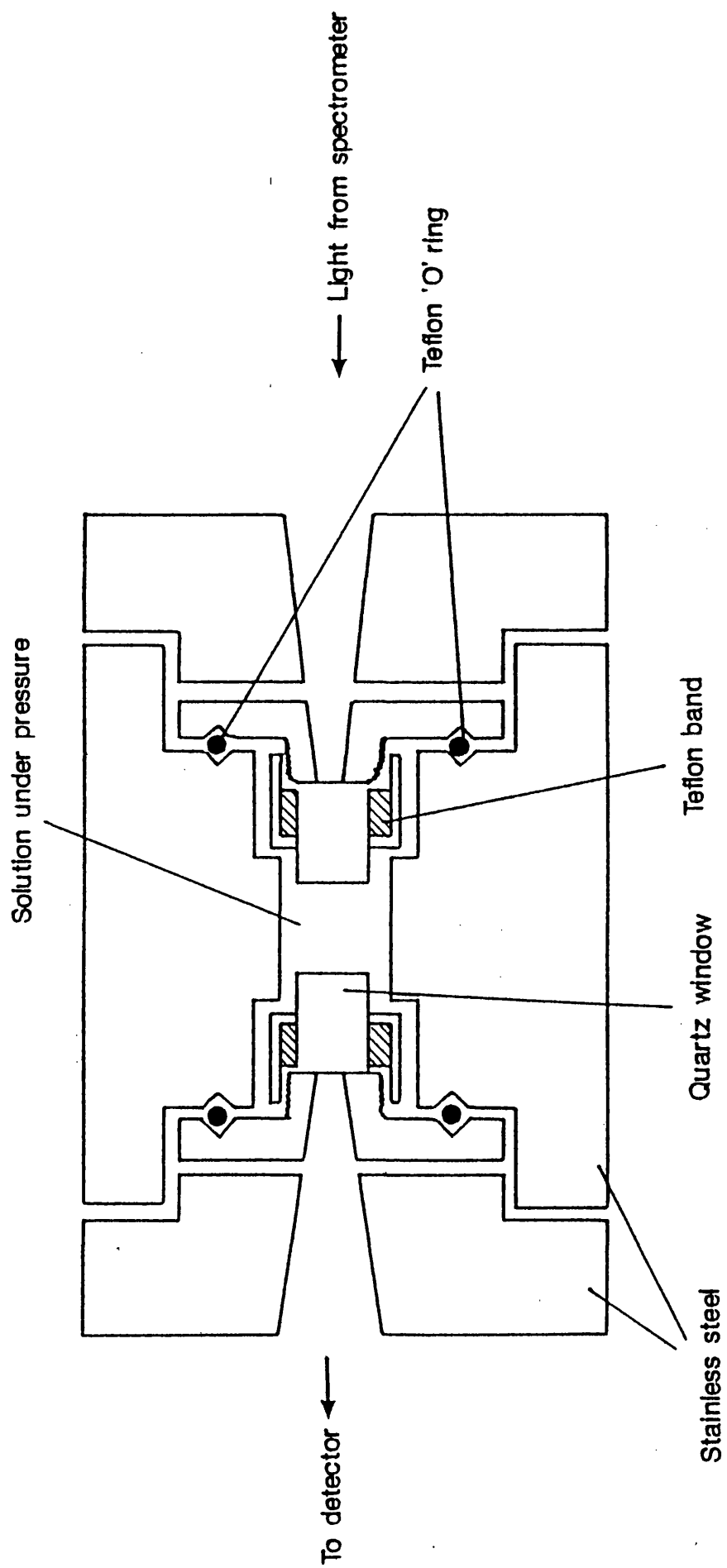


Figure 2.1 High Pressure Cell Unit.

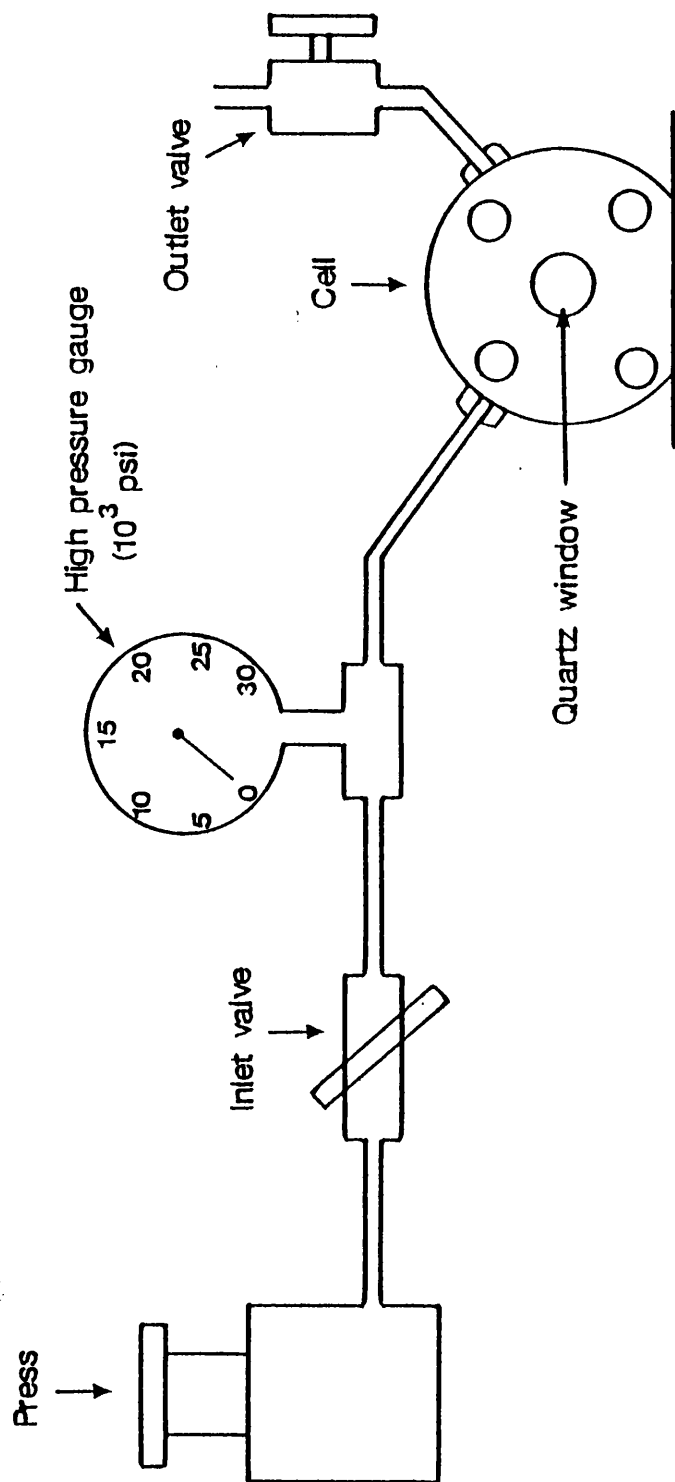


Figure 2.2 Apparatus used to apply pressure to high pressure cell.

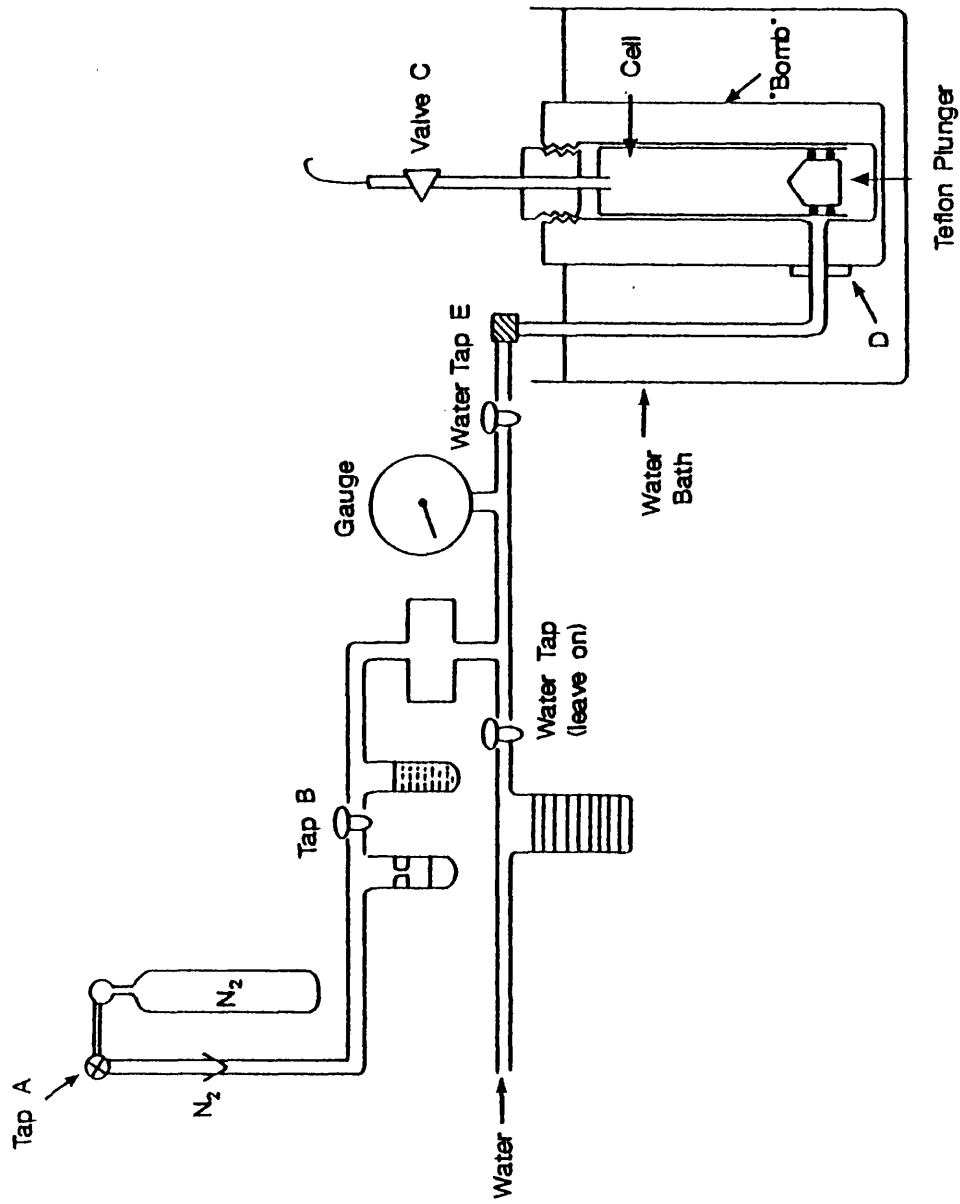


Figure 2.3 Schematic representation of the high pressure apparatus used for the determination of activation volumes.

2.5 Physical Measurements.

2.5.1 Solvent Mixtures.

All solvent mixtures were prepared from reagent grade solvents; with the component solvents dried by conventional methods ^[36]. All mixed solvent compositions are reported as percentage volumes. This refers to the composition (by volume) prior to mixing. All water was de-ionised prior to use.

2.5.2 Solubilities.

Saturated solutions were obtained by vigorously shaking a sealed vessel containing the solvent mixture and a generous excess of the solid. The vessels were then thermostatted in a constant temperature bath maintained at 298.2 K. The samples were left for about 6 hours with periodical shaking to ensure complete saturation. Each sample was then centrifuged to separate undissolved solid from the saturated solution. Subsequently, after filtering through a sinter if necessary, aliquots of the saturated solution were carefully removed from the vessel with a 1 ml bulb pipette. Dilution of the saturated solutions was effected with the respective solvent mixture so that concentrations could be measured by UV/visible spectrophotometry using the Beer–Lambert law and the extinction coefficient of the sample.

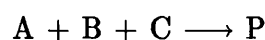
In some cases it was necessary to determine concentrations directly by atomic absorption spectrophotometry. In these cases dilution of the saturated solution was with water. The dilutions were sufficiently large for calibration with the appropriate aqueous standard eliminating the need to prepare metal ion standards in non-aqueous or mixed solvents.

Extinction coefficients were measured by a combination of uv/visible spectrophotometry and either atomic absorption or gravimetric methods. The reported values of concentration and extinction coefficient are the mean of three separate determinations.

It is important to note that all concentrations mentioned in this thesis are on the molar scale and hence, values are expressed in mol dm^{-3} .

2.5.3 First-order Rate Constants.

For a reaction which proceeds to completion such as



the concentration of only a single reactant, A, varies appreciably if all other reactants are present in much larger concentrations, i.e. under first-order conditions.

The change in concentration of reactant A with time can now be expressed as

$$-\frac{d[\text{A}]}{dt} = k[\text{A}]^a$$

where a is the order of the reaction with respect to reactant A, and a first-order dependence occurs when $a = 1$. The rate of reaction varies directly with the concentration of reactant A. Equivalent integrated forms can also be written

$$[\text{A}]_t = [\text{A}]_0 \exp(-kt)$$
$$\ln \frac{[\text{A}]_0}{[\text{A}]_t} = kt$$

where

$[A]_0$ is the initial concentration of A

$[A]_t$ is the concentration of A at time t

and k is the rate constant at the given temperature (T) and pressure (P).

A characteristic quantity of a first-order reaction is the reaction half-life and is the value of t when

$$[A]_t = \frac{[A]_0}{2}$$
$$\text{or } t_{\frac{1}{2}} = \frac{\ln 2}{k}$$

For the bimolecular reactions considered in this thesis, the observed first-order rate constant varies with the concentration of the other reactant, enabling the second-order rate constant to be calculated. All rate constants calculated and quoted in this thesis are, unless labeled otherwise, at 298.2 K.

2.6 Transfer Chemical Potentials.

Consider a pure solid electrolyte in equilibrium with two of its saturated solutions (in media A and B) at the same temperature and pressure. The solubility product, K_{sp} , of the electrolyte in each saturated solution is directly related to ΔG^θ or μ^θ by

$$\Delta G^\theta, \mu^\theta = -RT \ln K_{sp}$$

where μ^θ is the chemical potential, R is the gas constant and T the absolute temperature. The transfer chemical potential between the two media can then be derived as

$$\delta_m \mu^\theta [ML_x]X_n = \mu^\theta (B) [ML_x]X_n - \mu^\theta (A) [ML_x]X_n$$

for an electrolyte $[ML_x]X_n$

$$\delta_m \mu^\theta [\text{ML}_x] \text{X}_n = -RT \ln \left(\frac{K_{sp}(B)}{K_{sp}(A)} \right)$$

or, for an uncharged complex, $[\text{ML}_x]$

$$\delta_m \mu^\theta [\text{ML}_x] = -RT \ln \left(\frac{\text{solubility of } \text{ML}_x \text{ in solvent mixture (B)}}{\text{solubility of } \text{ML}_x \text{ in solvent mixture (A)}} \right)$$

More generally, for an electrolyte consisting of, as here, $(n+1)$ component ions

$$\delta_m \mu^\theta [\text{ML}_x] \text{X}_n = -(n+1) RT \ln \left(\frac{\text{solubility in mixture (B)}}{\text{solubility in mixture (A)}} \right)$$

These solubilities are calculated as described earlier, either directly by atomic absorption spectrophotometry, or by relating the absorbance of the saturated solution to the concentration using the Beer–Lambert law. Therefore, in a more relevant form to this thesis

$$\delta_m \mu^\theta [\text{ML}_x] \text{X}_n = -(n+1) RT \ln \left(\frac{\text{absorbance in mixture (B)}}{\text{absorbance in mixture (A)}} \right)$$

with mixture (A) being pure water and mixture (B) a binary aqueous solvent ($n = 0$ for a non-electrolyte).

For electrolytes an assumption about activity coefficients is required (except when the saturated solutions are very dilute). This is generally that the ratio of activity coefficients for the reference and the mixture is unity.

2.6.1 Single Ion Assumptions.

For electrolytes, the above analysis refers to transfer chemical potentials for the salt $[\text{ML}_x] \text{X}_n$. The separation into the transfer chemical potentials for the component ions $[\text{ML}_x]^{n+}$ and X^- requires the adoption of an extrathermodynamic assumption^[37]. At present, and although other assumptions have been proposed^[38], the TATB is the most generally acceptable^[39]. This is based on the assumption that an anion and cation of similar size, charge, and exterior have similar solvation characteristics, i.e.

$$\delta_m \mu^\theta (\text{Ph}_4\text{As}^+) = \delta_m \mu^\theta (\text{Ph}_4\text{B}^-) = \frac{1}{2} \delta_m \mu^\theta ([\text{Ph}_4\text{As}][\text{BPh}_4])$$

Throughout this thesis the transfer chemical potentials quoted are based on this assumption (or for methanol–water mixtures the closely related TPTB assumption ^[40]).

2.7 Solvent Effects on Reactivity.

In any reaction, the rate constant and the various transition state theory activation parameters (ΔG^\ddagger , ΔH^\ddagger , ΔV^\ddagger , and $T\Delta S^\ddagger$) reflect a barrier between the initial– and transition–state. Solvent effects on a rate constant therefore reflect a composite effect on the initial– and transition–state energies. To separate into these components, thermodynamic transfer parameters (as described in the previous Section) are necessary, since they describe changes in the Gibbs free energy of the initial state. In combination with rate constant changes (reflecting changes in ΔG^\ddagger), an initial–state transition–state dissection is possible. This is shown in Figure 2.4, with several of the possibilities that can arise from such an analysis illustrated in Figure 2.5.

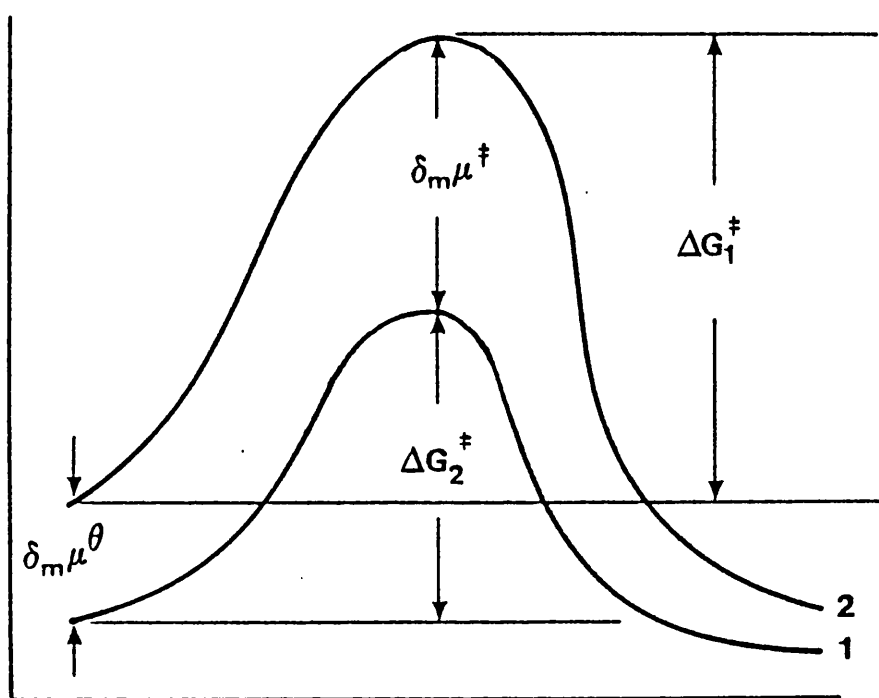
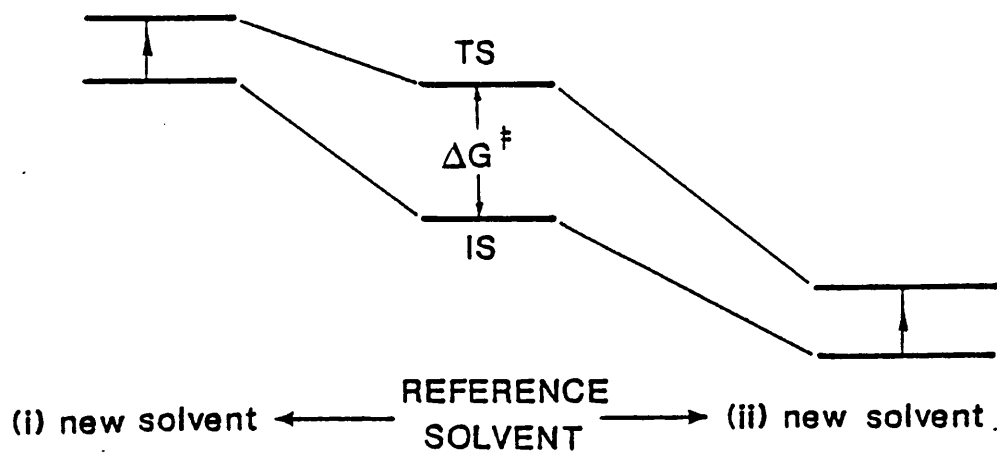


Figure 2.4 Representation of the solvent modification of the initial- and transition-state components to the activation barrier.

(a)



(b)

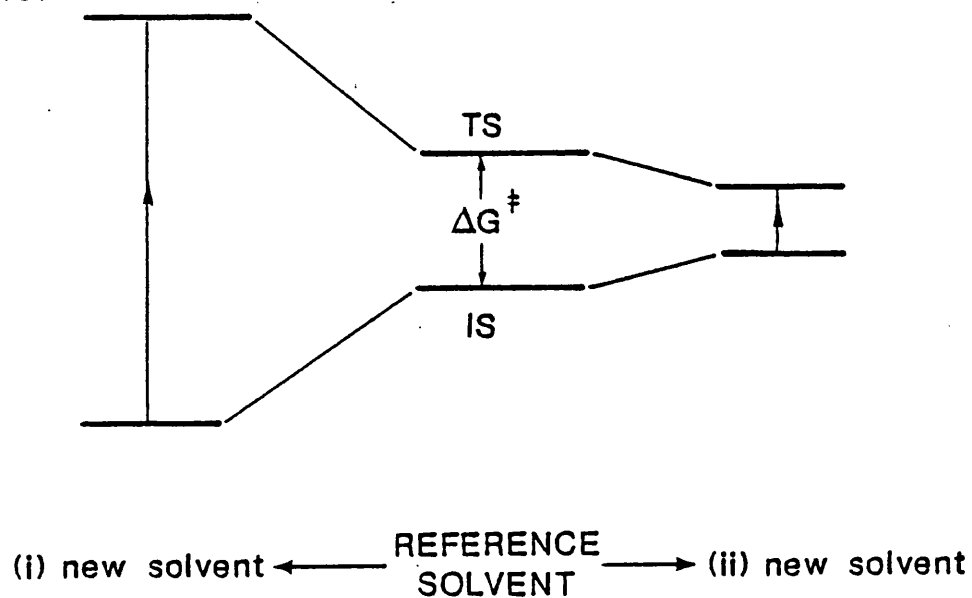


Figure 2.5 Representation of medium effects on the Gibbs free energy of activation, ΔG^\ddagger , for initial and transition states.

If, on changing the medium, the rate constant increases (ΔG^\ddagger decreases) at fixed temperature and pressure, the situation is as shown in Figure 2.5 (a). This can stem from either (1) destabilisation of both states, with the initial state being destabilised to a greater extent, or (2) stabilisation of both states with the transition state being stabilised to a larger extent.

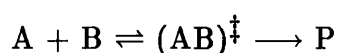
It is also possible for the initial- and transition-states to be affected differently, leading to an increase or decrease in ΔG^\ddagger , Figure 2.5 (b).

Bimolecular reactions are particularly suitable for such an IS/TS analysis since the rates can be adjusted by modification of reactant concentration and the thermodynamic transfer parameters can be measured for the separate reactants.

The calculations required for the initial state have been mentioned already. The calculation for the transition state, derived from the appropriate kinetic data, will be discussed next.

2.7.1 Principles of the Analysis.

For a single stage reaction between reactants A and B, a transition state $(AB)^\ddagger$, and products P



transition state theory provides a link between a rate constant, k_r , (which refers to an irreversible process) and ΔG^\ddagger (which can be treated using the principles of reversible thermodynamics) at fixed temperature (T) and pressure (P);

$$k_r = \frac{kT}{h} \exp\left(\frac{-\Delta G^\ddagger}{RT}\right)$$

where k and h are Boltzmann's and Planck's constants respectively.

If the solvent is a mixture of composition x_2 , then $\Delta G^\ddagger(x_2)$ is given by

$$\Delta G^\ddagger(x_2) = \mu^\ddagger - [\mu_{(A)}^\theta] + [\mu_{(B)}^\theta]$$

where $\mu_{(A)}^\theta$ and $\mu_{(B)}^\theta$ are the standard chemical potentials of reactants A and B, with their sum making up that of the initial state. Also, the standard chemical potential of the transition state is μ^\ddagger . Hence, $\Delta G^\ddagger(x_2)$ is given by the difference between the chemical potentials of the transition and initial states in their respective standard states; i.e. if the rate is expressed in $\text{dm}^3 \text{mol}^{-1} \text{s}^{-1}$, the relevant standard state is that where the concentration is 1.0mol dm^{-3} and the corresponding activity coefficient is unity. This relationship is more conveniently rewritten with the inclusion of a solvent operator δ_m (to avoid confusion) ^[41] so that

$$\delta_m \Delta G^\ddagger = \Delta G_{(2)}^\ddagger - \Delta G_{(1)}^\ddagger$$

and, from above,

$$\delta_m \Delta G^\ddagger = -RT \ln \left(\frac{k_{(2)}}{k_{(1)}} \right)$$

where $k_{(1)}$ and $k_{(2)}$ are rate constants in media (1) and (2) respectively.

2.8 Pressure Effects on Reactivity.

From fundamental thermodynamics, the first differential of the Gibbs free energy with respect to pressure (at constant temperature) is related to the volume

$$\left(\frac{\partial G}{\partial P}\right)_T = V$$

The determination of the volume of activation for a reaction is obtained from the pressure dependence of the rate of reaction via the transition state theory formalism (and hence the Gibbs free energy of activation, ΔG^\ddagger).

$$\Delta G^\ddagger = -RT \ln \left(\frac{kNh}{RT} \right)$$

to give

$$\Delta V^\ddagger = -RT \left(\frac{\partial \ln k}{\partial P} \right)_T$$

The activation volume reflects the change in volume of the reactants on reaching the transition state, i.e. , the difference between the partial molar volume of the initial- and transition-state ($\bar{V}_{TS} - \bar{V}_{IS}$).

The experimental ΔV^\ddagger value is however a composite quantity consisting of intrinsic and solvation components. A schematic representation of these components for a typical bond formation or bond cleavage process, during which partial charge neutralisation or creation can occur, is shown in Figure 2.6. For reactions in which no major solvational changes occur in the activation process one can estimate activation volumes in a relatively straightforward manner. Typical estimates for a variety of processes are given in Table 2.1 ^[42].

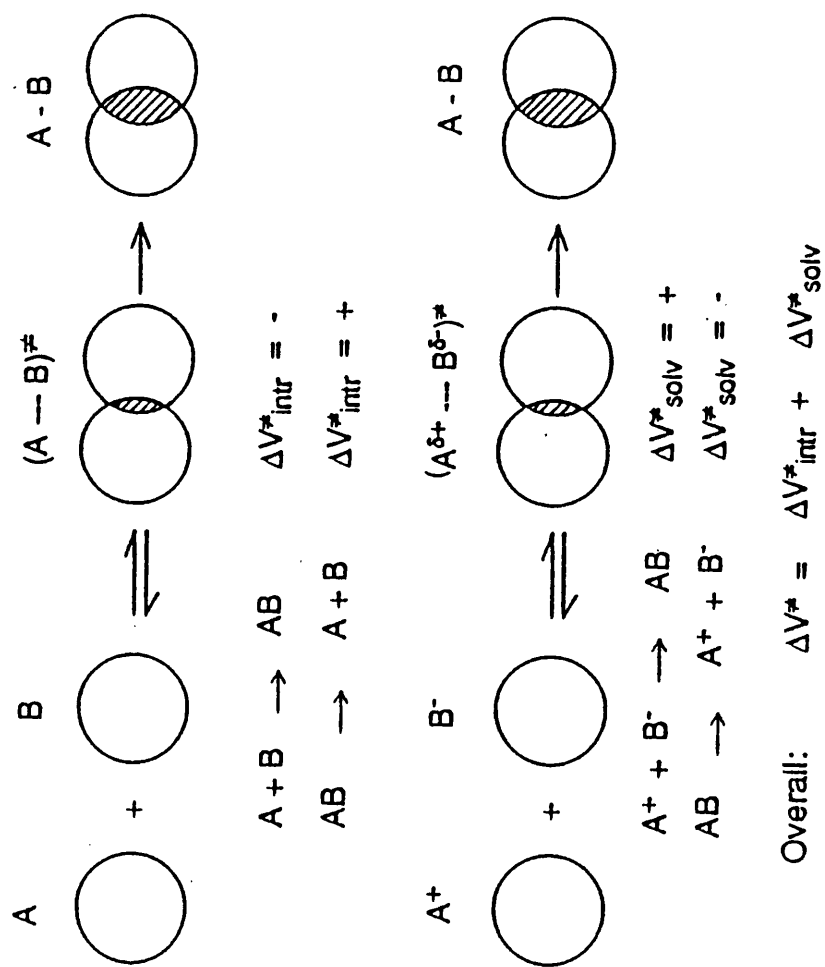


Figure 2.6 Representation of the components of the activation volume.

Mechanistic feature	Contribution to ΔV^\ddagger (cm ³ mol ⁻¹)
bond cleavage	+10
bond deformation	0
bond formation	-10
cyclisation	0
ionisation	-20
neutralisation	+20
charge dispersal	+5
charge concentration	-5

Table 2.1 ΔV^\ddagger estimates for a variety of reaction types.

The decrease in intrinsic reactant volume (reflecting changes in bond lengths and angles on transition state formation) has therefore been estimated to be in the region of $-10 \text{ cm}^3 \text{ mol}^{-1}$ and $+10 \text{ cm}^3 \text{ mol}^{-1}$ for associative and dissociative reactions respectively ^[43]. These estimates refer to organic reactions. Estimates for inorganic reactions are slightly more complicated ^[44]. An estimate for ΔV_{int}^\ddagger for bond formation between 2 spheres of radius 3 Å of ca. $-12 \text{ cm}^3 \text{ mol}^{-1}$ has however been reported ^[45]. For reactions in which charge is diminished (or delocalised), electrostricted solvent is released from the solvation shells of the participating reactants resulting in a positive contribution to the ΔV_{obs}^\ddagger value. In some cases the solvation term can be much larger than the intrinsic term

and positive ΔV_{obs}^\ddagger values are found.

Thus, for base hydrolysis or cyanide attack at low-spin iron(II)–diimine complexes, activation volumes ranging between $+30 \text{ cm}^3 \text{ mol}^{-1}$ in water to close to $-10 \text{ cm}^3 \text{ mol}^{-1}$ in organic-rich binary aqueous solvent media have been interpreted in terms of the release of electrostricted water from the heavily hydrated OH^- and CN^- nucleophiles [46].

Further evidence to support this proposal emerged from similar studies on the nucleophilic substitution of $[\text{Mo}(\text{CO})_4(\text{diimine})]$ complexes. Here, reactions were carried out in media such as toluene and chloroform where the incoming nucleophile was effectively unsolvated. Consequently, activation volumes of around $-10 \text{ cm}^3 \text{ mol}^{-1}$ were obtained [47].

For ease of experimental operation, pressure units are in psi or bar rather than Pascals ($1 \text{ bar} = 14.5 \text{ psi} = 10^5 \text{ Pa}$).

During a typical kinetic experiment the reaction mixture was monitored simultaneously at both atmospheric pressure and under high pressure conditions so that any systematic errors in the activation volume determination were minimised.

2.9 Partial Molar Volumes.

The partial molar volume of a sample (\bar{V}) is defined as the change in volume that occurs when the material is added to an indefinitely large sample of the solution

$$\bar{V}_A = \left(\frac{\partial V}{\partial n_A} \right)_{P, T; n_B}$$

at constant temperature, pressure, and with the number of moles of component B constant.

The magnitude is determined by the intrinsic size (as governed by the respective van der Waals radii) of the constituent atoms and, particularly for a charged species, by electrostriction of the surrounding solvent.

Data for simple inorganic ions ^[48] and a relatively sparse selection of inorganic complexes ^[49–51] exist, particularly in connection with the establishment of activation volumes and volume profiles for substitution ^[52].

Calculation of partial molar volumes involves the extrapolation to zero ionic strength of a plot of density (apparent molar volume) against salt concentration using the Redlich–Mayer equation ^[53].

Solution densities were determined using a vibrating needle densitometer cell (Anton Paar, Model 602), calibrated with air and doubly distilled water.

In an analogous manner to the transfer parameters described in Section 2.6.1, the assignment of single ion values requires the adoption of an extrathermodynamic assumption. The usual convention is to take $\bar{V}(\text{H}^+)$ as zero ^[48]. If however comparisons between anion and cation volumes are to be made then an estimate for the absolute value for $\bar{V}(\text{H}^+)$ is needed. Estimates of between $+5 \text{ cm}^3 \text{ mol}^{-1}$ and $-5 \text{ cm}^3 \text{ mol}^{-1}$ (the value accepted by the majority of authors) have been reported ^[48].

If one uses the TATB assumption mentioned in Section 2.6.1 [and assume that $\bar{V}(\text{AsPh}_4^+) = \bar{V}(\text{BPh}_4^-)$] then $\bar{V}(\text{H}^+) = -11 \text{ cm}^3 \text{ mol}^{-1}$. Such a variety of estimates has led to the adoption of $\bar{V}(\text{H}^+)[\text{conventional}] = \bar{V}(\text{H}^+)[\text{absolute}] = 0 \text{ cm}^3 \text{ mol}^{-1}$ for the values quoted in this Thesis.

2.10 Volume Profiles.

In general, partial molar, reaction, and activation volume data can be combined to construct a reaction volume profile that describes the volume changes that occur along the reaction coordinate. Such a profile gives a pictorial view of the chemical reaction in terms of the volume changes that occur. Unlike the energy profiles mentioned previously, absolute values for initial-, transition-, and product-states can be determined relatively easily. Interpretation of the reaction volume profile allows one to speculate whether the transition state is closer to the initial- or product-state in structure, and can therefore lead to a clearer understanding of the underlying reaction mechanism. Volume profiles for a variety of complex formation, hydrolysis, and substitution reactions have been reported. These, and many organometallic and organic reactions have been extensively reviewed ^[54]. Recent attention has also focused on bioinorganic reactions such as that between vitamin B₁₂ and pyridine ^[55].

Chapter 3

Structure, Solvation, Solvatochromism

and Piezochromism of Ternary

Iron(II)-diimine Complexes

3.1 Introduction.

MLCT (metal to ligand charge transfer) bands are commonly observed when a low-spin d^6 metal is bound to an aromatic heterocycle such as 2,2'-bipyridine [56]. For a given metal the frequency depends on both the σ -donor and π -acceptor abilities of the ligand. The frequencies of the transitions for tris-bidentate complexes such as $[\text{Ru}(\text{bipy})_3]^{2+}$ [57,58] and $[\text{Fe}(\text{bipy})_3]^{2+}$ [59] show very little solvent dependence. In contrast, ternary complexes such as $[\text{M}(\text{CO})_4(\text{bipy})]$ ($\text{M} = \text{Mo}$ [60], Cr [61], W [62]) and $[\text{Fe}(\text{CN})_2(\text{bipy})_2]$ [63] display marked solvatochromic shifts – as well as dependence on such physical parameters as pressure and temperature [64,65]. The direction of these solvato-, piezo-, and thermo-chromic shifts is bathochromic (to lower energy) as the solvent polarity decreases. This direction is a characteristic of the MLCT transitions exhibited by these d^6 complexes, and is the reverse of that for the LMCT in the iron(III) analogues [64].

The magnitude of the shift can conveniently be quantified by introducing a solvent sensitivity scale. Here again, a reference compound is needed, and is selected on the basis of its solubility and sensitivity in as wide a range of solvent media as is possible. Unfortunately, previous studies on the organometallic and the ternary iron complexes used different reference compounds because of the difficulty in finding a single standard whose solubility could encompass solvents as diverse as water and heptane.

For consistency with previous work [66], the $\text{Fe}(\text{CN})_2(\text{bipy})_2$ complex has been used here as an internal standard rather than the $\text{Fe}(\text{CN})_2(\text{phen})_2$ analogue [67]

This solvent dependence provides a spectroscopic agent with which pref-

erential solvation patterns can be compared with trends obtained using other methods such as transfer chemical potentials ^[68].

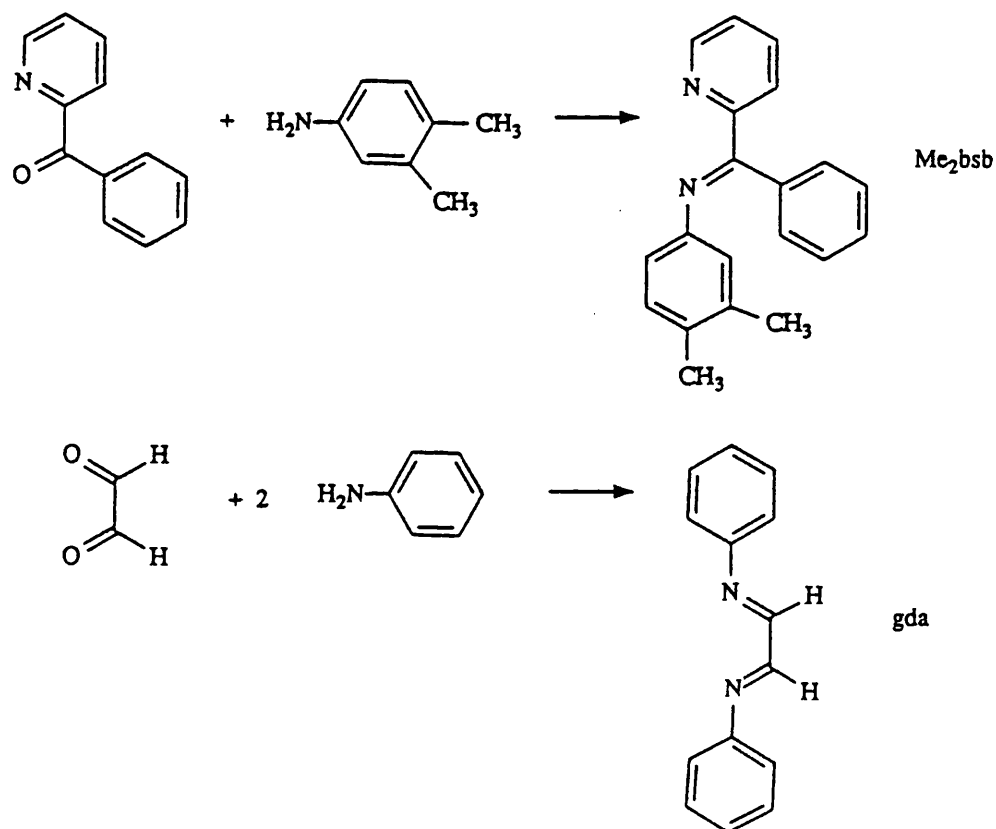
This chapter examines and compares the solvation of a series of ternary iron(II)–cyanide–diimine complexes utilising both of the methods mentioned in the preceeding paragraph. The solvato– and piezo–chromic shifts of these complexes are characterised, and their magnitudes are discussed in terms of the extent of the metal–ligand bonding.

In addition, the X–ray crystallographic structures of the $K_2[Fe(CN)_4(en)] \cdot 3H_2O$ and $H[Fe(CN)_4(bipy)] \cdot 2H_2O$ complexes have been determined. The results are discussed in terms of the effect of oxidation state and solvate interactions on the structural parameters.

3.2 Experimental.

The complexes $K_2[Fe(CN)_4(LL)]$ with $LL = \text{bipy}$ or phen were prepared by Schilt's method ^[69]. The $K_2[Fe(CN)_4(LL)]$ complexes with $LL = \text{ein}$ ^[70] and bqdi ^[71] were prepared by the aerobic oxidation of the respective ternary complexes $K_2[Fe(CN)_4(LL)]$, where LL is ethane-1, 2-diamine and 1, 2-diaminobenzene respectively.

The other ternary complexes $K_2[Fe(CN)_4(LL)]$ were prepared by addition of an excess of KCN to the tris-diimine complexes, each made by the addition of appropriate primary amine and ketone to a solution of $FeCl_2 \cdot 4H_2O$ as shown



Subsequently, the solution volume was reduced by rotary evaporation and any remaining $[\text{Fe}(\text{CN})_2(\text{LL})_2]$ intermediate and free ligand were extracted into CH_2Cl_2 . The aqueous component was rotary evaporated to dryness and removed from the flask. The solid was washed sparingly with methanol – leaving any unreacted KCN in the funnel. The complexes were characterised by their extinction coefficients and their λ_{max} since thermal C, H and N analysis is extremely unreliable for such iron(II)–cyanide complexes ^[72]. Hydration numbers were determined by thermogravimetry.

The transfer chemical potentials were derived from the appropriate solubility measurements as described in Section 2.4.2, except that dilution of the saturated solution was effected with water to eliminate the need to obtain ϵ at each solvent composition.

The frequencies quoted (ν_{MLCT}) were measured on a Shimadzu UV160 spectrophotometer, and are quoted with $\sigma = 50 \text{ cm}^{-1}$. Solvent sensitivities were calculated as the ratio of the shift in ν_{MLCT} for the $[\text{Fe}(\text{CN})_4(\text{LL})]^{2-}$ complexes between water and DMSO, and the corresponding shift for $\text{Fe}(\text{CN})_2(\text{bipy})_2$. This method of calculation was adopted so that any preferential solvation of the participating species did not affect the sensitivity, and also meant that the values obtained here were consistent with those calculated previously ^[66].

Crystal structures were kindly determined by Dr. D. R. Russell and his group. The $\text{K}_2[\text{Fe}(\text{CN})_4(\text{en})] \cdot 3\text{H}_2\text{O}$ crystal was precipitated from a concentrated aqueous solution by the slow addition of acetone. The $\text{H}[\text{Fe}(\text{CN})_4(\text{bipy})] \cdot 2\text{H}_2\text{O}$ crystal was grown slowly from aqueous solution. The X-ray diffraction data for $\text{K}_2[\text{Fe}(\text{CN})_4(\text{en})] \cdot 3\text{H}_2\text{O}$ and $\text{H}[\text{Fe}(\text{CN})_4(\text{bipy})] \cdot 2\text{H}_2\text{O}$ are detailed in Appendices A and B respectively.

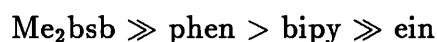
3.3 Results and Discussion.

3.3.1 Solvation.

Transfer Chemical Potentials.

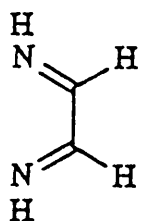
The transfer chemical potentials for a representative selection of ternary iron(II)–cyanide–diimine complexes are given in Table 3.1. Ligand formulae are shown in Scheme 3.1. The importance of charge and ligand periphery in determining solvation patterns can be seen from the trends shown in Figure 3.1. Most striking are the very different solvation trends for the uncharged, and predominantly hydrophobic, $[\text{Fe}(\text{CN})_2(\text{bipy})_2]$ complex and the predominantly hydrophilic $[\text{Fe}(\text{CN})_4(\text{bipy})]^{2-}$ anion. The $[\text{Fe}(\text{CN})_2(\text{bipy})_2]$ complex shows marked preferential solvation by DMSO, with the characteristic minimum for complexes with a mixed hydrophilic and hydrophobic surface ^[73]. This can be rationalised as the sum of cyanide hydration and DMSO solvation of the bipyridyl ligands. It is interesting if one looks at Figure 3.2, that this minimum is considerably less pronounced than for other binary aqueous solvent mixtures.

All the anionic complexes are destabilised as the DMSO content of the solvent mixtures increases underlying the relatively poor anion solvating ability of DMSO and the dominant role played by the charge in determining the solvation trends. Within these trends, the nature of the diimine moiety plays an important, but secondary role. The extent of the hydrophobic diimine–DMSO stabilisation is in line with the hydrophobicity of each individual diimine moiety, ie

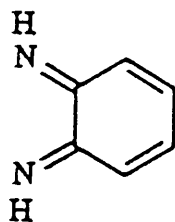


Thus, substitution of Me₂bsb has the effect of inducing a 28 kJ mol⁻¹ stabilisation relative to its bipy analogue even at 60% DMSO. The rather small destabilisation for the [Fe(CN)₄(ein)]²⁻ anion relative to its bipy and phen analogues can be simply ascribed to the very hydrophilic ein moiety being able to retain strongly hydrogen-bonded water molecules in its primary solvation shell – even at modest DMSO concentrations. Similarly, the transfer chemical potentials of the hydrophilic [Fe(CN)₆]³⁻ anion in water–methanol mixtures are interpreted such that the solvation shell of the anion is composed primarily of water even in solutions of high methanol content ^[74].

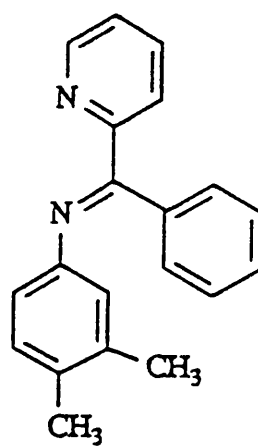
Also included in Figure 3.1 are the transfer chemical potential trends for a selection of cations and anions reproduced from the literature ^[75]. This puts the data for the complexes measured here into context and shows the general distinction between trends for cations and anions.



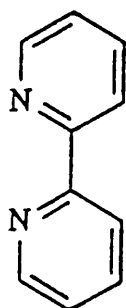
cin



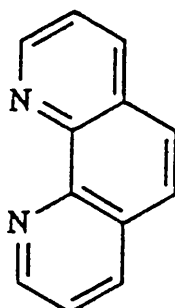
bqdi



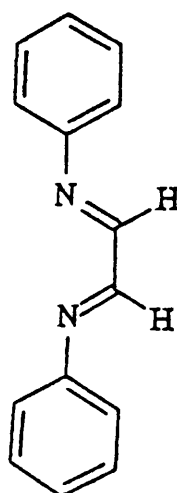
Me₂bsb



bipy



phen



gda

Scheme 3.1 General ligand formulae.

Solvatochromism.

The frequencies of the lowest energy MLCT transition for the ternary iron–cyanide–diimine complexes are reported as a function of solvent composition in Table 3.2, and shown in Figure 3.3. Here again, the importance of the hydrophobic/hydrophilic balance of the ligand periphery can clearly be seen, with the small, predominantly hydrophilic species, $[\text{Fe}(\text{CN})_4(\text{ein})]^{2-}$ and $[\text{Fe}(\text{CN})_4(\text{bqdi})]^{2-}$ exhibiting preferential hydration. In contrast, the much more hydrophobic species, $[\text{Fe}(\text{CN})_4\text{LL}]^{2-}$ (LL = gda, bipy, phen, Me_2bsb) show varying degrees of preferential solvation by DMSO consistent with the relative hydrophobicity of each diimine moiety.

Comparisons between the preferential solvation trends obtained by the two methods are not particularly good, being most satisfactory for the $[\text{Fe}(\text{CN})_4(\text{ein})]^{2-}$ and $[\text{Fe}(\text{CN})_4(\text{bqdi})]^{2-}$ anions.

The two techniques measure fundamentally different processes, the transfer chemical potentials describing an absolute change in the ground state solvation, whereas solvatochromic shifts reflect solvation changes on a difference between a ground– and excited–state. One would expect that for the latter technique, solvation of the ground state would predominate with, due to the Franck–Condon principle, the solvent dipoles frozen in an orientation appropriate to the ground state.

McRae’s equation ^[76] and other similar dielectric cavity models are used extensively in discussions of the origin of solvatochromism ^[77]. Recently, such models have been shown (after reasonable assumptions) to be coherent ^[78], but relevant only for solvent systems where specific solvent–solute interactions, such as hydrogen–bonding, are small or absent. In fact it is still able to deal

satisfactorily only with pure solvents. For systems where specific solvation effects are important, as is the case here, alternative methods are needed.

Correlations have primarily involved the DN ^[79] and AN ^[80] scales. The choice of scale used depends on the nature of the predominant solvent–solute interaction. For systems such as $[\text{Ru}(\text{NH}_3)_5(\text{py})]^{2+}$, where the Lewis acid ability of the solvent molecules is important, correlations against DN are invoked ^[81]. In contrast, AN are used for systems such as $[\text{Fe}(\text{CN})_2(\text{bipy})_2]$ ^[82], which characterise the Lewis base ability of the solvent. Here, hydrogen–bonding can occur to the exposed cyanide (or carbonyl) lone pairs in protic media. Solvents which are less effective at (or incapable of) hydrogen–bonding destabilise the ground state energy (reduce the redox potential) by modulating the $\text{Fe}—\text{C}\equiv\text{N}$ dipole moment. Thus, significant differences in electronic transition energies are found between solvents such as water and DMSO. In addition to this ground state dominated dependence of MLCT (and LMCT) frequency, excited state properties can be dramatically influenced by changes in the medium ^[83–84], and in pH ^[85,86].

Certainly solvent shifts on the MLCT transitions have corresponding changes in the metal–carbonyl and carbon–oxygen frequencies, and nmr shifts of the relevant nuclei (^{13}C and ^{95}Mo) within a series of ternary $\text{Mo}(\text{CO})_4(\text{LL})$ complexes ^[87]. Furthermore, protonation of the cyanides in the $[\text{Fe}(\text{CN})_4(\text{bipy})]^{2-}$ anion ^[88] (which can be considered as the extreme case of hydrogen–bonding) leads to a considerable hypsochromic shift in the charge transfer energy.

Unfortunately, several problems arise when using the empirical scales mentioned above. Firstly, the DN scale is of limited value for aqueous media because of the tendency for the calorimetric empirical standard to decompose ^[89]. Secondly, and most importantly here, these empirical scales do not account for

differences in preferential solvation (although this has not stopped Reichardt's E_T parameter ^[90] being used widely as a solvent polarity indicator for mixed solvents ^[91]). Figures 3.4 and 3.5 show the correlation of the MLCT frequencies for the iron(II) complexes against AN and E_T respectively. Differences in preferential solvation between the ternary iron(II) complexes and the empirical standards are reflected in the curvature of these plots. The correlations against E_T for these complexes are much more satisfactory than those with AN.

Clearly the simple balance between electrostatic and hydrophilic/hydrophobic solvent-solute interactions used to explain the transfer chemical potential trends cannot be used for those obtained by the spectroscopic method. Here cyanide solvation is the dominant factor (*vide supra*), with the diimine hydrophobicity and charge effects playing relatively minor roles. It is interesting therefore that the best correlations between the two solvation techniques occur for the complexes involving the diimine ligands that are most likely to be involved in hydrogen-bonding (i.e. ein and bqdi). Such hydrogen-bonding interactions are discussed in more detail in Section 3.3.4.

% DMSO	0	20	40	60	80	100
$2 \times \delta_m \mu^\theta (\text{K}^+) ^a$	—	-0.6	-3.0	-8.8		-26.2
$[\text{Fe}(\text{CN})_2(\text{bipy})_2]$ $\delta_m \mu^\theta$ (complex)	—	-3.8	-5.6	-8.0	-10.9	-10.2
$\text{K}_2[\text{Fe}(\text{CN})_4(\text{bipy})]$ $\delta_m \mu^\theta$ (salt)	—	+2.6	+13.2	+21.2		+33.8
$\delta_m \mu^\theta$ (anion)		+3.2	+16.2	+30		+60
$\text{K}_2[\text{Fe}(\text{CN})_4(\text{Me}_2\text{bsb})]$ $\delta_m \mu^\theta$ (salt)	—	-0.5	-2.0	-4.7		-2.2
$\delta_m \mu^\theta$ (anion)	—	+0.1	+1.1	+2.0		+28
$\text{K}_2[\text{Fe}(\text{CN})_4(\text{phen})]$ $\delta_m \mu^\theta$ (salt)	—	+1.8	+8.1	+17.8		
$\delta_m \mu^\theta$ (anion)	—	+1.2	+11.2	+25		
$\text{K}_2[\text{Fe}(\text{CN})_4(\text{ein})]$ $\delta_m \mu^\theta$ (salt)	—	+4.1	+7.4	+12.2		
$\delta_m \mu^\theta$ (anion)	—	+4.7	+10.5	+18.9		

^a Taken from reference [92].

Table 3.1 Transfer chemical potentials of ternary iron(II)-cyanide-diimine complexes in DMSO-water mixtures (kJ mol⁻¹; 298.2 K).

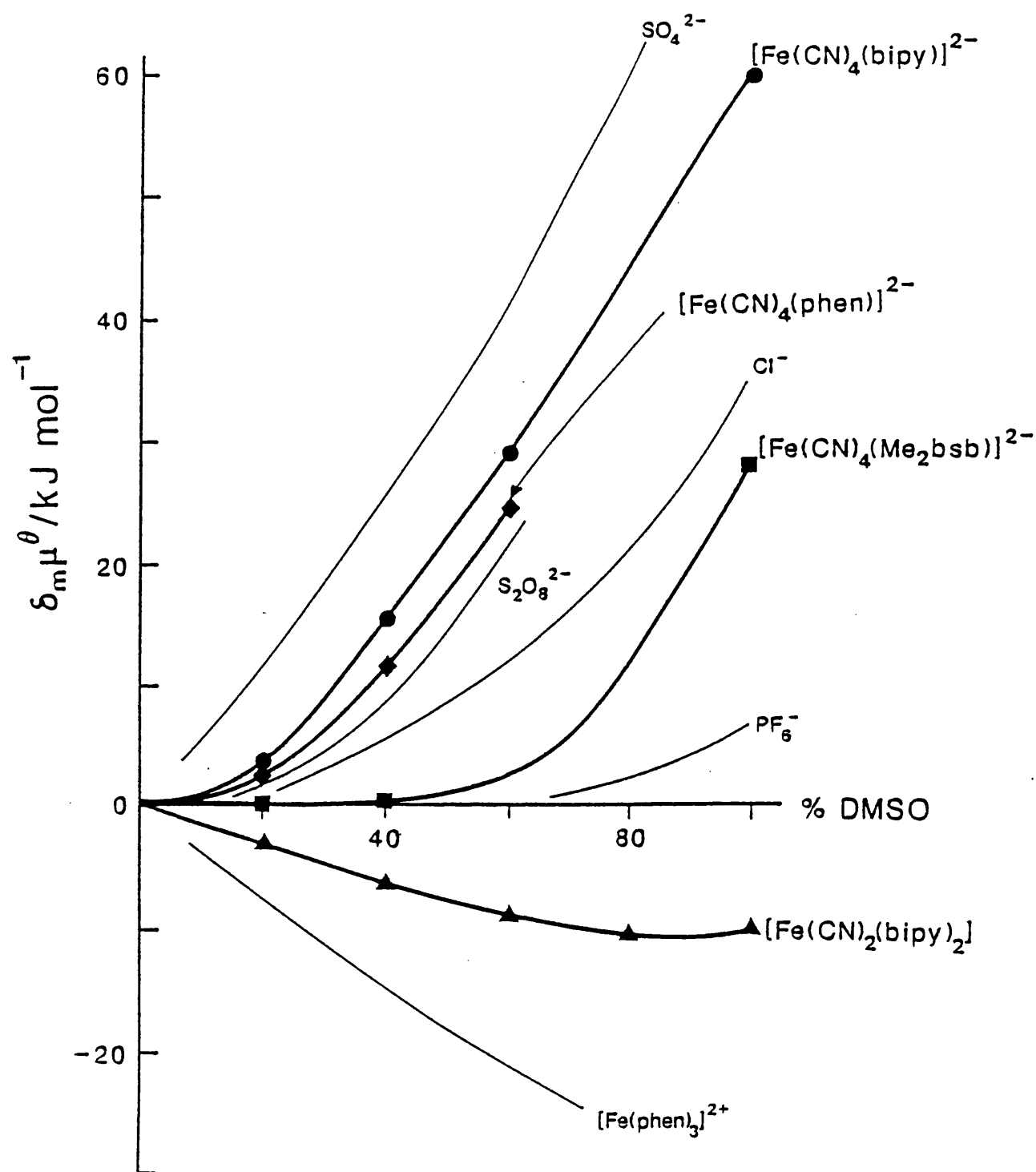


Figure 3.1 Transfer chemical potentials trends of ternary iron(II)-cyanide-diimine complexes in water-DMSO mixtures.

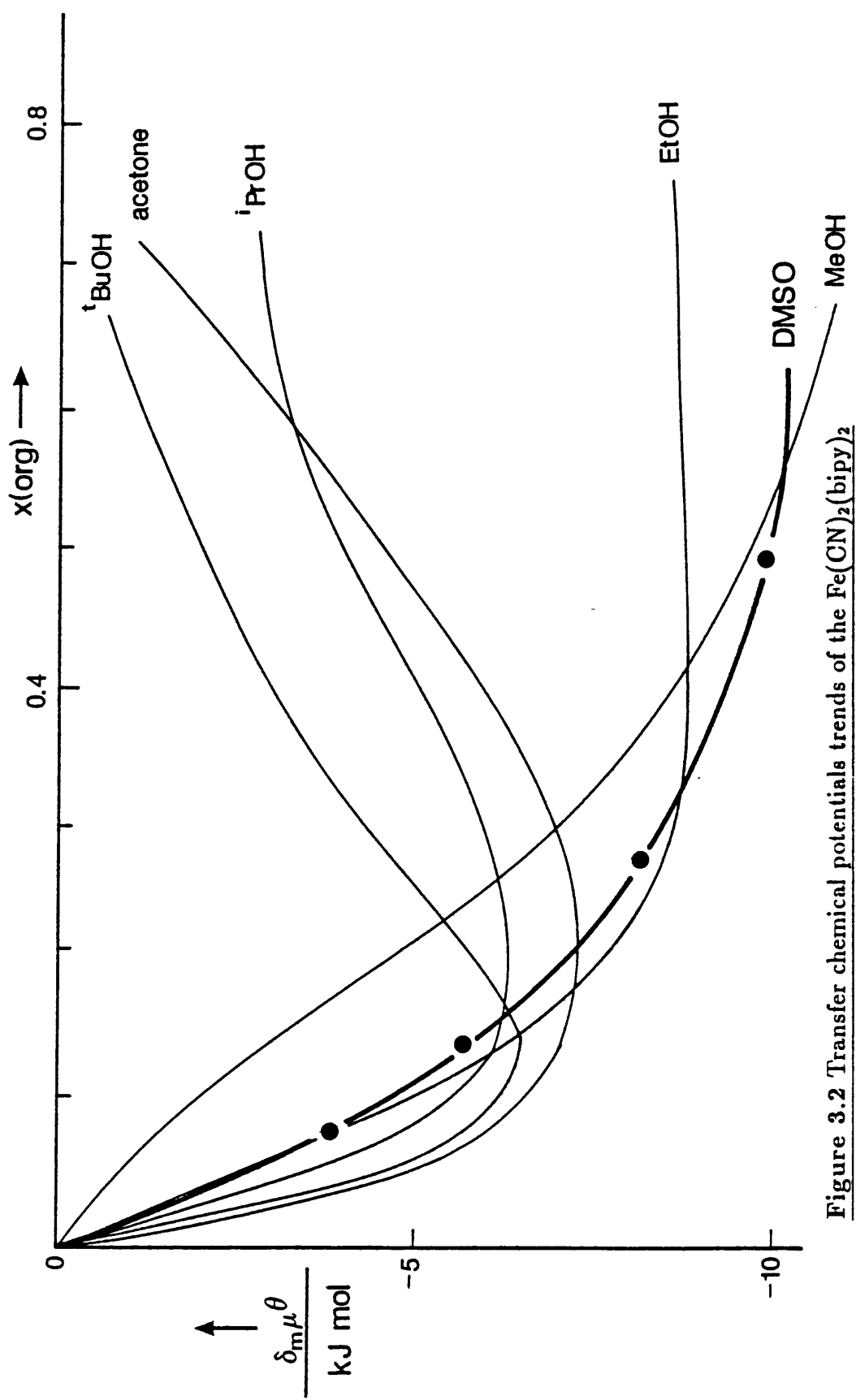


Figure 3.2 Transfer chemical potentials trends of the $\text{Fe}(\text{CN})_2(\text{bipy})_2$ complex in a series of binary aqueous solvent mixtures.

Vol % DMSO	0	20	40	60	80	100
x_{DMSO}	0.000	0.060	0.145	0.276	0.504	1.000
A.N. ^a	54.8	51.3	48.5	44.0	35.9	19.3
E_T ^b	62.8	60.0	57.0	53.7	50.1	45.1
[Fe(CN) ₂ (bipy) ₂]	19267	18762	18248	17730	17094	16287
[Fe(CN) ₄ (ein)] ²⁻	19608	19552	19302	19151	18709	15600
[Fe(CN) ₄ (Me ₂ bsb)] ²⁻	18657	17953	17422	16722	16026	14728
[Fe(CN) ₄ (phen)] ²⁻	21276	20576	19800	18761	17271	14859
[Fe(CN) ₄ (bipy)] ²⁻	20747	19920	19084	18018	16750	14815
[Fe(CN) ₄ (bqdi)] ²⁻	17271	17286	17361	17528	17809	18500
[Fe(CN) ₄ (gda)] ²⁻	17498	17123	16892	16639	16313	16051

^a Taken from ref. [93].

^b Taken from ref. [94].

Table 3.2 ν_{MLCT} of ternary iron(II)–cyanide–diimine complexes
in water–DMSO solvent mixtures.

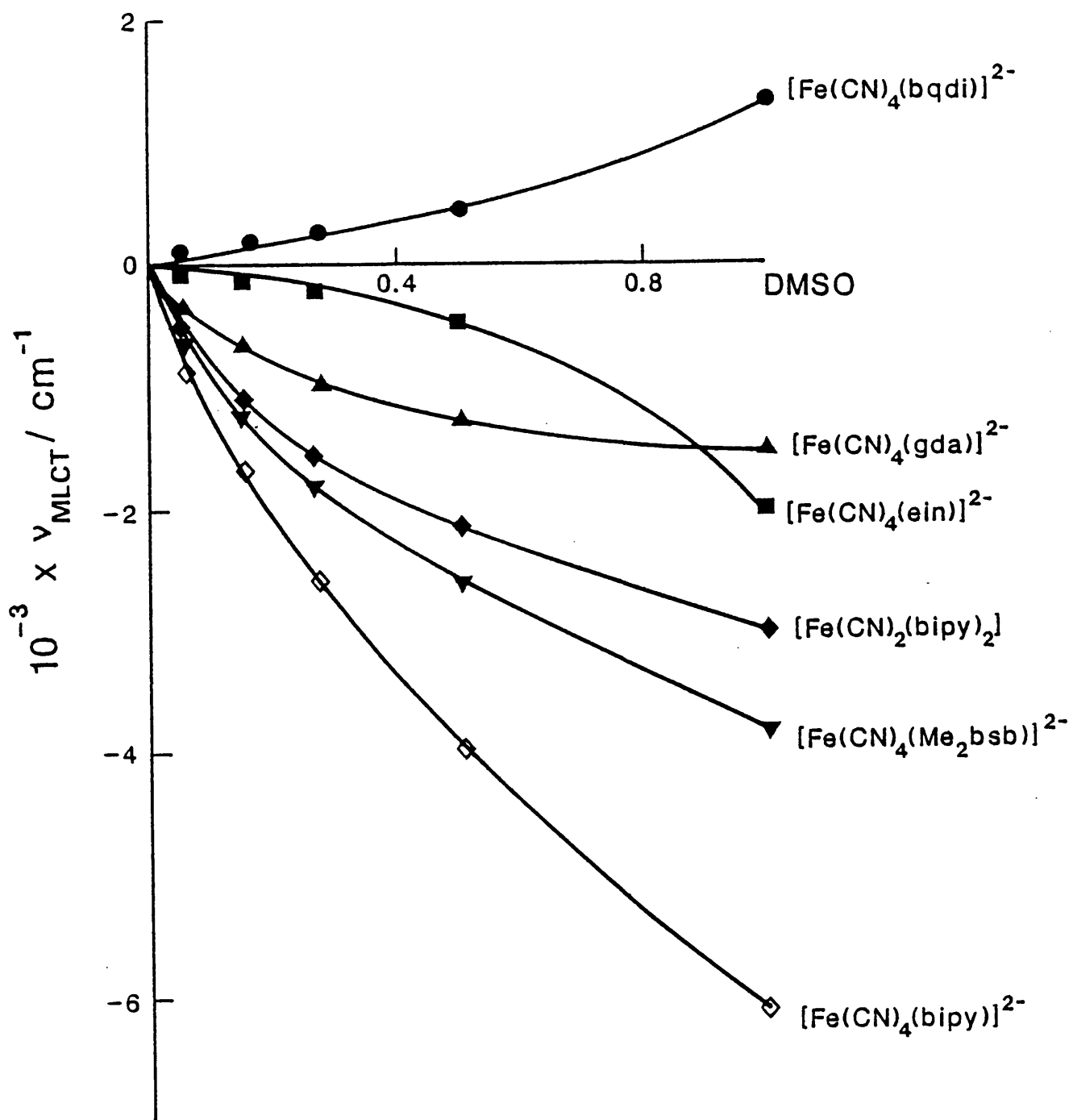


Figure 3.3 Solvatochromic shifts of ternary iron(II)-cyanide-diimine complexes in water-DMSO mixtures.

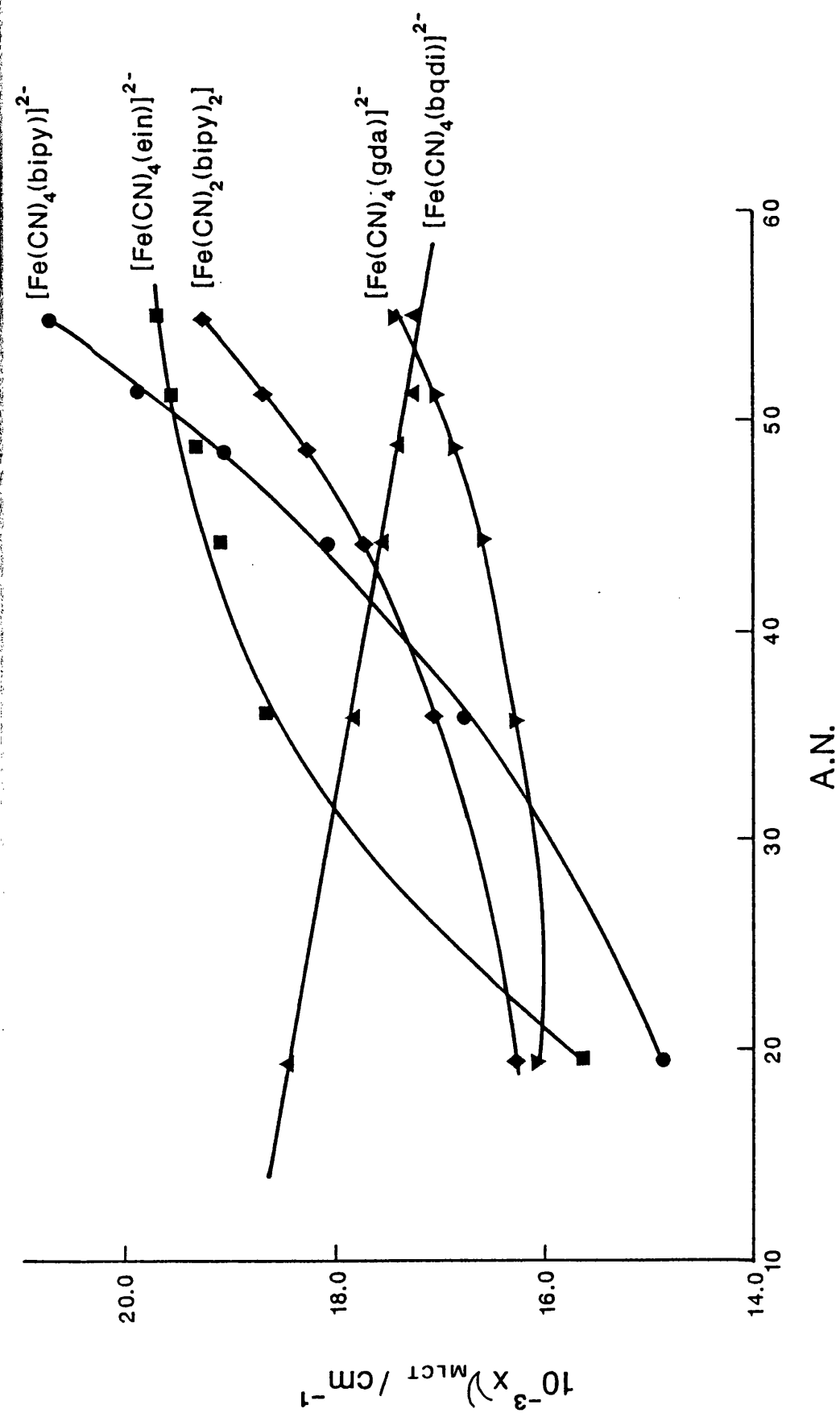


Figure 3.4 Correlation between solvatochromic shifts of ternary iron(II)-cyanide-diimine complexes and AN for water-DMSO mixtures.

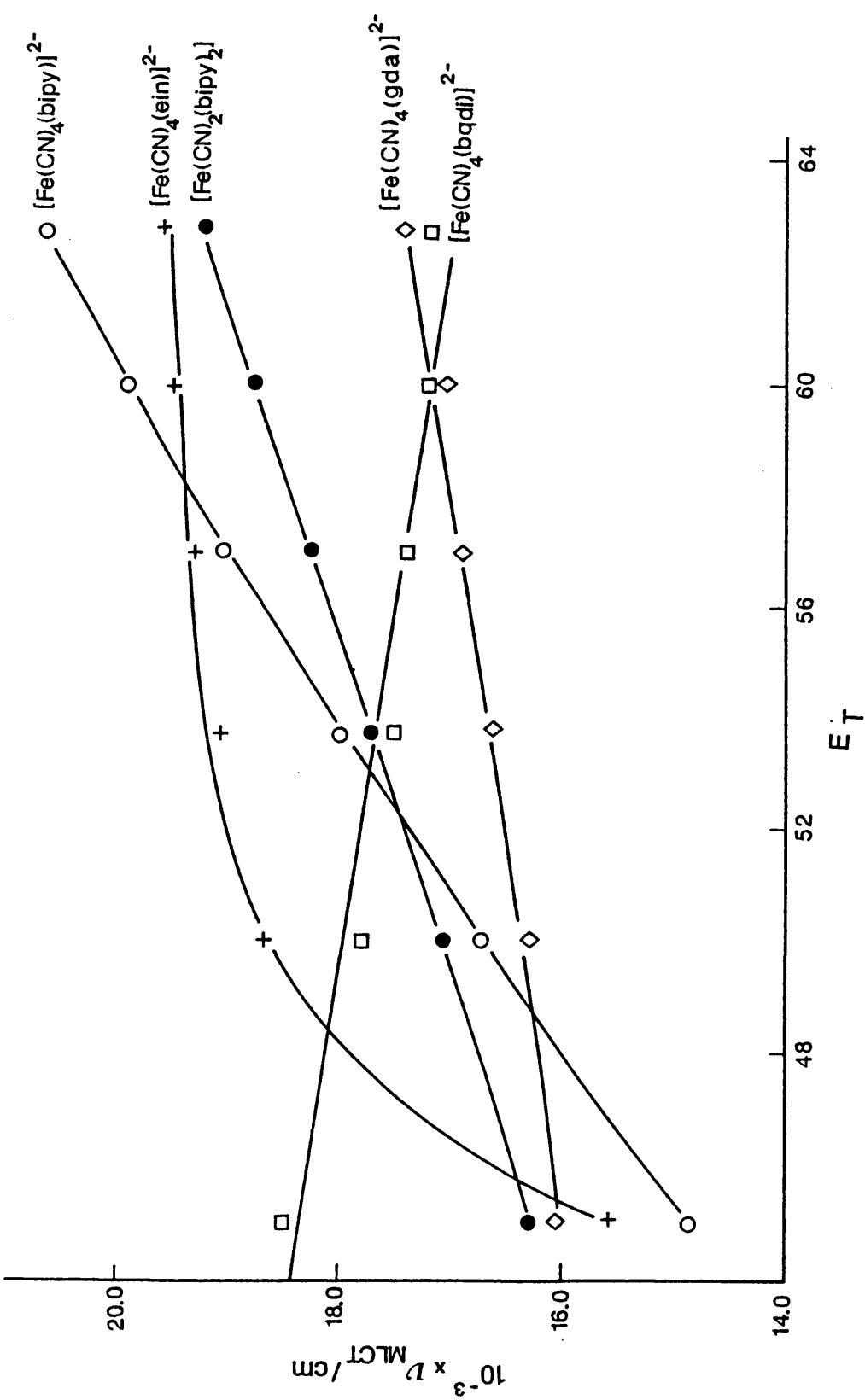


Figure 3.5 Correlation between solvatochromic shifts of ternary iron(II)-cyanide-diimine complexes and E_T for water-DMSO mixtures.

3.3.2 Solvent Sensitivities.

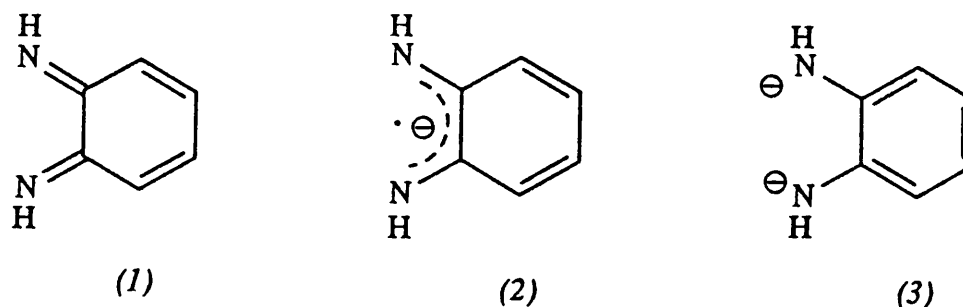
The solvent sensitivities for each compound are reported in Table 3.3, which also includes sensitivities for other ternary iron(II) and iron(III)–cyanide–diimine complexes. Most striking is the anomalous negative sensitivity for the $[\text{Fe}(\text{CN})_4(\text{bqdi})]^{2-}$ anion – consistent with the LMCT transitions in the iron(III) complexes also included in Table 3.3.

Complex	Solvent sensitivity	Ref.
$\text{K}_2[\text{Fe}(\text{CN})_4(\text{ein})]$	1.3	a
$\text{K}_2[\text{Fe}(\text{CN})_4(\text{gda})]$	0.49	a
$\text{K}_2[\text{Fe}(\text{CN})_4(\text{bqdi})]$	−0.41	a
$[\text{Fe}(\text{CN})_2(\text{bipy})_2]$	1.0	a
$\text{K}_2[\text{Fe}(\text{CN})_4(\text{Me}_2\text{bsb})]$	1.3	a
$\text{K}_2[\text{Fe}(\text{CN})_4(\text{bipy})]$	2.0	a
$\text{K}_2[\text{Fe}(\text{CN})_4(\text{phen})]$	2.1	a
$[\text{Fe}(\text{CN})_2(\text{bipy})_2](\text{NO}_3)$	−0.5	[64]
$\text{H}[\text{Fe}(\text{CN})_4(\text{bipy})]$	−1.0	[64]

^a This work.

Table 3.3 Solvent sensitivities for a series of ternary iron(II)
cyanide–diimine complexes (298.2 K).

The bqdi ligand is one of a series of so called 'non-innocent' ligands because of the relative ease of conversion between the different redox forms

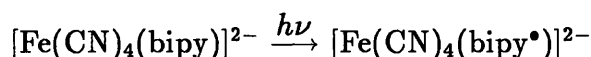


These range from the bqdi diimine unit (1), the radical anion (2), to the dianion of the parent diamine (3). The free bqdi ligand has been postulated to exist in solution ^[95], but only when stabilised (by complexation to a metal) has it been confirmed ^[71]. The possibility of the $[\text{Fe}(\text{CN})_4(\text{bqdi})]^{2-}$ anion existing as an iron(III) atom spin-coupled with a $[\text{C}_6\text{H}_4(\text{NH})_2]^{\bullet-}$ radical (2) was explored, but the single crystal structure confirmed the localised alternating double bond system (1) within the chelate ring ^[71]. The anomalous behaviour must therefore be due to some subtle difference in the molecular orbitals involved in the transition. The 'negative' solvatochromism of the $[\text{Os}(\text{NH}_3)_5(\text{PzMe})]^{3+}$ cation has recently been explained using such arguments ^[81]. It is relevant at this point therefore to briefly review the MLCT process.

The conventional interpretation of a MLCT transition is the interaction between a π -symmetry ‘non-bonding’ metal orbital and an empty, high energy, ligand antibonding orbital. Elegant resonance Raman studies have shown conclusively that the lowest energy MLCT transition for the $[\text{M}(\text{CO})_4(\text{diimine})]$ analogues $[\text{M} = \text{Mo}(0)^{[96]}$ and $\text{W}(0)^{[97]}$] is the z-polarised $b_2 \longrightarrow b_2^*$ transition, with the transition moment lying antiparallel to the ground state dipole moment ^[98].

As the $[\text{Fe}(\text{CN})_4(\text{LL})]^{2-}$ complexes are both isoelectronic and isostructural with these $[\text{M}(\text{CO})_4(\text{diimine})]$ analogues it is quite reasonable to assume that the same transition is involved for both. The MO diagram for this transition is shown in Figure 3.6.

Thus, on excitation the dipole moment of the excited state is reduced relative to the ground state ^[99] as the ligand acquires significant radical character

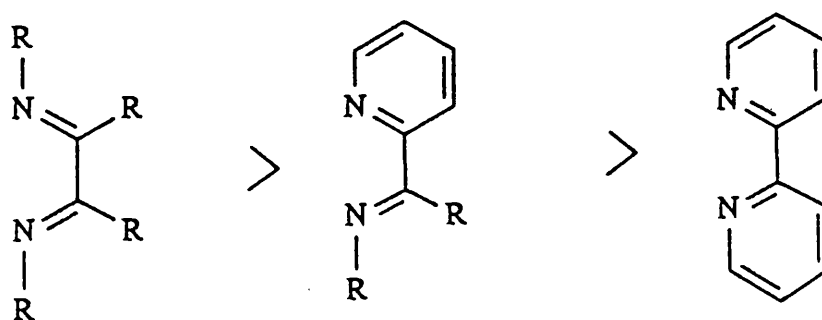


The ground state is strongly solvated in polar solvents, the Franck–Condon excited state will be correspondingly destabilised relative to that in non-polar solvents. In the latter, solvent interactions with the ground- and excited-states are weaker, and the transition lies at lower energy.

The solvent sensitivity will be greatest when the change in dipole moment between the ground- and excited-state is greatest, i.e. when the mixing between the d_π and L_{π^*} orbitals is small ^[100] (Figure 3.6a). The extent of mixing will depend predominantly on the π -acceptor ability of the diimine moiety so that as the π -acceptor ability increases, the orbital mixing increases, and the solvent

sensitivity decreases. As the energy of the L_{π^*} orbital lowers (as its π -acceptor ability increases) the situation arises where the metal and ligand manifolds are degenerate (Figure 3.6b). Now, the transition is purely metal–ligand bonding to antibonding and will effectively not be solvatochromic.

The relative π -acceptor ability of a series of bidentate diimine ligands has been calculated ^[101]. These are depicted in Figure 3.7. The solvent sensitivities in Table 3.3 are consistent with these values, and fall into the general trend of ligand π -acceptor ability



If the π -acceptor ability increases even further, to the position illustrated in Figure 3.6c, the orbital energy ranking is similar to that for a typical LMCT transition. This is quite reasonable for the $[\text{Fe}(\text{CN})_4(\text{bqdi})]^{2-}$ anion when one looks at Figure 3.7. A MLCT transition for such a species will reduce, or even possibly reverse, the molecular dipole moment, and hence give rise to the unexpected solvatochromic shift.

Several other anomalies arise over complexes containing the bqdi ligand. The C—N bond lengths in $[\text{Fe}(\text{bqdi})_3]^{2+}$ and in $[\text{Fe}(\text{CN})_4(\text{bqdi})]^{2-}$ are comparable to other ligands of pure α -diimine character such as gmi and bmi. The iron–nitrogen bond lengths are however considerably shorter than for any other

diimine ligand, confirming exceptionally strong metal–ligand bonding (see Section 3.3.4). The stabilisation of the iron(II) oxidation state is also much greater than that for other iron(II)–diimine complexes, and reflects the exceptional π -acceptor ability of this ligand. The standard redox potentials are given in Table 3.4.

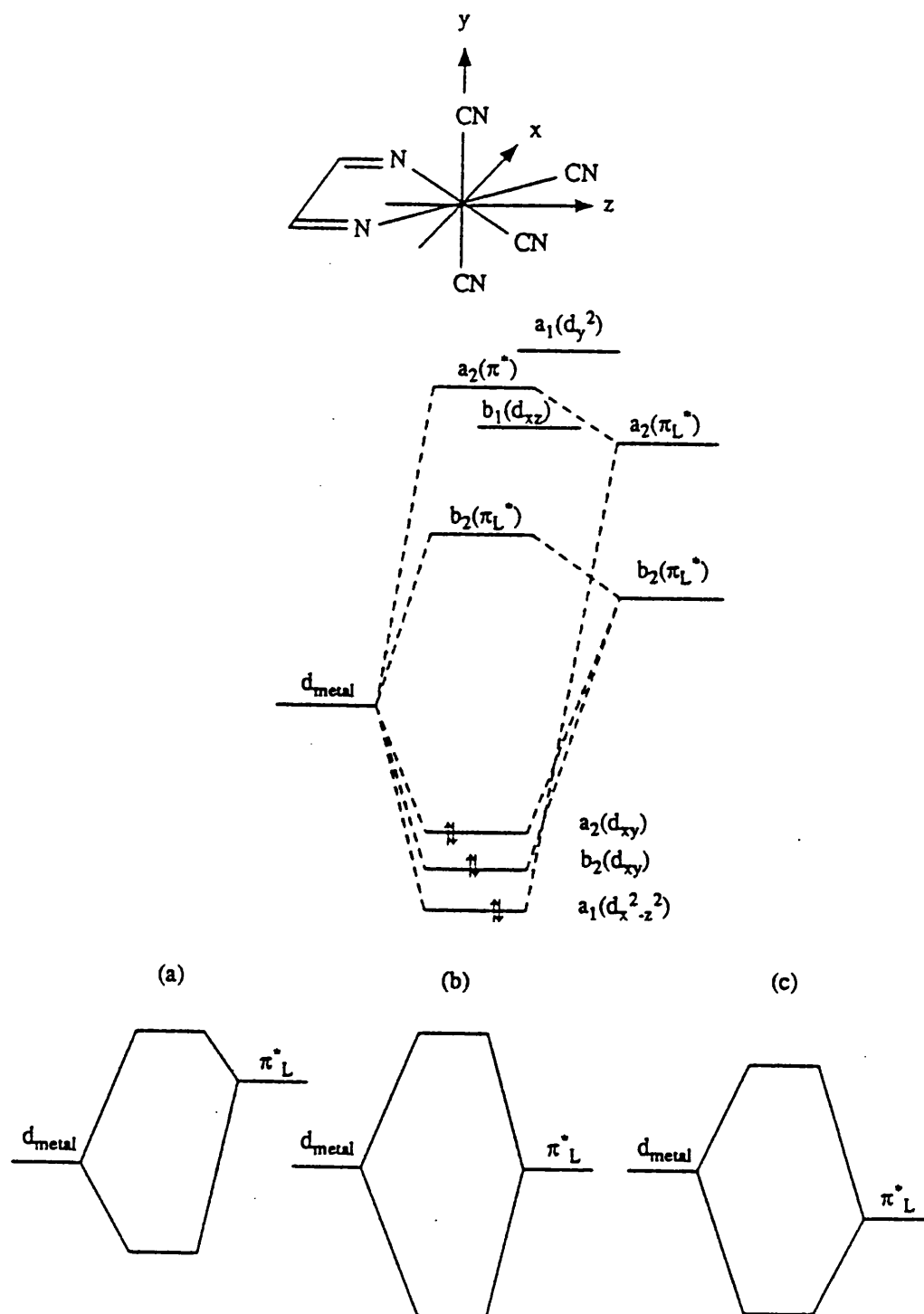


Figure 3.6 Molecular orbital diagram illustrating the relevant optical transitions in the $[\text{Fe}(\text{CN})_4(\text{LL})]^{2-}$ anion.

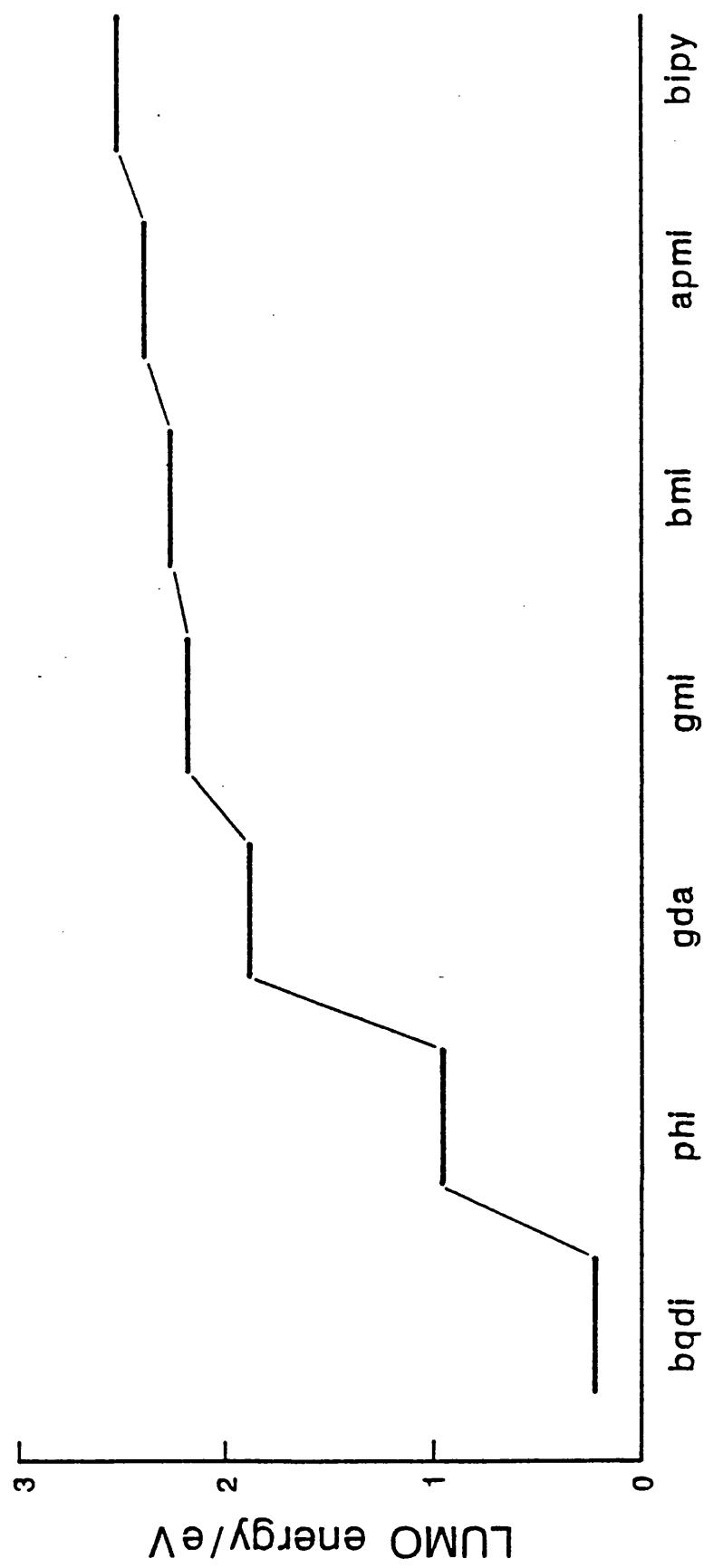


Figure 3.7 Relative π -acceptor ability of diimine ligands.

Complex ^a	E ^o ^b / V	Ref.
[Fe(bqdi) ₃] ²⁺	1.45	[102]
[Fe(CN) ₆] ⁴⁻	0.36	[103]
[Fe(CN) ₂ (bipy) ₂]	1.02	[103]
[Fe(CN) ₄ (bipy)] ²⁻	0.56	[104]
[Fe(bipy) ₃] ²⁺	1.29	[105]

^a Ligands defined in text.

^b Values quoted are vs. NHE.

Table 3.4 Standard redox potentials for a selection of iron(II) complexes.

3.3.3 Piezochromism.

In this Section the piezochromism of a selection of new ternary iron(II) complexes has been undertaken to extend the correlation between solvatochromic and piezochromic effects.

The correlation between piezo-, thermo-, and solvatochromic shifts for ternary $\text{Mo}(\text{CO})_4(\text{LL})$ complexes has been established [65]. Attempts to repeat this procedure for ternary iron–cyanide–diimine complexes are particularly promising because of the possibility of having both iron(II) and iron(III) oxidation states. This enables one to correlate both MLCT and LMCT transitions.

The pressure dependence of the charge transfer frequency of two ternary iron(II)–cyanide–diimine complexes is reported in Table 3.5. Table 3.6 compares these piezochromic coefficients with several complexes taken from the literature. Figure 3.8 shows the overall correlation of solvent sensitivity against pressure sensitivity. Also included in this Figure are data for the binuclear mixed valence bis(fulvalene)diiron complex [24,106,107]. The faint line shown in this Figure is the correlation line for the $[\text{Mo}(\text{CO})_4(\text{diimine})]$ series [65].

Complex ^a	ν_{MLCT} ^b at pressure P / bar				$\left(\frac{\partial \nu}{\partial P}\right)_T$ / cm ⁻¹ kbar ⁻¹ ($\sigma = 10$)
	50	500	1000	1500	
[Fe(CN) ₄ (bqdi)] ²⁻	17400	17410	17420	17420	+15
[Fe(CN) ₄ (ein)] ²⁻	19510	19570	19600	19650	+90

^a Ligand formulae defined in text.

^b Frequencies quoted are in cm⁻¹.

Table 3.5 ν_{MLCT} as a function of pressure for a series of ternary iron(II)-cyanide-diimine complexes (298.2 K).

Complex ^a	$\left(\frac{\partial \nu}{\partial P}\right)_T / \text{cm}^{-1} \text{ kbar}^{-1}$ (2 σ)	Ref.
[Fe(CN) ₄ (ein)] ²⁻	+90 (20)	a
[Fe(CN) ₄ (bqdi)] ²⁻	+15 (20)	a
[Fe(CN) ₂ (bipy) ₂]	+55 (20)	[64]
[Fe(CN) ₂ (bipy) ₂] ⁺	-170 (125)	[64]
[Fe(CN) ₄ (bipy)] ²⁻	+110 (25)	[64]
[Fe(CN) ₄ (bipy)] ⁻	-60 (50)	[64]

^a This work.

^b Ligands are defined in text.

Table 3.6 Pressure sensitivities for a series of ternary iron(II)-cyanide-diimine complexes (298.2 K).

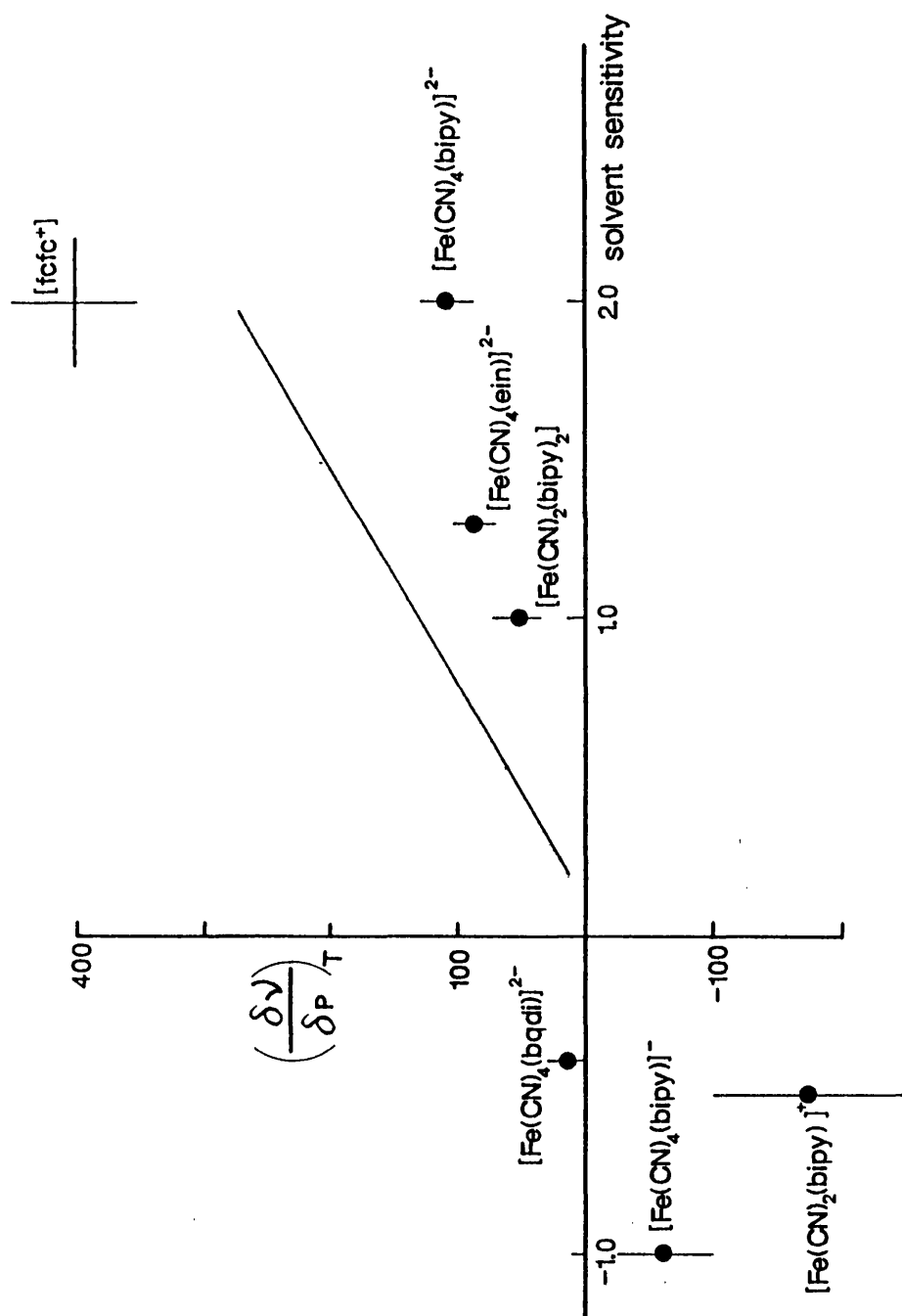


Figure 3.8 Correlation between piezo- and solvatochromic co-efficients for a series of ternary iron(II)-cyanide-diimine complexes.

3.3.4 Crystal Structures.

This Section reports the crystal structures of the $\text{H}[\text{Fe}(\text{CN})_4(\text{bipy})]\cdot 2\text{H}_2\text{O}$ and $\text{K}_2[\text{Fe}(\text{CN})_4(\text{en})]\cdot 3\text{H}_2\text{O}$ complexes, and compares them with related structures taken from the literature. The relevant bond angles and bond lengths are reported in Table 3.7 with data for analogues.

The structures of $\text{K}_2[\text{Fe}(\text{CN})_4(\text{en})]\cdot 3\text{H}_2\text{O}$ and $\text{H}[\text{Fe}(\text{CN})_4(\text{bipy})]\cdot 2\text{H}_2\text{O}$ are illustrated in Figures 3.9 and 3.11 respectively.

Coordination Polyhedron.

The iron–nitrogen and carbon–nitrogen bond lengths within the chelate ring for the $[\text{Fe}(\text{CN})_4(\text{en})]^{2-}$ anion are 2.07–2.08 Å and 1.45–1.47 Å respectively. These are of course substantially longer than for those ligands capable of metal–ligand delocalisation (cf. Table 3.7).

Several ternary tetracyano–iron(II)–diamine complexes; $[\text{Fe}(\text{CN})_4(\text{LL})]^{2-}$ (LL = cxa and cpa) have been synthesised ^[108]. Structural data for such simple Fe—N σ bonds have yet to be reported however. Possibly the best (and only) complexes with which to make constructive comparison are the low-spin iron(II) complexes $[\text{Fe}(\text{hxsbH})]^{2+}$ ^[109] and $[\text{Fe}(\text{tptcn})]^{2+}$ ^[110]. Here, the Fe—N and C—N bond lengths within the central N—CH₂—CH₂—N chelating unit are 2.00 and 1.49 Å (for hxsbH) and 2.00 and 1.51 Å (for tptcn) respectively. Thus, all C—N bonds are comparable to that in RNH₂ (taken to be 1.47 Å ^[111]). The iron–nitrogen bonds in $[\text{Fe}(\text{CN})_4(\text{en})]^{2-}$ are, in contrast, significantly longer than in either $[\text{Fe}(\text{hxsbH})]^{2+}$ or $[\text{Fe}(\text{tptcn})]^{2+}$.

The bond angles at the carbon and nitrogen atoms within the 5-membered ring are all close to that one would expect for sp^3 hybridised atoms (109.5°) except for the $\angle\text{C—C—N}$ angles, which are slightly expanded to 112°. This

reflects the relatively small bite of such a five membered ring at iron(II), and the large crystal field stabilisation energy for the latter being able to force slight angle strain in the relatively flexible (cf. bmi or gmi) chelate ring. This is reinforced by the angle subtended at the iron by the diamine ligand ($\angle \text{N—Fe—N} = 82^\circ$), greater than for the Schiff base diimine ligands in Table 3.7.

Significantly, the C—C bond in the chelate ring is substantially shorter than one would expect (bond lengths for hxsbH and tptcn are 1.51 and 1.52 Å respectively). In fact, at 1.45 Å, it falls within the range of those ligands with some degree of multiple bond character. In comparison ^[111], typical C—C bond lengths are 1.53 Å (in cyclohexane), 1.40 Å (in benzene), and 1.34 Å (in ethene).

The N₁—C₁—C₂—N₂ torsion angle in the diamine ring is 45.7° and is shown in Figure 3.10. The Newman projection along the C₁—C₂ axis highlights the torsion angle, Φ . Within the chelate ring there appears to be a considerable degree of van der Waals strain, with several H—H non-bonding distances being substantially less than the sum of their van der Waals radii (i.e. < 2.5 Å). The degree of torsional strain imposed by the above, and by coordination, is significantly less than for either [Fe(hxsbH)]²⁺ ($\Phi = 42.5^\circ$) or [Fe(tptcn)]²⁺ ($\Phi = 29^\circ$). Presumably the latter ligands impose greater geometric constraints because of their multidentate nature.

Unlike the [Fe(Bcxcage)] complex ^[112], no evidence for ring inversion was observed during structural refinement. Rapid inversion (in the iron(III) analogue) occurs in solution however, with $k_1 = 3 \times 10^8 \text{ s}^{-1}$ ^[113].

Complex ^a	Bond lengths / Å			∠N—Fe—N	Ref.
	Fe—N	N—C	C—C		
[Fe(bipy) ₃] ²⁺	1.96–1.99	1.34–1.35	1.42–1.48	82	[114]
[Fe(phen) ₃] ²⁺	1.96–1.98	1.31–1.39	1.38	83	[115]
[Fe(C ₃ N ₃ cxcage)] ²⁺	1.90–1.93	1.26–1.29	1.43–1.45	77–79	[116]
[Fe(gmi) ₃] ²⁺	1.95	1.27	1.42	80	[117]
[Fe(bmi) ₃] ²⁺	1.96	1.29	1.48	79.5	[117]
[Fe(bqdi) ₃] ²⁺	1.90–1.92	1.29–1.32	1.45–1.46	79.4	[118]
[Fe(bdh) ₃] ²⁺	1.96	1.29	1.47	79.4	[112]
[Fe(CN) ₂ (bdh) ₂]	1.94	1.32	1.45	78.6	[112]
[Fe(CN) ₄ (bqdi)] ^{2–}	1.91	1.32	1.44	80.4	[71]
[Fe(SCN) ₂ (phen)] ^{2–} ^b	2.00	1.35	1.43	81.8	[119]
[Fe(SCN) ₂ (phen)] ^{2–} ^c	2.20	1.37	1.42	76.1	[119]
[Fe(CN) ₄ (bipy)] [–]	1.98	1.34–1.35	1.47	80.8	d
[Fe(CN) ₄ (en)] ^{2–}	2.07–2.08	1.45–1.47	1.45	82	d

^a Ligands are shown in Scheme 3.1.

^b Low-spin.

^c High-spin.

^d This work.

Table 3.7 Bond lengths and bond angles for the ternary
iron(II)–cyanide–diimine complexes and analogues.

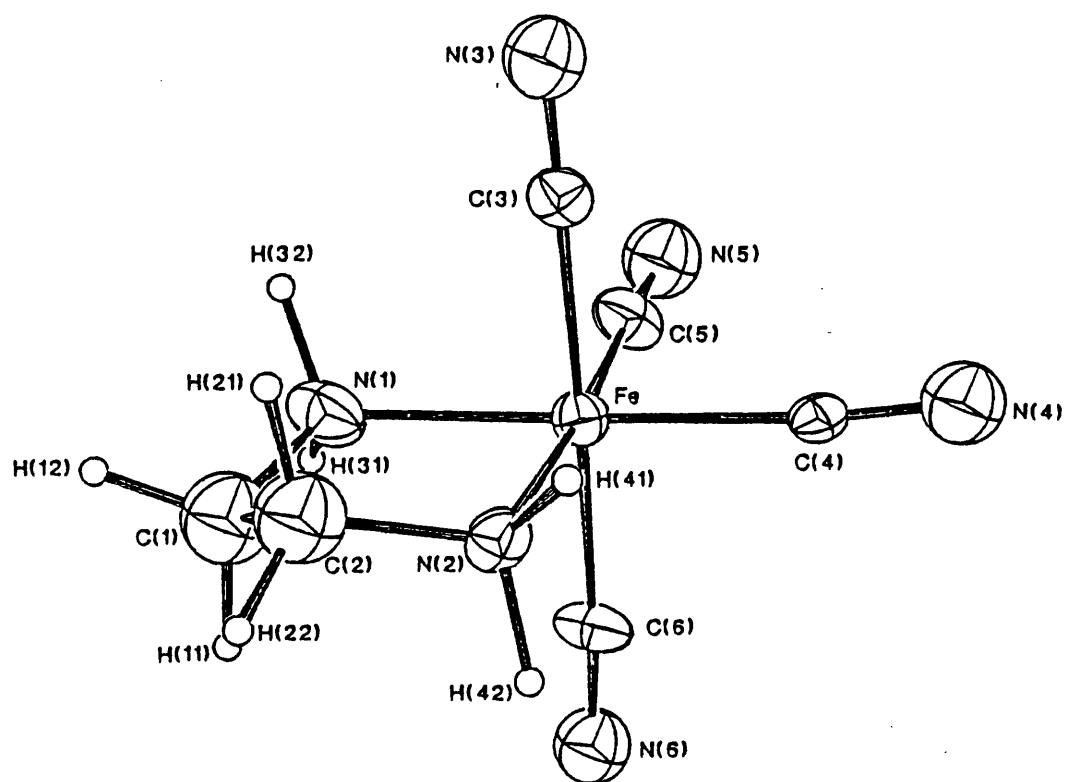


Figure 3.9 Crystal structure of $K_2[Fe(CN)_4(en)] \cdot 3H_2O$.

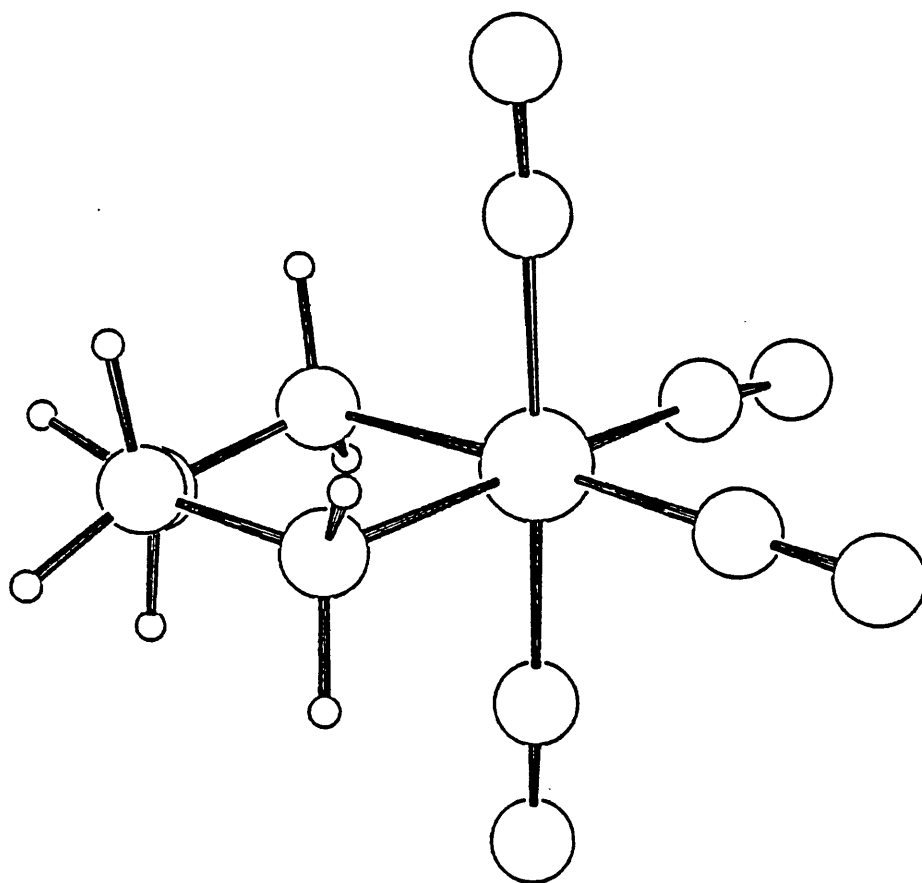
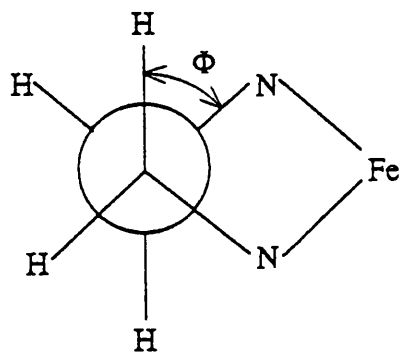


Figure 3.10 Illustration of the torsion angle in $[\text{Fe}(\text{CN})_4(\text{en})]^{2-}$.

Oxidation State.

The coordination polyhedron of the bipy ligand in the $[\text{Fe}(\text{CN})_4(\text{bipy})]^-$ anion is, within experimental error, unchanged from that in $[\text{Fe}(\text{bipy})_3]^{2+}$, with $\text{Fe}-\text{N} = 1.98 \text{ \AA}$.

The loss of an electron should weaken metal-ligand bonding, although this would be more significant for high spin complexes than for low spin. Thus for $[\text{Fe}(\text{phen})_3]^{2+/3+}$ $\delta(\text{Fe}-\text{N}) = 0.003 \text{ \AA}$, and 0.026 \AA for $[\text{Fe}(\text{CN})_6]^{3-/4-}$. This compares with 0.128 \AA for $[\text{Fe}(\text{OH}_2)_6]^{2+/3+}$ [120].

The $\text{Fe}-\text{C}$ and $\text{C}\equiv\text{N}$ bond lengths vary considerably for both complexes. Such variations are due in part to hydrogen-bonding between the nitrogen lone pairs on the coordinated cyanide moieties and hydrate molecules. This is discussed in the following Section.

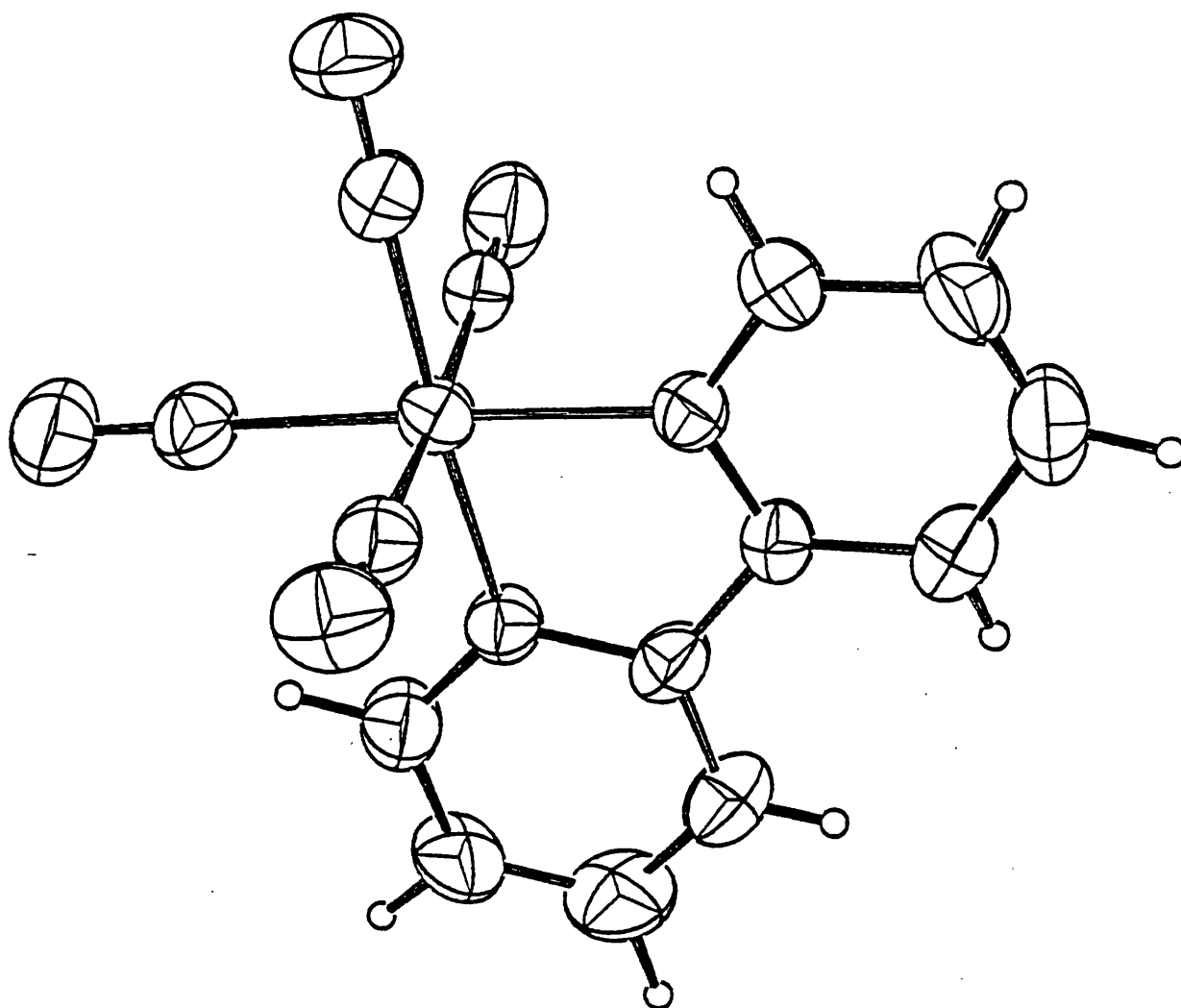


Figure 3.11 Crystal structure of $\text{H}[\text{Fe}(\text{CN})_4(\text{bipy})]\cdot 2\text{H}_2\text{O}$.

Solvate interactions.

The importance of the interaction between solvent molecules and the periphery of these ternary complexes, evident from the solvatochromic and solvation studies conducted in Section 3.3.1, is illustrated further when one looks at the role of the solvate molecules in the unit cell. Figures 3.12 and 3.13 show stereo pair diagrams of the unit cell for $\text{K}_2[\text{Fe}(\text{CN})_4(\text{en})] \cdot 3\text{H}_2\text{O}$ and $\text{H}[\text{Fe}(\text{CN})_4(\text{bipy})] \cdot 2\text{H}_2\text{O}$.

In the former, interactions occur primarily between hydrate and potassium counter-ions, with the water molecules orientated to maximise the electrostatic stabilisation. The hydrogen-bonding interactions between hydrate molecules and the cyanide nitrogens for $\text{K}_2[\text{Fe}(\text{CN})_4(\text{en})] \cdot 3\text{H}_2\text{O}$ and, more significantly, for $\text{H}[\text{Fe}(\text{CN})_4(\text{bipy})] \cdot 2\text{H}_2\text{O}$, are illustrated as faint lines in these Figures. For the latter, the proton and the two water molecules appear to be combined into a $[\text{H}_5\text{O}_2]^+$ cation (see Figure 3.16), with three hydrogen atoms from this cation involved in hydrogen-bonding to the anion. A quantitative evaluation of these interactions can be made from Figures 3.14 and 3.15.

As one would intuitively expect, hydrogen-bonding leads to an increase in $\text{C}\equiv\text{N}$, and a corresponding decrease in $\text{Fe}-\text{C}$ bond lengths. The data are slightly complicated by the different *trans* effects of the bidentate and the cyanide ligands.

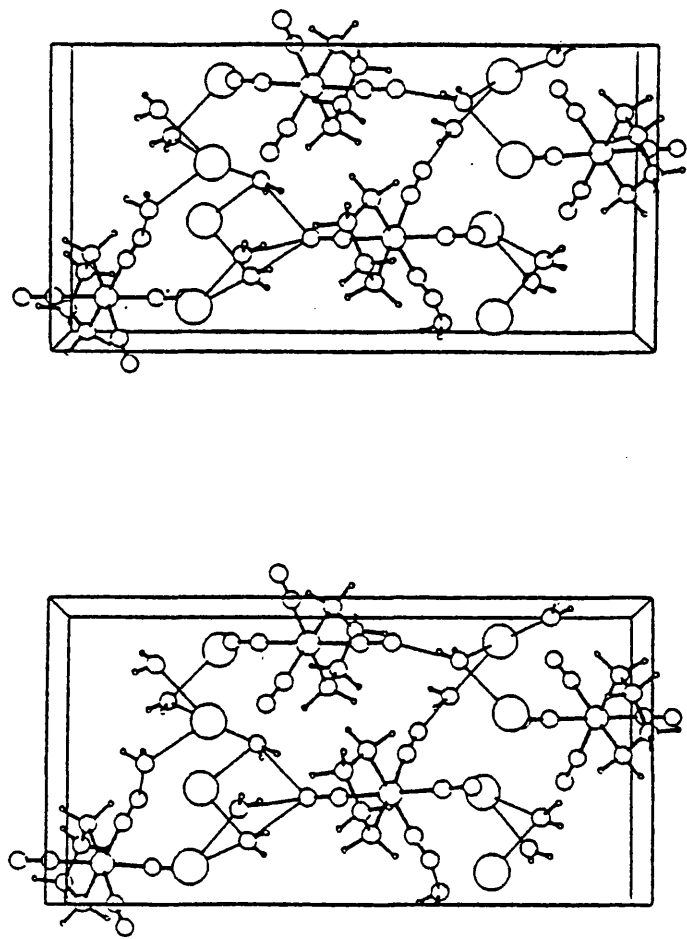


Figure 3.12 Stereo view of the unit cell of $K_2[Fe(CN)_4(en)] \cdot 3H_2O$.

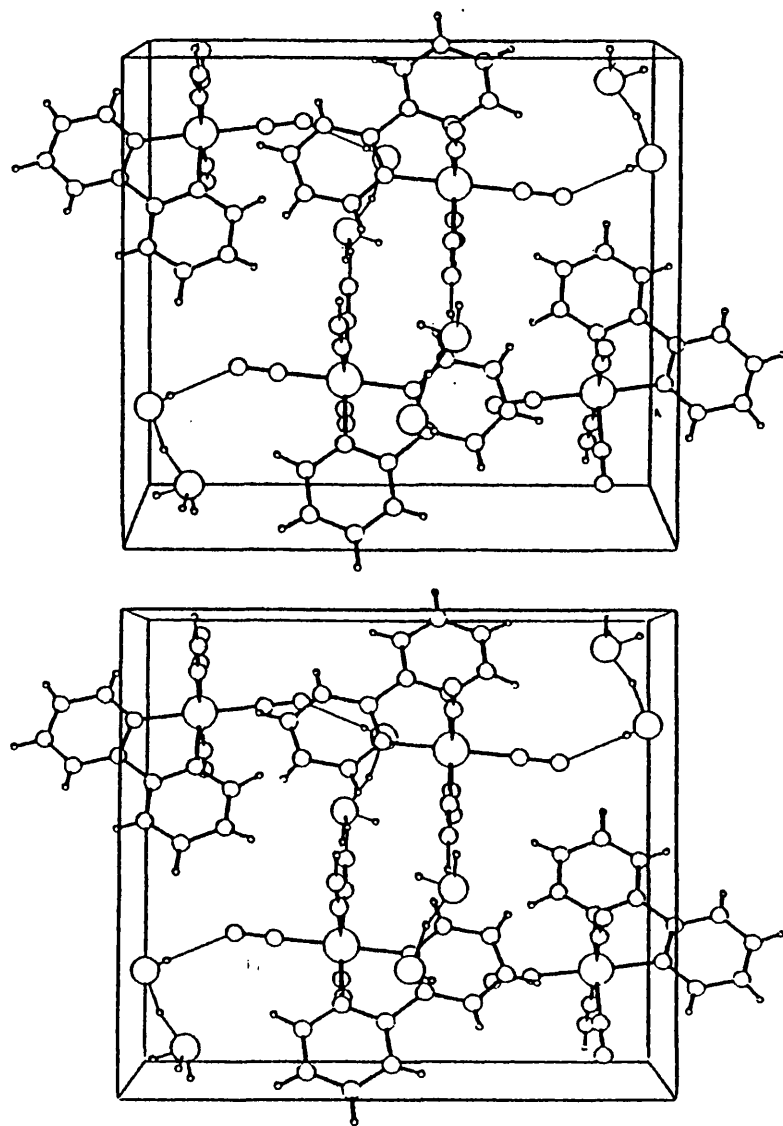


Figure 3.13 Stereo view of the unit cell of $\text{H}[\text{Fe}(\text{CN})_4(\text{bipy})]\cdot 2\text{H}_2\text{O}$.

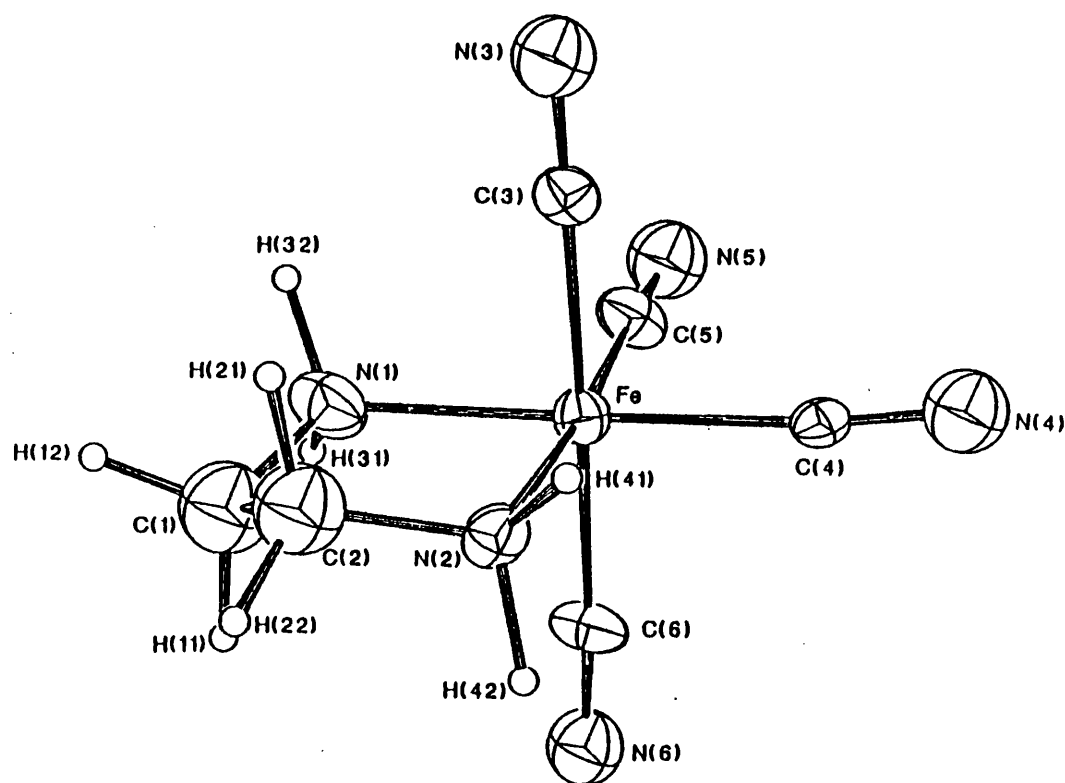
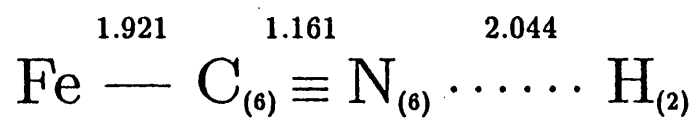
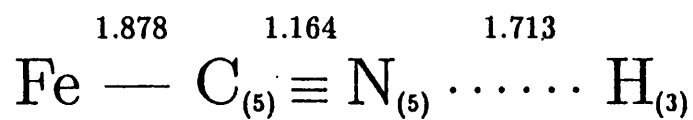
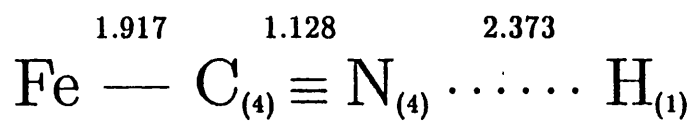
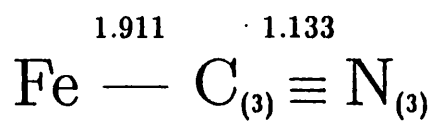


Figure 3.14 Hydrogen bonding interactions for $\text{K}_2[\text{Fe}(\text{CN})_4(\text{en})] \cdot 3\text{H}_2\text{O}$.

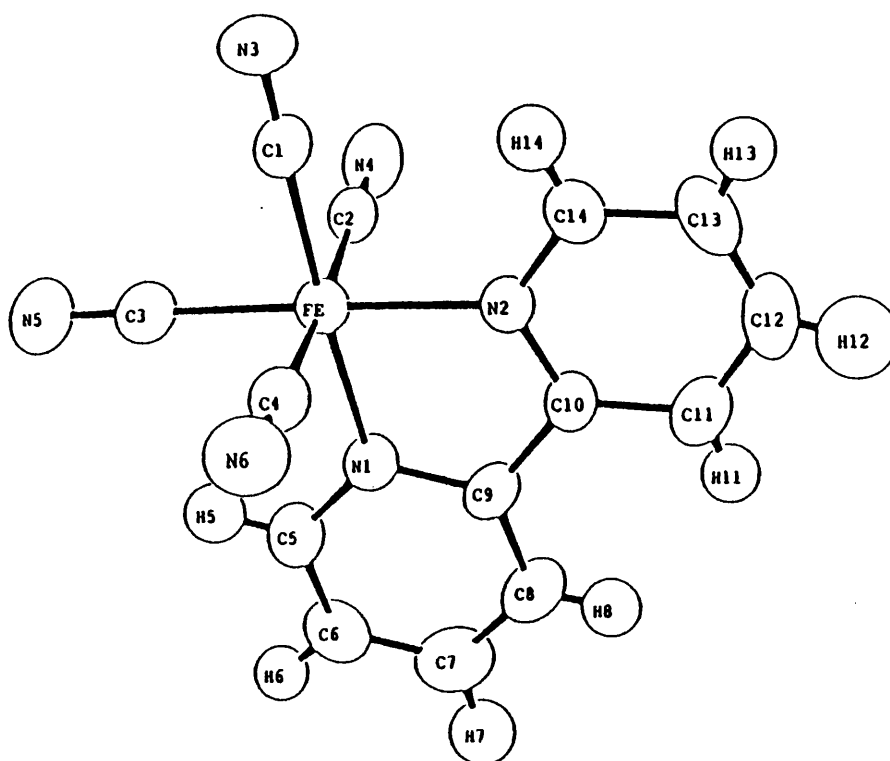
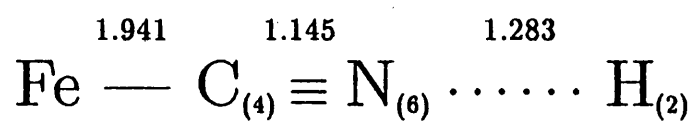
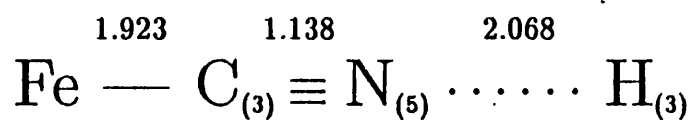
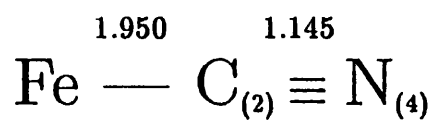
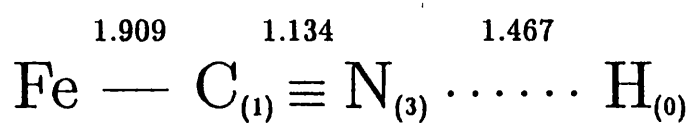


Figure 3.15 Hydrogen bonding interactions for $\text{H}[\text{Fe}(\text{CN})_4(\text{bipy})] \cdot 2\text{H}_2\text{O}$.

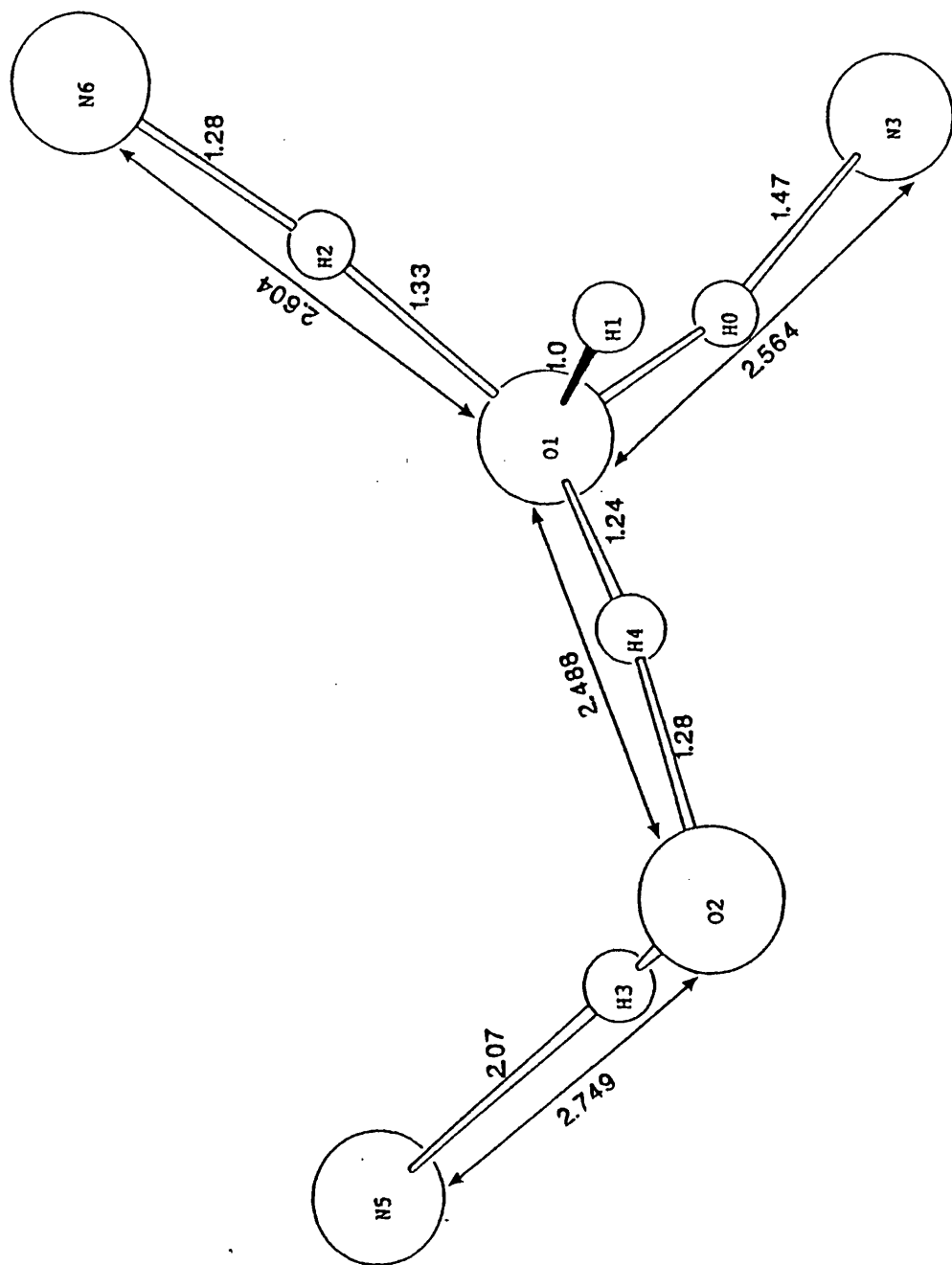


Figure 3.16 $[H(OH_2)_2]^+$ from the unit cell of $H[Fe(CN)_4(bipy)] \cdot 2H_2O$.

3.4 Concluding Remarks.

Clearly, such specific solvent effects are important – not only for the intramolecular electron transfer transitions described here, but for all aspects of solution chemistry. New techniques, or at least new developments in current techniques are needed so that specific solvent effects can be monitored in situ. EXAFS is one technique which shows considerable promise. Bond lengths in a series of iron and ruthenium complexes from crystallographic and from EXAFS sources have been compared ^[120]. Data were comparable for complexes such as $[\text{Fe}(\text{phen})_3]^{2+}$. For the $[\text{Fe}(\text{CN})_6]^{4-}$ and $[\text{Fe}(\text{OH}_2)_6]^{2+}$ complexes, where ligand–solvent hydrogen–bonding can occur, metal–ligand bond lengths obtained via EXAFS were consistently shorter than those in the solid state.

An additional approach to characterise ligand–solvent interactions in situ is preresonance Raman spectroscopy analysed using time dependent scattering. Changes in the charge transfer energy for the $[\text{Ru}(\text{bipy})(\text{NH}_3)_4]^{2+}$ cation were recently analysed quantitatively in terms of the modification of $\text{Ru}-\text{NH}_3$ bond strengths and consequent charge distribution brought about by hydrogen–bonding ^[121].

Significant advances in the analysis of solvent effects on redox processes, particularly preferential solvation in mixed solvents, are being made through ternary ruthenium complexes such as $[\text{Ru}(\text{NH}_3)_4(\text{bipy})]^{2+/3+}$ ^[122]. Unsymmetrical preferential solvation in binuclear analogues, such as $[(\text{bipy})_2\text{ClRu}-\text{pz}-\text{Ru}(\text{NH}_3)_4(\text{py})]^{3+}$, occurs between the diruthenium(II) and the mixed valence complex ^[123]. In addition, differences in solvent–solute interactions are able to modulate the extent of orbital mixing and electronic coupling ^[124].

In the following Chapter the ternary iron(II)–cyanide–diimine complexes

mentioned in this Chapter are used as reductants to examine solvent and pressure effects on intermolecular electron transfer rates.

Chapter 4

*Volumes of Activation, Partial Molar
Volumes, and Solvent Effects Related
to the Peroxodisulphate Oxidation of
Ternary Iron(II)-diimine complexes*

4.1 Introduction.

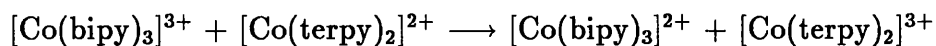
In comparison to other inorganic reactions there is a relatively small amount of data involving solvent and pressure effects on redox reactions. This applies particularly to simple outer-sphere electron transfer reactions, for which very few volumes of activation have been reported ^[125]. Some of these are given in Table below.

Reaction	Solvent	ΔV^\ddagger / cm ³ mol ⁻¹	Ref.
$[\text{Co}(\text{terpy})_2]^{2+} + [\text{Co}(\text{bipy})_3]^{3+}$	MeCN	-5	[126]
	water	-9	
	formamide	-14	
$[\text{Fe}(\text{CN})_4(\text{bipy})]^{2-} + \text{S}_2\text{O}_8^{2-}$	water	0	[127]
$[\text{Co}(\text{NH}_3)_5(\text{N}_3)]^{2+} + \text{Fe}_{aq}^{2+}$	water	+12	[128]
$[\text{Co}(\text{NH}_3)_5(\text{OH}_2)]^{3+} + [\text{Fe}(\text{CN})_6]^{4-}$	water	+27	[129]

The electron exchange between $[\text{Fe}(\text{OH})]_{aq}^{2+}$ and Fe^{2+} , and the peroxodisulphate oxidation of $[\text{Fe}(\text{CN})_4(\text{bipy})]^{2-}$ have activation volumes of zero. These have been interpreted as the balance between opposing intrinsic and solvation contributions of the reactants. Counter-ion solvation has also been shown to be important for the $[\text{MnO}_4]^{2-/-}$ exchange reaction, where activation volumes for the cation-dependent pathway are +3.3 and -1.1 cm³ mol⁻¹ for the Na⁺ and K⁺ salts respectively ^[130].

Amongst the few simple OSET reactions reported, only a small number have

shown a significant solvation effect. Thus for the reaction

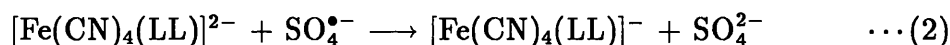
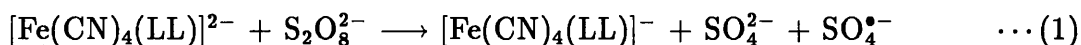


ΔV_{obs}^\ddagger varies from -5 to $-14 \text{ cm}^3 \text{ mol}^{-1}$ between acetonitrile and formamide. Such solvent variation of ΔV_{obs}^\ddagger implies significantly different solvation patterns between the initial- and transition-state in each of the respective media.

In this Chapter the outer-sphere electron transfer reaction between the peroxodisulphate anion ($\text{S}_2\text{O}_8^{2-}$) and a series of ternary iron(II)-cyanide-diimine complexes is examined. Kinetic and thermodynamic data are measured as functions of pressure and solvent composition. Data are discussed in terms of the differences in the solvation of the participating species due to electrostatic and ligand hydrophilic/hydrophobic nature.

4.2 Experimental.

The complexes $\text{Fe}(\text{CN})_2(\text{bipy})_2$ and $\text{K}_2[\text{Fe}(\text{CN})_4(\text{LL})]$ ($\text{LL} = \text{phen}, \text{ein}, \text{Me}_2\text{bsb}$) were all prepared as described in Chapter 2. All reagents were obtained from Aldrich except $\text{K}_2\text{S}_2\text{O}_8$ which was AnalaR grade. The apparatus and technique used to determine the kinetic parameters is described in Chapter 2. The oxidation of the iron(II) complexes is proposed to occur via the mechanism shown



where step (1) is rate determining.

The peroxodisulphate concentration was in vast excess compared with that of the iron(II) complex. Good first-order kinetics were observed for the first half-life after which time the quality of the fit began to deteriorate slowly due to the presence of radicals. The extent of radical interference is much less than that observed for the $\text{S}_2\text{O}_8^{2-}$ oxidation of $[\text{Fe}(\text{phen})_3]^{2+}$ [131].

The reaction was monitored from the decrease in absorbance of the iron(II)-diimine chromophore with

$$-\frac{d[\text{complex}]}{dt} = k_{obs}[\text{Complex}]$$

The $\text{S}_2\text{O}_8^{2-}$ oxidation of iron(II)-diimine complexes, particularly those involving electron withdrawing ligands such as $[\text{Fe}(5\text{-NO}_2\text{phen})_3]^{2+}$ [132], showed that significant unimolecular decomposition of the iron complex occurred on the reaction timescale. The observed rate constant was therefore fitted to an equation of the general type

$$k_{(obs)} = (k_1 + k_2[\text{S}_2\text{O}_8^{2-}])$$

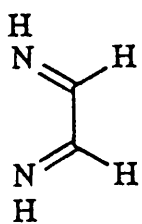
where the k_1 term corresponds to unimolecular decomposition of the iron(II) complex and k_2 to bimolecular oxidation.

The ternary complexes used here are ideal in this respect since k_1 values are extremely small ^[133]. The observed rate constant, k_{obs} , is therefore purely a function of the oxidation of the ternary iron(II) complex.

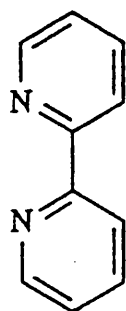
A small amount (ca. 10^{-5} mol dm⁻³) of EDTA was present to sequester any trace transition metal impurities present in the $S_2O_8^{2-}$ - avoiding unwanted catalysis.

All kinetic data were obtained using the SP 8-100 spectrophotometer described in Section 2.3.

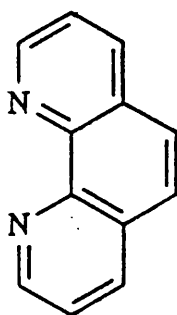
The measured apparent partial molar volumes are calculated for the hydrated solid samples. Conversion to the value for the anhydrous anion was made by subtracting $\bar{V} (H_2O)$ for each water of crystallisation (determined by thermogravimetrically or from the relevant crystal structure). Partial molar volumes were kindly measured by Dr Colin D. Hubbard and Dr Pilar Guardado.



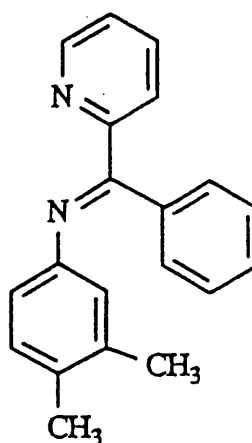
ein



bipy



phen



Me₂bsb

4.3 Results and Discussion.

4.3.1 Volumes of Activation.

The \log_{10} of the ratios of observed first-order rate constants at high pressure to their equivalents at atmospheric pressure are given in Table 4.1. Plots of these logarithm ratios against pressure were essentially linear and are shown in Figure 4.1. The dotted lines in this Figure correspond to a 60% DMSO–water mixture. The volumes of activation derived from such plots are given in Table 4.2.

Firstly, it is clear that the previous interpretation of balancing intrinsic and solvation terms for the peroxodisulphate oxidation of $[\text{Fe}(\text{CN})_4(\text{bipy})]^{2-}$ is correct. If one now compares the series of $[\text{Fe}(\text{CN})_4(\text{LL})]^{2-}$ anions the importance of complex hydrophobicity can clearly be seen. For the largest, and most hydrophobic, complex, $[\text{Fe}(\text{CN})_4(\text{Me}_2\text{bsb})]^{2-}$, $\Delta V_{obs}^\ddagger = -10.2 \text{ cm}^3 \text{ mol}^{-1}$. This is approximately that expected for a bimolecular reaction in the absence of a solvation contribution. As the hydrophobicity of the coordinated diimine moiety decreases (and the solvation contribution to ΔV_{obs}^\ddagger increases) the values increase progressively until, for $[\text{Fe}(\text{CN})_4(\text{ein})]^{2-}$ $\Delta V_{obs}^\ddagger = +5 \text{ cm}^3 \text{ mol}^{-1}$, where the release of electrostricted solvent dominates the intrinsic volume decrease.

In view of the fact that the partial molar volume of ‘free’ water is $+18 \text{ cm}^3 \text{ mol}^{-1}$ and that of electrostricted water is $+15 \text{ cm}^3 \text{ mol}^{-1}$ [134], it can be estimated that approximately 5 water molecules are released from the solvation sheath of the anion on transition state formation. This compares with approximately 3 for $[\text{Fe}(\text{CN})_4(\text{bipy})]^{2-}$ and one for the most hydrophobic (and least hydrated) $[\text{Fe}(\text{CN})_4(\text{Me}_2\text{bsb})]^{2-}$ anion.

Complex ^a	[K ₂ S ₂ O ₈] mol dm ⁻³	k ₂ (1 bar) mol ⁻¹ dm ³ s ⁻¹	log ₁₀ ($\frac{k_2}{k_a}$) at P / kbar			
			0.34	0.69	0.87	1.04
water						
K ₂ [Fe(CN) ₄ (ein)]	0.01	0.042	-0.023	-0.062	-0.081	
K ₂ [Fe(CN) ₄ (phen)]	0.0050	0.050	0.023		0.040	0.049
[Fe(CN) ₂ (bipy) ₂]	0.0020	0.120	0.047	0.089		0.148
K ₂ [Fe(CN) ₄ (Me ₂ bsb)]	0.008	0.026		0.101	0.135	0.185
60% DMSO						
K ₂ [Fe(CN) ₄ (phen)]	0.010	0.024		0.038		0.068
[Fe(CN) ₂ (bipy) ₂]	0.030	0.025		0.051	0.076	0.098

^a Ligand structures defined in text.

Table 4.1 Log₁₀($\frac{k_2}{k_a}$) as a function of pressure for the S₂O₈²⁻ oxidation of ternary iron(II) complexes (298.2 K).

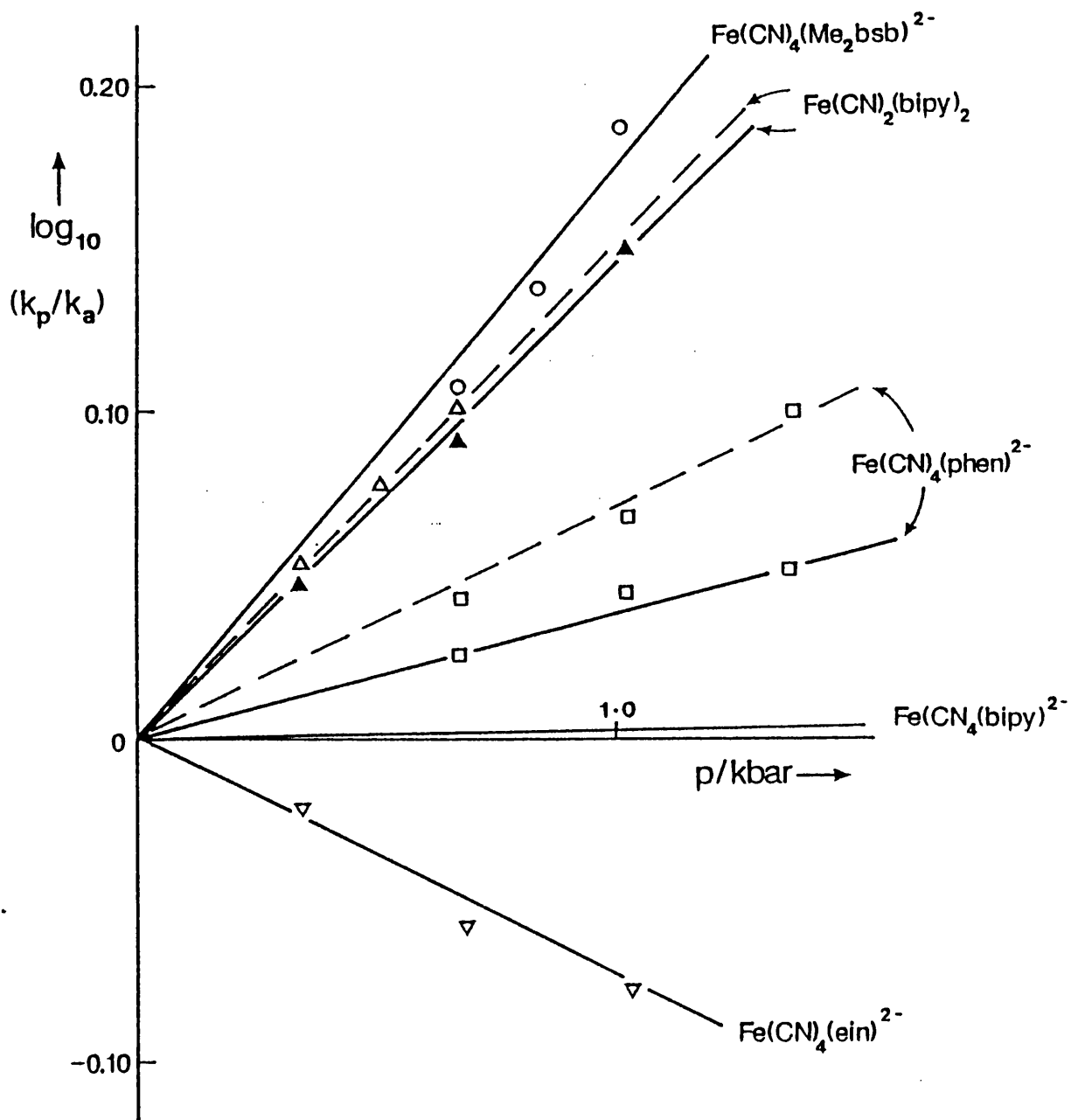


Figure 4.1 Plot of $\log_{10}(\frac{k_p}{k_a})$ vs. pressure.

Complex ^a	ΔV^\ddagger / cm ³ mol ⁻¹
K ₂ [Fe(CN) ₄ (ein)]	+4.6
K ₂ [Fe(CN) ₄ (bipy)]	0.0 ^b
K ₂ [Fe(CN) ₄ (phen)]	-2.1
[Fe(CN) ₂ (bipy) ₂]	-7.7
K ₂ [Fe(CN) ₄ (Me ₂ bsb)]	-10.2
K ₂ [Fe(CN) ₄ (phen)]	-3.6 ^c
[Fe(CN) ₂ (bipy) ₂]	-8.3 ^c

^a Ligand formulae defined in text.

^b Taken from ref. [127]

^c 60% DMSO–water solvent mixture

Table 4.2 Calculated activation volumes for the S₂O₈²⁻ oxidation of ternary iron(II)–cyanide–diimine complexes (298.2 K).

4.3.2 Partial Molar Volumes.

The partial molar volumes of several ternary iron(II)–cyanide–diimine complexes are reported in Table 4.3. The dependence of \bar{V} for the ternary complexes on ligand nature is shown in Figure 4.2.

The use of relative molecular mass as the x -ordinate may seem a rather crude approach, ignoring aspects of ligand geometry such as planar vs. puckered ring systems (ein vs. en) and group fluxionality which are of undoubted importance in determining the solvation of such structures. A previous attempt to correlate partial molar volumes with intrinsic complex volumes highlighted the uncertainty involved in the calculation of intrinsic volumes for such complex structures [135], and consequently no attempt has been made here to do so.

The effect of solvation on \bar{V} is illustrated by the $[\text{Fe}(\text{CN})_4(\text{bipy})]^{2-/-}$ couple. The iron(III) complex, with its -1 charge has a partial molar volume of $205 \text{ cm}^3 \text{ mol}^{-1}$. This compares to $181 \text{ cm}^3 \text{ mol}^{-1}$ for the dinegative iron(II) analogue. As the intrinsic size of the $[\text{Fe}(\text{CN})_4(\text{bipy})]^-$ anion is expected to be negligibly different from the iron(II) analogue (cf. Chapter 3) this discrepancy must be due to decreased solvent electrostriction and hydrogen-bonding. An increase of similar magnitude occurs between $[\text{Ni}(\text{edta})]^{2-}$ ($\bar{V} = 165 \text{ cm}^3 \text{ mol}^{-1}$) and $[\text{Fe}(\text{edta})]^-$ ($\bar{V} = 171 \text{ cm}^3 \text{ mol}^{-1}$) [136].

The relationship between partial molar volumes for the $[\text{Fe}(\text{CN})_4(\text{diimine})]^{2-}$ anions and a selection of other inorganic complexes is shown in Figure 4.3. The diagonal line is that taken from Figure 4.2.

The general correlation, although qualitative in its approach, is quite good, with, as one might intuitively expect, the $4-$ complexes, and the large $6+$ hexol complex all lying below the Figure 4.2. line. Data for hydrophobic organic

cations and anions; AsPh_4^+ , decylNMe_3^+ , and BPh_4^- ^[48], and the hydrophobic $[\text{Fe}(\text{diimine})_3]^{2+}$ cations ^[135] lie well above (and are parallel to) this line. The point for the particularly hydrophobic cation $[\text{Bu}_3\text{N}(\text{CH}_2)_8\text{NBu}_3]^{2+}$ ^[48] lies even higher. Interestingly, the $[\text{Fe}(\text{gmi})_3]^{2+}$ cation, whose transfer chemical potentials ^[68] indicate it to be at the hydrophobic/hydrophilic boundary, lies on the correlation line for the ternary anions – which, as mentioned in Section 3.3.1, have a similar mixed hydrophobic/hydrophilic surface. Complexes of greater hydrophilic character (of 4–, 3–, and 3+ charge) and even $[\text{PtCl}_4]^{2-}$, whose values ^[51] lie below the correlation line, confirm the pattern of increasing charge or hydrophilicity leading to less positive (\bar{V}) values.

Compound ^a	RMM (Anion)	\bar{V} / cm ³ mol ⁻¹	
		Salt	Anion ^b
K ₂ [Fe(CN) ₄ (ein)].4H ₂ O	216	105	87
K ₂ [Fe(CN) ₄ (en)].4H ₂ O	220	119	101
K ₂ [Fe(CN) ₄ (bqdi)].3H ₂ O	266	116	98
K ₂ [Fe(CN) ₄ (bipy)].3H ₂ O	316	199	181
K ₂ [Fe(CN) ₄ (phen)].4H ₂ O	340	198	180
K ₂ [Fe(CN) ₄ (Me ₂ bsb)].2H ₂ O	446	257	239
[H(OH ₂) ₂][Fe(CN) ₄ (bipy)]	316	240	205

^a Ligand abbreviations and formulae are given in the text.

^b Assuming $\bar{V}(\text{H}^+) = 0$ (cf. text).

Table 4.3 Partial molar volumes for a series of ternary iron(II)–cyanide–diimine complexes (298.2 K).

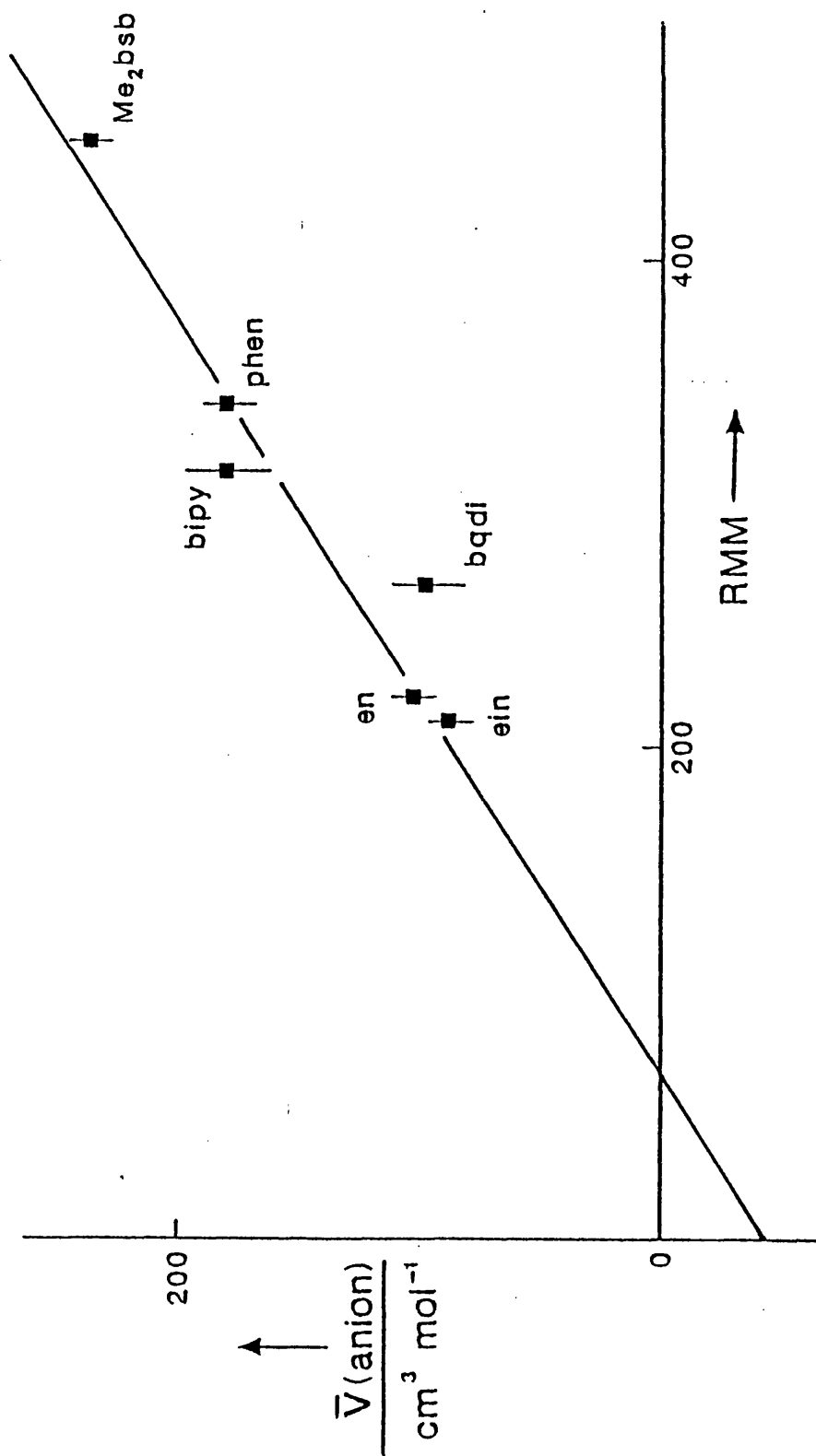


Figure 4.2 Plot of partial molar volume of the ternary
iron(II)-cyanide-diimine complexes vs. molecular weight.

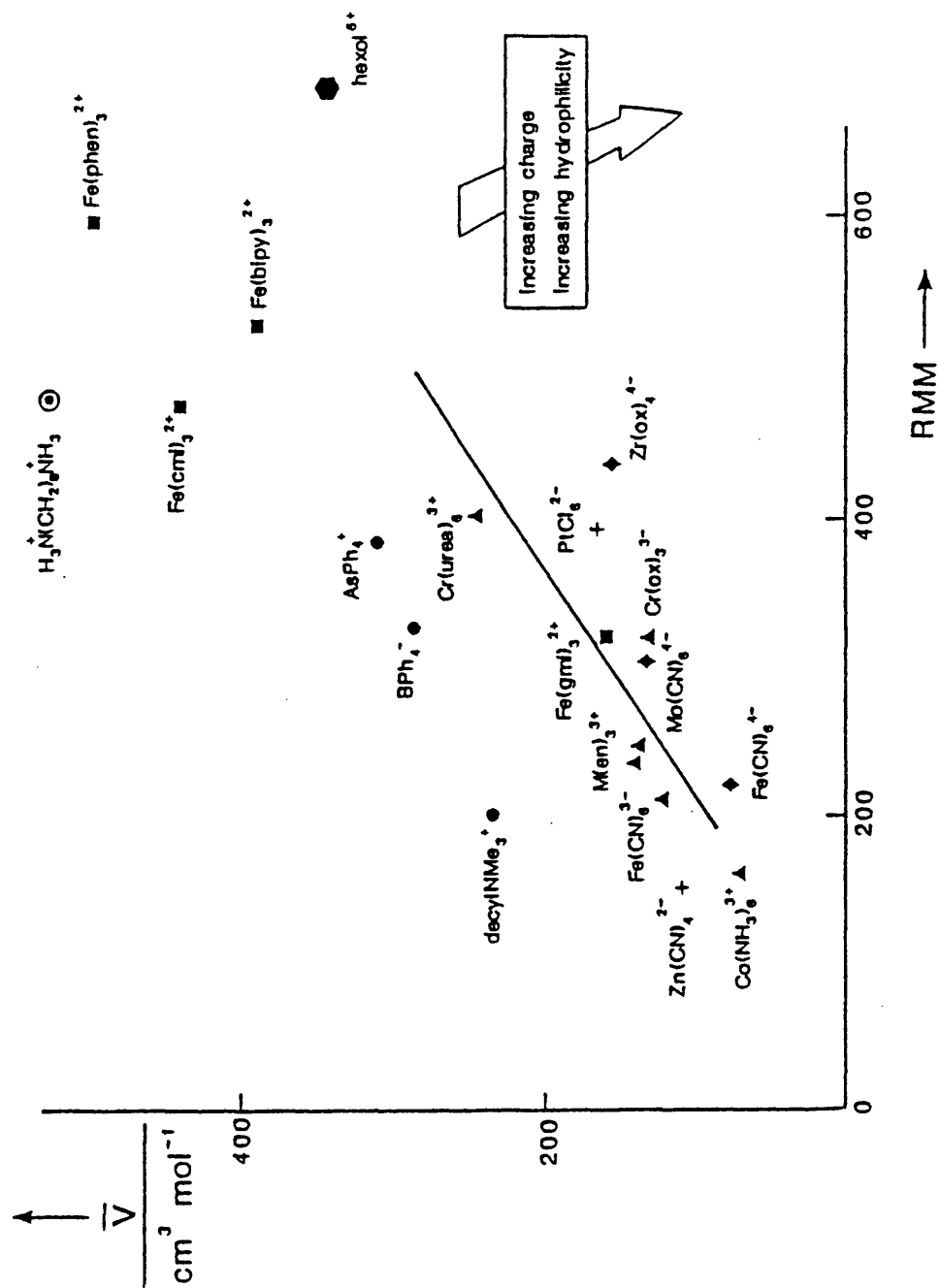


Figure 4.3 Plot of partial molar volumes for a selection of inorganic ions.

4.3.3 Volume Profile

The combination of the partial molar volumes of the reactants and products, and the activation volume allows one to construct a volume profile for a reaction (Section 2.10). The data needed for such a profile are collected in Table 4.4.

The partial molar volume of the $\text{SO}_4^{\bullet-}$ radical anion is unavailable. Here, it is assumed that $\bar{V}(\text{SO}_4^{\bullet-}) \cong \bar{V}(\text{ClO}_4^-)$. Such an assumption is expected to have a small effect ($\pm 2 \text{ cm}^3 \text{ mol}^{-1}$) on the analysis. The volume profile is illustrated in Figure 4.4.

Structure	$\bar{V} / \text{cm}^3 \text{ mol}^{-1}$	Ref.
$\text{S}_2\text{O}_8^{2-}$	80	[137]
$[\text{Fe}(\text{CN})_4(\text{bipy})]^{2-}$	181	a
IS	261	
ΔV_{obs}^\ddagger	0	b
TS	261	
$\text{SO}_4^{\bullet-}$ ^c	36	[48]
SO_4^{2-}	14	[48]
$[\text{Fe}(\text{CN})_4(\text{bipy})]^-$	205	a
Products	255	

^a This work.

^b From ref. [127].

^c $\bar{V}(\text{SO}_4^{\bullet-}) \cong \bar{V}(\text{ClO}_4^-)$ (cf. text).

Table 4.4 Volume profile data for the $\text{S}_2\text{O}_8^{2-}$ oxidation of $[\text{Fe}(\text{CN})_4(\text{bipy})]^{2-}$.

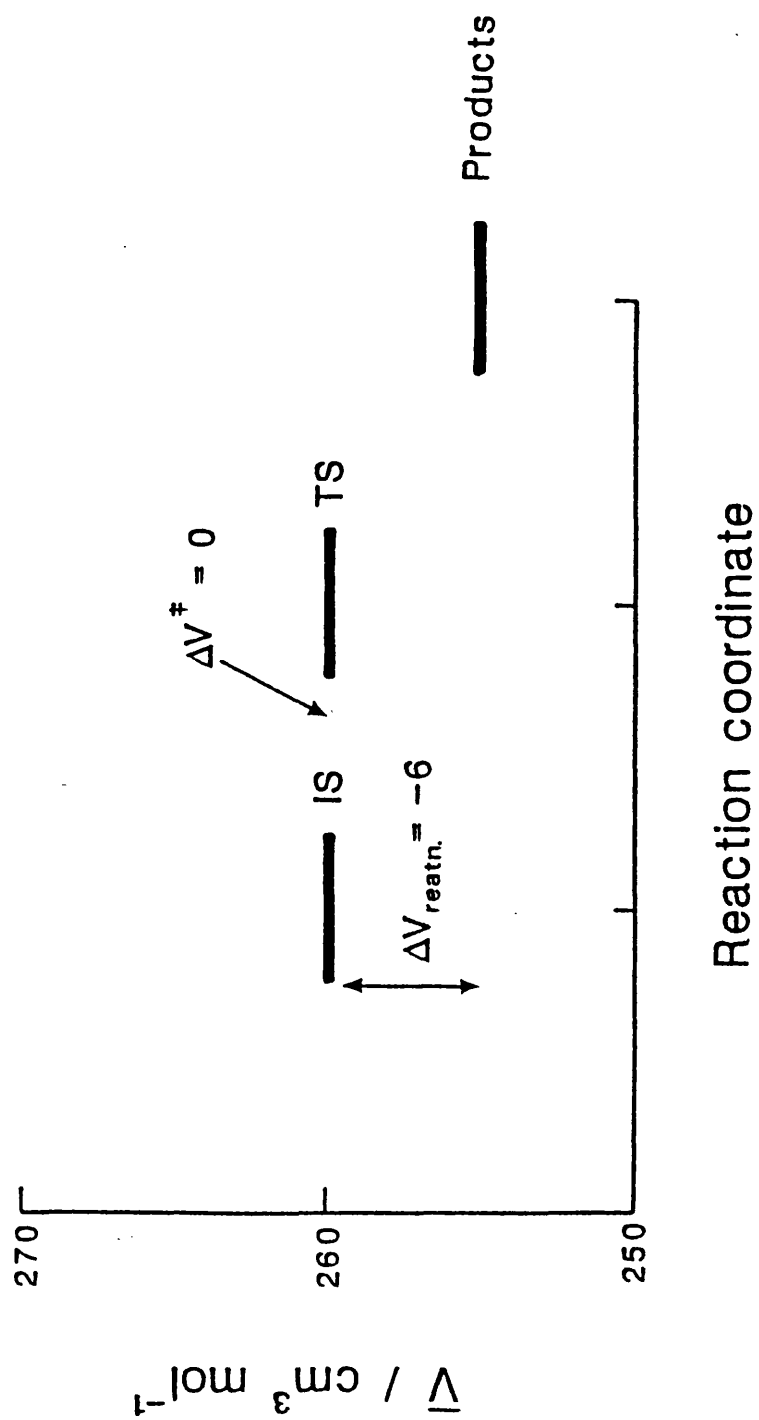


Figure 4.4 Volume profile for the $\text{S}_2\text{O}_8^{2-}$ oxidation of $[\text{Fe}(\text{CN})_4(\text{bipy})]^{2-}$.

There is a very small volume change of $-6 \text{ cm}^3 \text{ mol}^{-1}$ during the reaction which arises entirely from a decrease in volume between the transition state and the products. This change masks a decrease in solvation of the iron complex balancing an increase in solvation of the $\text{SO}_4^{\bullet-}$ and SO_4^{2-} fragments (relative to $\text{S}_2\text{O}_8^{2-}$). This is barely significant when one remembers the estimated value for the $\text{SO}_4^{\bullet-}$ component.

Transition state desolvation would be greater for reactants with a $2+/2-$ charge combination, where the outer-sphere associate would be formally uncharged. The design of potential iron(II) complexes is complicated by kinetic stability constraints. Cage, semi-cage, and garland-type hexadentate ligands, such as those shown in Scheme 3.1 form complexes of the required stability, although ligand oxidation, particularly for the latter type, can occur in preference to a metal centred process ^[117,138].

4.3.4 Initial State—Transition State Analysis.

The transfer chemical potentials from Chapter 3 are combined with the second-order rate constants for peroxodisulphate oxidation (Table 4.5) to give the initial state transition state analyses in Tables 4.6 – 4.8. These initial state transition state analyses are then shown in Figures 4.5 – 4.7.

$10^4 k_{obs} / s^{-1}^a$				
Complex ^b	Vol % DMSO			
	0	20	40	60
$Fe(CN)_2(bipy)_2$	65	22	4.6	0.62
$[Fe(CN)_4(bipy)]^{2-}$	26	21	12.7	9.2
$[Fe(CN)_4(Me_2bsb)]^{2-}$	21	120	230	25

^a $[K_2S_2O_8] = 0.02 \text{ mol dm}^{-3}$ ($\equiv I$) ; $[complex] = 1 \times 10^{-4} \text{ mol dm}^{-3}$.

^b Ligand formulae are defined in text.

Table 4.5 Observed first-order rate constants for $S_2O_8^{2-}$ oxidation of iron(II)–cyanide–diimine complexes in DMSO–water mixtures (298.2 K).

Rather strikingly the relatively small solvent effect on rate constants masks very large changes in IS and TS stability. In fact the destabilisation of the initial state in moving from water to 60% DMSO for the $\text{S}_2\text{O}_8^{2-}$ oxidation of $[\text{Fe}(\text{CN})_4(\text{bipy})]^{2-}$ is of similar magnitude to the activation barrier.

Although initial state destabilisation is large, reactivity patterns are determined by transition state effects. For $[\text{Fe}(\text{CN})_2(\text{bipy})_2]$ and the $[\text{Fe}(\text{CN})_4(\text{bipy})]^{2-}$ anion, the rate retardation observed is due to destabilisation of the transition state relative to the ground state. This dominance of reactivity by transition state destabilisation is relatively common for outer-sphere electron transfer reactions where the reactants have the same sign as in the reactions considered here. It is usually rationalised in terms of the destabilisation of the $[\text{Fe}(\text{CN})_4(\text{LL}), \text{S}_2\text{O}_8]^{4-}$ transition state relative to the component dianions. This is in contrast to the peroxodisulphate oxidation of $[\text{Fe}(\text{phen})_3]^{2+}$ [131] or of $[\text{Fe}(\text{C}_3\text{N}_3\text{cage})]^{2+}$ [139], where such transition state effects are less important due to the formally uncharged outer-sphere associate.

Vol % DMSO	0	20	40	60
$k_2 / \text{mol}^{-1} \text{dm}^3 \text{s}^{-1}$	0.33	0.11	0.023	0.0031
$\delta_m \Delta G^\ddagger$	—	+2.7	+6.6	+11.5
$\delta_m \mu^\theta (\text{S}_2\text{O}_8^{2-})$	—	+1.8	+8.4	+22
$\delta_m \mu^\theta (\text{Complex})$	—	-3.8	-5.6	-8.0
$\delta_m \mu^\theta (\text{IS})$	—	-2.0	+2.8	+14
$\delta_m \mu^\theta (\text{TS})$	—	+0.7	+9.4	+25

Table 4.6 Initial state-transition state analysis for the $\text{S}_2\text{O}_8^{2-}$ oxidation of $\text{Fe}(\text{CN})_2(\text{bipy})_2$ in water-DMSO mixtures (kJ mol^{-1} ; 298.2 K).

Vol % DMSO	0	20	40	60
$k_2 / \text{mol}^{-1} \text{ dm}^3 \text{ s}^{-1}$	0.129	0.104	0.063	0.046
$\delta_m \Delta G^\ddagger$	—	+0.5	+1.8	+2.6
$\delta_m \mu^\theta (\text{S}_2\text{O}_8^{2-})$	—	+1.8	+ 8.4	+22
$\delta_m \mu^\theta (\text{Complex})$	—	+3.2	+16.2	+30
$\delta_m \mu^\theta (\text{IS})$	—	+5.0	+24.6	+52
$\delta_m \mu^\theta (\text{TS})$	—	+5.5	+26	+55

Table 4.7 Initial state-transition state analysis for the $\text{S}_2\text{O}_8^{2-}$ oxidation of $[\text{Fe}(\text{CN})_4(\text{bipy})]^{2-}$ in water-DMSO mixtures (kJ mol^{-1} ; 298.2 K).

Vol % DMSO	0	20	40	60
$10^3 k_2 / \text{mol}^{-1} \text{dm}^3 \text{s}^{-1}$	2.1	12.0	22.5	2.5
$\delta_m \Delta G^\ddagger$	—	-4.3	-5.8	-0.3
$\delta_m \mu^\theta (\text{S}_2\text{O}_8^{2-})$	—	+1.8	+8.4	+22
$\delta_m \mu^\theta (\text{Complex})$	—	+0.1	+1.1	+2.0
$\delta_m \mu^\theta (\text{IS})$	—	+1.9	+9.5	+24
$\delta_m \mu^\theta (\text{TS})$	—	-2.4	+4.3	+24

Table 4.8 Initial state-transition state analysis for the $\text{S}_2\text{O}_8^{2-}$ oxidation of $[\text{Fe}(\text{CN})_4(\text{Me}_2\text{bsb})]^{2-}$ in water-DMSO mixtures (kJ mol^{-1} ; 298.2 K).

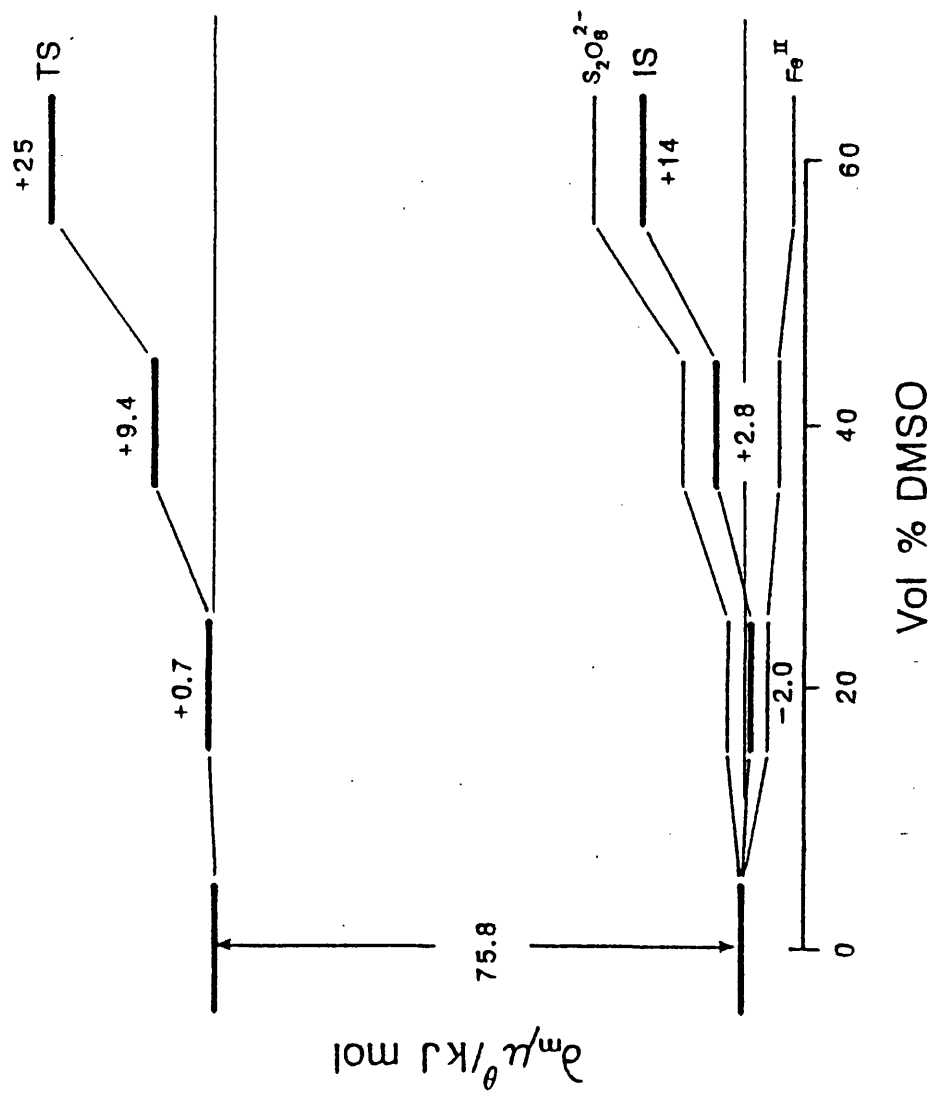


Figure 4.5 Initial state-transition analysis for the $\text{S}_2\text{O}_8^{2-}$ oxidation of $\text{Fe}(\text{CN})_2(\text{bipy})_2$ in water-DMSO mixtures.

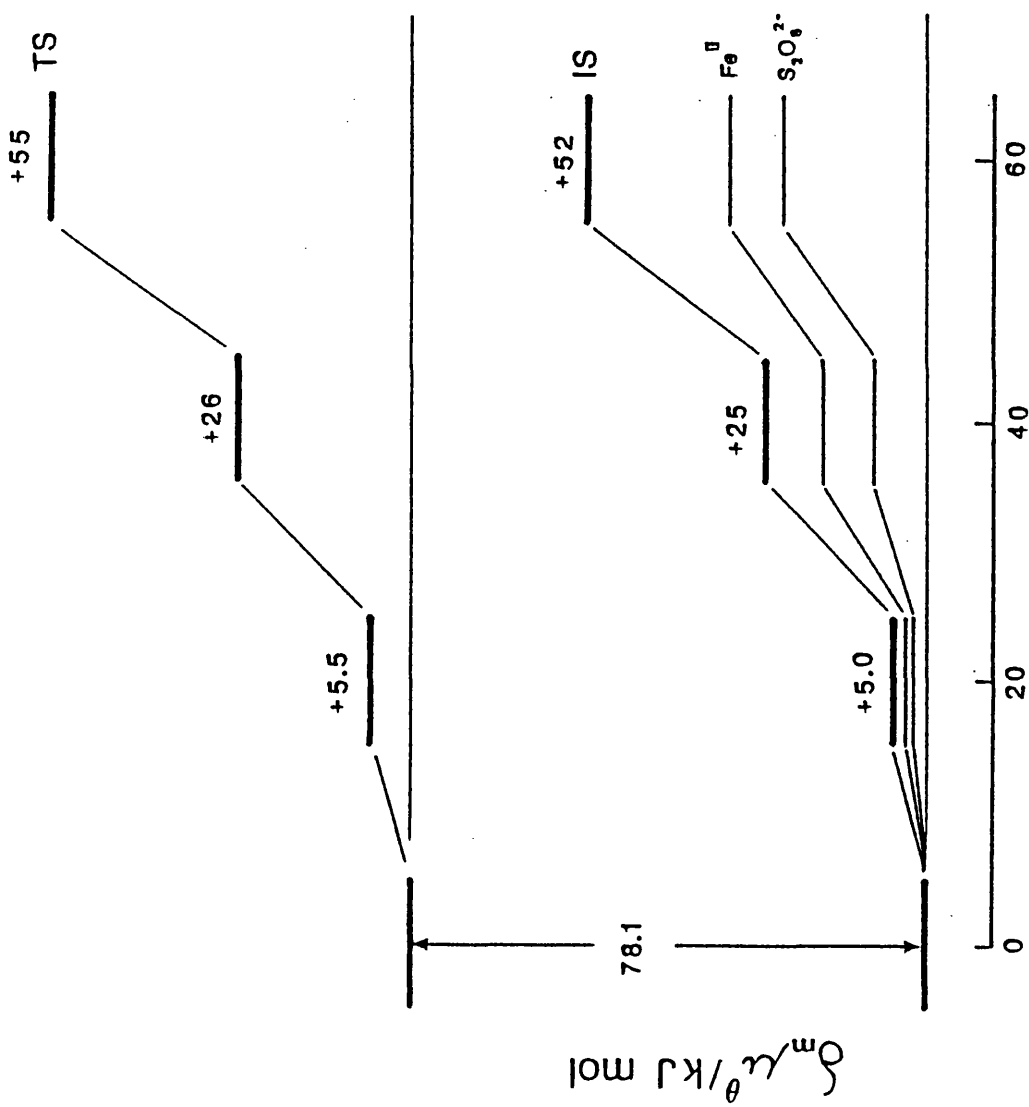
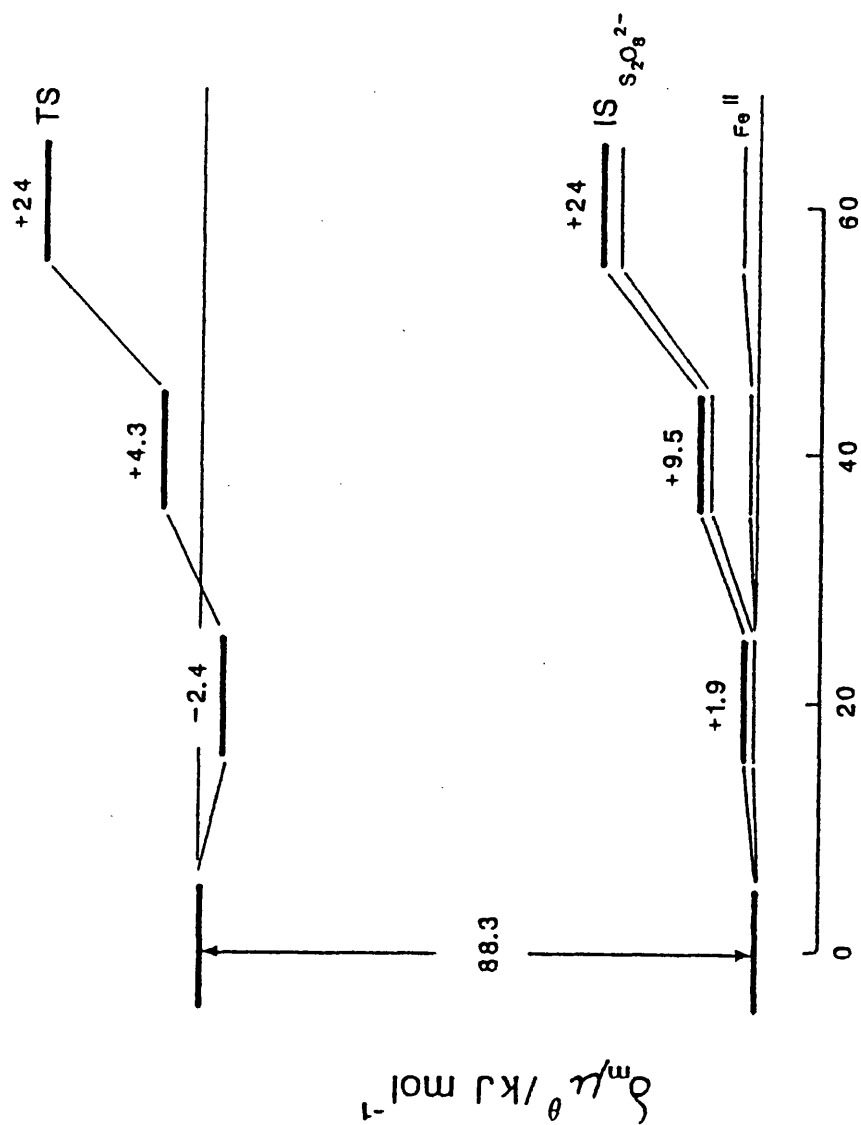


Figure 4.6 Initial state-transition analysis for the $\text{S}_2\text{O}_8^{2-}$ oxidation of $[\text{Fe}(\text{CN})_4(\text{bipy})]^{2-}$ in water-DMSO mixtures.



Vol % DMSO

Figure 4.7 Initial state-transition analysis for the $S_2O_8^{2-}$ oxidation
of $[Fe(CN)_4(Me_2bsb)]^{2-}$ in water-DMSO mixtures.

4.4 Concluding Remarks.

It is interesting to note that the second-order rate constant for $\text{S}_2\text{O}_8^{2-}$ oxidation varies directly with the formal iron(II)/(III) redox potentials (and hence inversely with ΔG^0) for the series of complexes given in Table 4.9. Particularly striking is the large drop in reactivity between $[\text{Fe}(\text{CN})_4(\text{bipy})]^{2-}$ and $[\text{Fe}(\text{CN})_6]^{4-}$. Assuming that the reactions are all approximately equally adiabatic, this trend could suggest that electron delocalisation on the diimine ligand in the charge transfer excited state may provide a low energy pathway via which the reaction could proceed. Consequently this would involve the specific orientation of the ternary complex with respect to the $\text{S}_2\text{O}_8^{2-}$ oxidant. Certainly the ability of such ligands to participate in bridge mediated inner-sphere electron transfer reactions is becoming apparent ^[140,141].

Complex ^a	E ^θ / V ^b	Ref.	k ₂ / mol ⁻¹ dm ³ s ⁻¹	Ref.
[Fe(bipy) ₃] ²⁺	1.29	[105]	0.73	[142]
[Fe(CN) ₂ (bipy) ₂]	1.02	[103]	0.33	^c
[Fe(CN) ₄ (bipy)] ²⁻	0.56	[104]	0.129	^c
[Fe(CN) ₆] ⁴⁻	0.36	[103]	0.03	[143]

^a Ligands are defined in text.

^b vs. NHE.

^c This work.

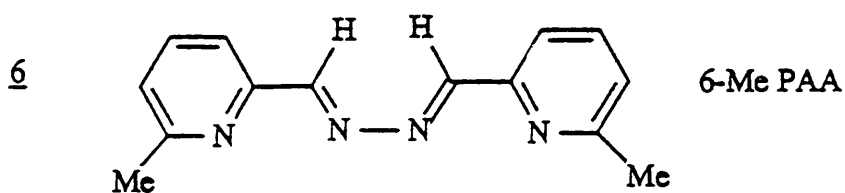
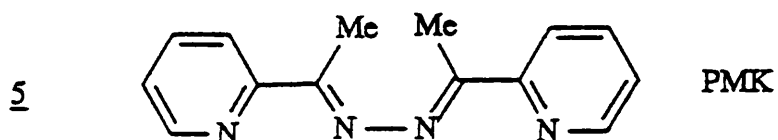
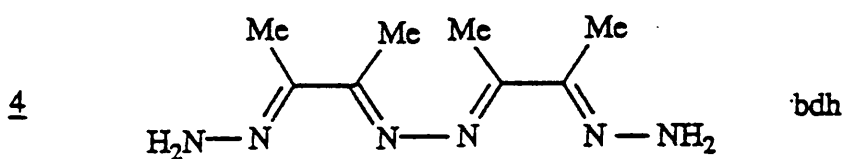
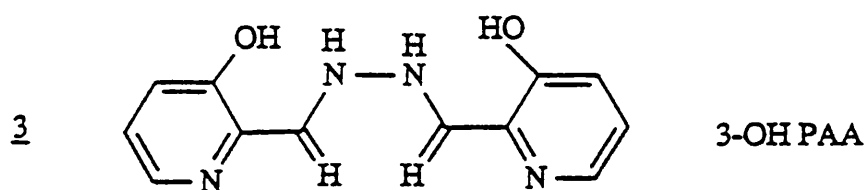
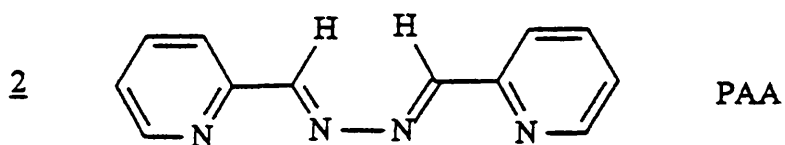
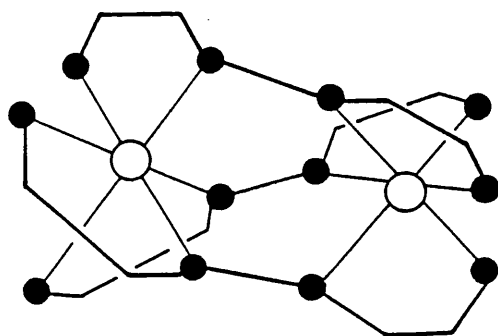
Table 4.9 Standard redox potentials for a selection of iron(II) complexes
with second order rate constants for S₂O₈²⁻ oxidation (298.2 K).

Chapter 5

*Structure and Solvation of
Binuclear Iron(II)-diimine complexes*

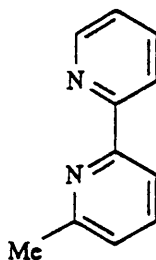
5.1 Introduction.

Several binuclear complexes of the general type (1) exist formed with a variety of terdentate ligands (2 to 6) [144–148].



The vast majority of these have been homometallic, and involved either Fe^{2+} , Co^{2+} , Ni^{2+} or Zn^{2+} cations. More recently, a series of mixed metal binuclear complexes ($[\text{MM}'(\text{pmk})_3]^{4+}$) have been reported ($\text{M} = \text{Zn}^{2+}$; $\text{M}' = \text{Co}^{2+}$, Cu^{2+} or Ni^{2+}) [149]. Such heterobimetallic complexes have become useful models with which to study the nuclear relaxation behaviour of paramagnetic metal ions. This is particularly interesting in the context of the work involved in this Thesis since it provides an alternative method to examine metal-metal interaction to that provided by the Robin and Day classification (cf. Chapter 6).

The stability of the iron(II) complexes formed by ligands (2 to 5) varies considerably. The 6-Me paa variant (6) was reported not to form a low-spin complex at all [148]. Presumably, the inter-methyl distortion is too large to permit close enough approach of the ligands to the metal to engender a low-spin environment. Similarly, the $[\text{Fe}(\text{6-Mebipy})_3]^{2+}$ [150] cation exhibits a low-spin \rightleftharpoons high-spin transition at ca. 89 K.



Low-spin iron(II) complexes are generally substitution inert as a consequence of high crystal field stabilisation energies, with maximum crystal field stabilisation in the ground state corresponding to octahedral geometry. For tris-diimine complexes considerable distortion away from accurate octahedral FeN_6 units can occur due to the relatively small bite of these diimine ligands. Ligands which are even more sterically demanding can force even greater distortion from octahedral geometry – particularly in semi- and fully-encapsulating

cage compounds. These changes in ligand structure affect reactivity through the usual electronic and steric effects but can also influence reactivity trends in binary aqueous solvent mixtures through hydrophobic and hydrophilic ligand-solvent interactions and consequent preferential solvation. The factors affecting these preferential solvation trends for mononuclear iron(II), cobalt(III), and chromium(III) complexes in mixed solvents is well established ^[68]. Data for binuclear complexes are, on the other hand, very sparse indeed.

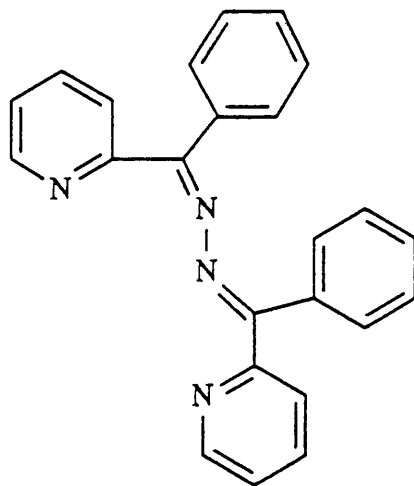
In the present Chapter the structure and solvation of several binuclear iron(II)-diimine complexes of the type shown below are examined and compared where possible with existing data on mononuclear iron(II), and binuclear cobalt(III) complexes.

5.2 Experimental.

The $[\text{Fe}_2(\text{paa})_3]^{4+}$ ^[144] cation was prepared from iron(II) chloride tetrahydrate, hydrazine and pyridine 2-aldehyde, and isolated as the PF_6^- and Cl^- salts. The $[\text{Fe}_2(\text{pmk})_3]^{4+}$ cation was generated by the published method ^[146] from iron(II) chloride, hydrazine and 2-acetyl pyridine, and isolated as the Cl^- , I^- , ClO_4^- and PF_6^- salts.

The attempted preparation of **5** via the initial isolation of the free ligand led to the formation of a blue complex ($\epsilon_{590} = 7 \times 10^3$). Repeating this preparation in the presence of an iron(II) template led to the initial formation of the blue solution. On prolonged standing (12 hours) a green solution prevailed ($\epsilon_{620} = 0.9 \times 10^3$) from which a solid was precipitated as the iodide and perchlorate salts. The iron analysis was consistent with the formulation $[\text{Fe}_2(\text{pbk})_3](\text{PF}_6)_4$.

Presumably, the preparation of the ligand in the absence of a metal template led to the formation of the *cis-trans* configuration (see below) because of the significant $\text{Ph} \leftrightarrow \text{Ph}$ steric crowding associated with the *cis-cis* form. Clearly this type of configuration is able to function as a tridentate ligand, as has been observed in the hydrolysis of the $[\text{Fe}_2(\text{pah})_3]^{4+}$ cation ^[144].



The sample of $[\text{Fe}_2(\text{pmk})_3]\text{I}_4$ used for the X-ray study was grown from a supersaturated aqueous solution as a red cubic crystal. The structure determination was performed by Dr D.R. Russell and Ms. M. Bassett.

The acquisition of high resolution NMR spectra of iron(II)–diimine complexes can be hampered by solubility restraints (and opposing sample microheterogeneity), decomposition to paramagnetic products and sample viscosity. Such complications dictate the choice of both counter-ion and solvent to maximise the quality of spectra. Previous studies on a wide range of mononuclear iron(II)–diimine complexes ^[151] found that the most suitable conditions were to use the PF_6^- salt and CD_3CN . Here however, due to the higher cation charge and greater probability to ion-pair a concentrated solution of the chloride salt in D_2O was used.

Spectra were recorded on a Bruker AM300 spectrophotometer operating at 300 MHz for ^1H and 75 MHz for ^{13}C , and at 298 K. Chemical shifts are reported relative to a DSS internal standard.

Complex solubilities were determined in the manner outlined in Section 2.4.2 except for those containing the $[\text{Fe}_2(\text{pmk})_3]^{4+}$ cation which was slightly unstable in some of the media used. As a result, solubilities were determined more rapidly ($\frac{1}{4}$ hour) from a rapidly stirred thermostatted solution. Concentrations were determined spectrophotometrically (Pye–Unicam SP 8–100). Samples of the binuclear cobalt(III) complexes were kindly supplied by Prof. T. P. Dasgupta and K. A. Rashid.

5.3 Results and Discussion.

5.3.1 Crystal Structure.

The X-ray diffraction data for $[\text{Fe}_2(\text{pmk})_3](\text{I})_4 \cdot 3\text{H}_2\text{O}$ are set out in Appendix C. Selected bond lengths and angles are included in Table 5.1 which also includes relevant data for related iron(II)–diimine complexes.

In an analogous manner to $[\text{Co}_2(\text{pmk})_3]^{4+}$ the metal centres are coordinated in an approximately octahedral environment as can be seen in Figure 5.1. The geometry at each iron is *fac* with the three pyridyl nitrogens defining one octahedral face and the three bridging nitrogens the other. Table 5.1 includes skew and bond angles, and bond length data for $[\text{Fe}_2(\text{pmk})_3]^{4+}$ and related complexes. (See Figure 5.2 for ligand formulae)

The bite of the diimine moiety $\text{N}=\text{C}-\text{C}=\text{N}$ is slightly less than 90° producing a small but significant distortion towards trigonal prismatic geometry. This is further highlighted when one looks at the skew angles of 47° and 52° (between faces 1 and 2, and between 3 and 4) respectively (Figure 5.3). These skew angles are intermediate between those for the relatively unhindered $[\text{Fe}(\text{LL})_3]^{2+}$ ($\text{LL} = \text{bipy}, \text{phen}, \text{gmi}, \text{bmi}$) complexes which are close to octahedral ($\alpha = 55^\circ$), and the more sterically constrained cage complexes, $[\text{Fe}(\text{C}_3\text{N}_3\text{cxcage})]^{2+}$ and $[\text{Fe}(\text{Bcxcage})]$, where $\alpha = 22^\circ$ and 0° respectively.

The $\text{N}_1-\text{C}_5-\text{C}_6-\text{N}_2$ and $\text{N}_4-\text{C}_{15}-\text{C}_{16}-\text{N}_3$ torsional angles within the pmk ligand system are 3° . Each five membered chelate ring is therefore essentially co-planar with the corresponding pyridine ring. In contrast, the $\text{N}_1-\text{C}_5-\text{C}_6-\text{C}_7$ and $\text{N}_4-\text{C}_{15}-\text{C}_{16}-\text{C}_{17}$ torsional angles are ca. 8° , with the methyl groups bent out of this plane. This is consistent with a significant degree of inter-methyl group distortion. The distortion in the $[\text{Fe}_2(\text{pmk})_3]^{4+}$ cation, due

to steric methyl \leftrightarrow methyl repulsion is constrained more than in the Co(II) analogue ($\alpha = 42^\circ$) by the greater CFSE for the iron(II) centre.

The C—N_{pyridyl} bond lengths are 1.36 Å are considerably longer than the C—N_{azide} bonds (1.29 Å), reflecting significantly more double bond character for the latter (cf. 1.37 Å for pyridine; C=N = 1.27 Å [111]).

From Table 5.1 it is evident that iron–nitrogen bond lengths span only the small range of 1.90 to 1.99 Å – reflecting contributions from σ and π effects as well as geometric restraints of some of the ligands. A similar division to that mentioned above can be seen for the Fe—N bonds. The Fe—N_{pyridyl} bonds (1.98 Å) are shorter than the Fe—N_{azide} bonds (1.92 Å), a trend that is consistent with mononuclear analogues involving the apmi, hxsBH, and tripod ligands (see Scheme 5.1 for formulae).

Some measure of metal–ligand delocalisation should be provided by C—N bond lengths, although complications arise because of ligand asymmetry (*vide supra*). Probably the best reflection of delocalisation is provided by the imine C—C bond lengths in the chelate ring – although the small range of C—C bond lengths makes this rather insensitive. Using this criterion however, the degree of delocalisation in the [Fe₂(pmk)₃]⁴⁺ cation is similar to that in [Fe(bipy)₃]²⁺, but less than in [Fe(phen)₃]²⁺.

The choice of the C—C bond lengths as the best criterion to describe the extent of metal–ligand delocalisation is reinforced when comparisons are made between the cobalt and iron binuclear complexes. The C—N bonds in the [Co₂(pmk)₃]⁴⁺ cation are comparable to those in the iron analogue. In contrast, the C—C bond lengths are significantly longer in the Co(II) complex, reflecting the less effective π_d –L π^* donation for the d⁷ cobalt centre.

Complex ^a	Bond lengths / Å			Bond angles		Ref.
	Fe—N	N—C	C—C	N—Fe—N	α ^b	
[Fe(bipy) ₃] ²⁺	1.96–1.99	1.34–1.35	1.42–1.48	82	55	[114]
[Fe(phen) ₃] ²⁺	1.96–1.98	1.31–1.39	1.38	83	55	[115]
[Fe(gmi) ₃] ²⁺	1.95	1.27	1.42	80	53	[117]
[Fe(bmi) ₃] ²⁺	1.96	1.29	1.48	79.5	53	[117]
[Fe(apmi) ₃] ²⁺	1.93–1.96	1.28,1.35	1.45	80	54	[152]
[Fe(bqdi) ₃] ²⁺	1.90–1.92	1.29–1.32	1.45–1.46	79	40	[118]
[Fe(hxsbH)] ²⁺	1.87–1.97	1.31,1.36	1.43	81–86	–	[109]
[Fe(tripod)] ²⁺	1.95–1.99	1.28–1.38	1.44	81–82	54	[153]
[Fe(C ₃ N ₃ cx cage)] ²⁺	1.90–1.93	1.26–1.29	1.43–1.45	77–79	22	[116]
[Fe(Bcx cage)] ²⁺	1.87–1.96	1.18–1.47	1.47	76	–	[112]
[Fe ₂ (pmk) ₃] ⁴⁺	1.93–1.98	1.29–1.35	1.44–1.47	80	47,52	c
[Co ₂ (pmk) ₃] ⁴⁺	–	1.25–1.39	1.42–1.58		42	[154]

^a Ligand formulae shown in Fig. 5.2.

^b Defined in Fig. 5.3.

^c This work.

Table 5.1 Bond lengths and angles for the [Fe₂(pmk)₃]⁴⁺ cation
and for iron(II)–diimine analogues.

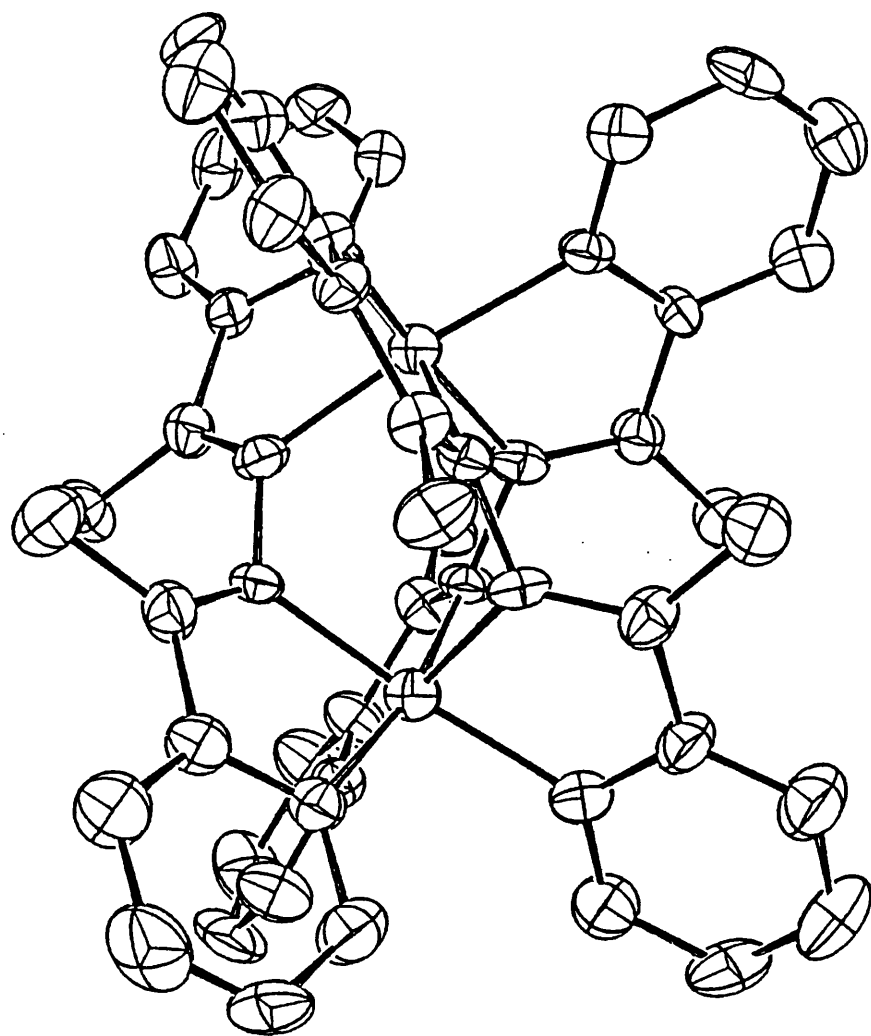


Figure 5.1 Perspective view of the $[\text{Fe}_2(\text{pmk})_3]^{4+}$ cation.

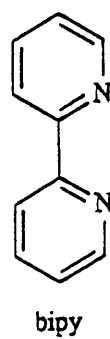
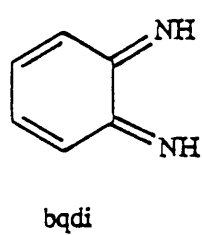
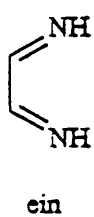
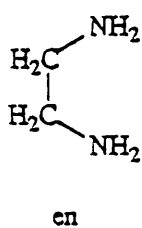
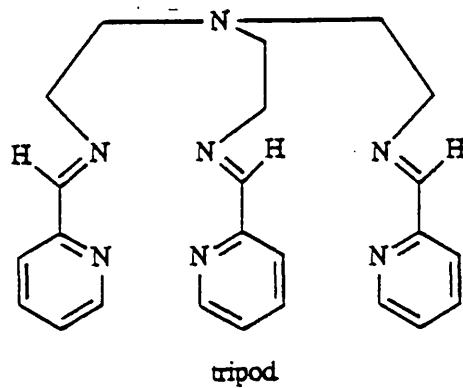
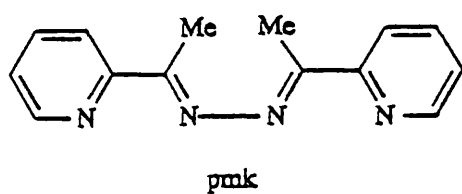
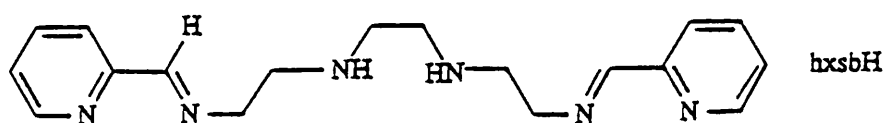
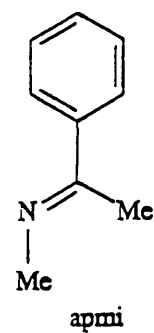
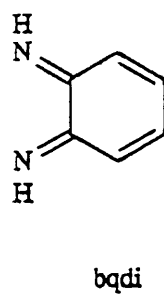
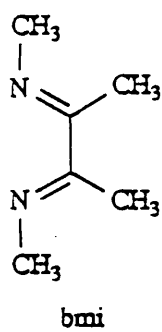
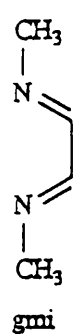


Figure 5.2 General ligand formulae.

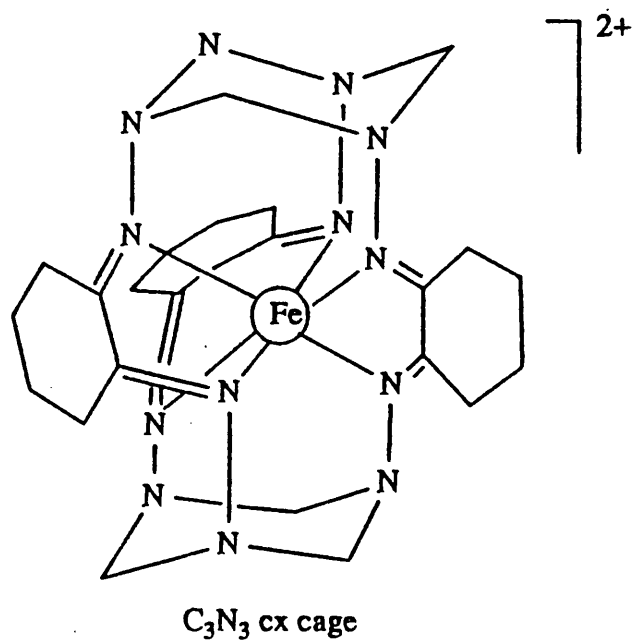
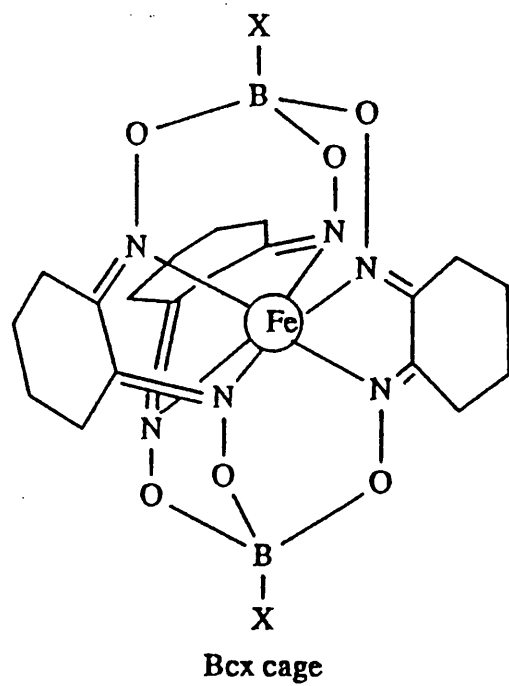


Figure 5.2 (cont.) General ligand formulae.

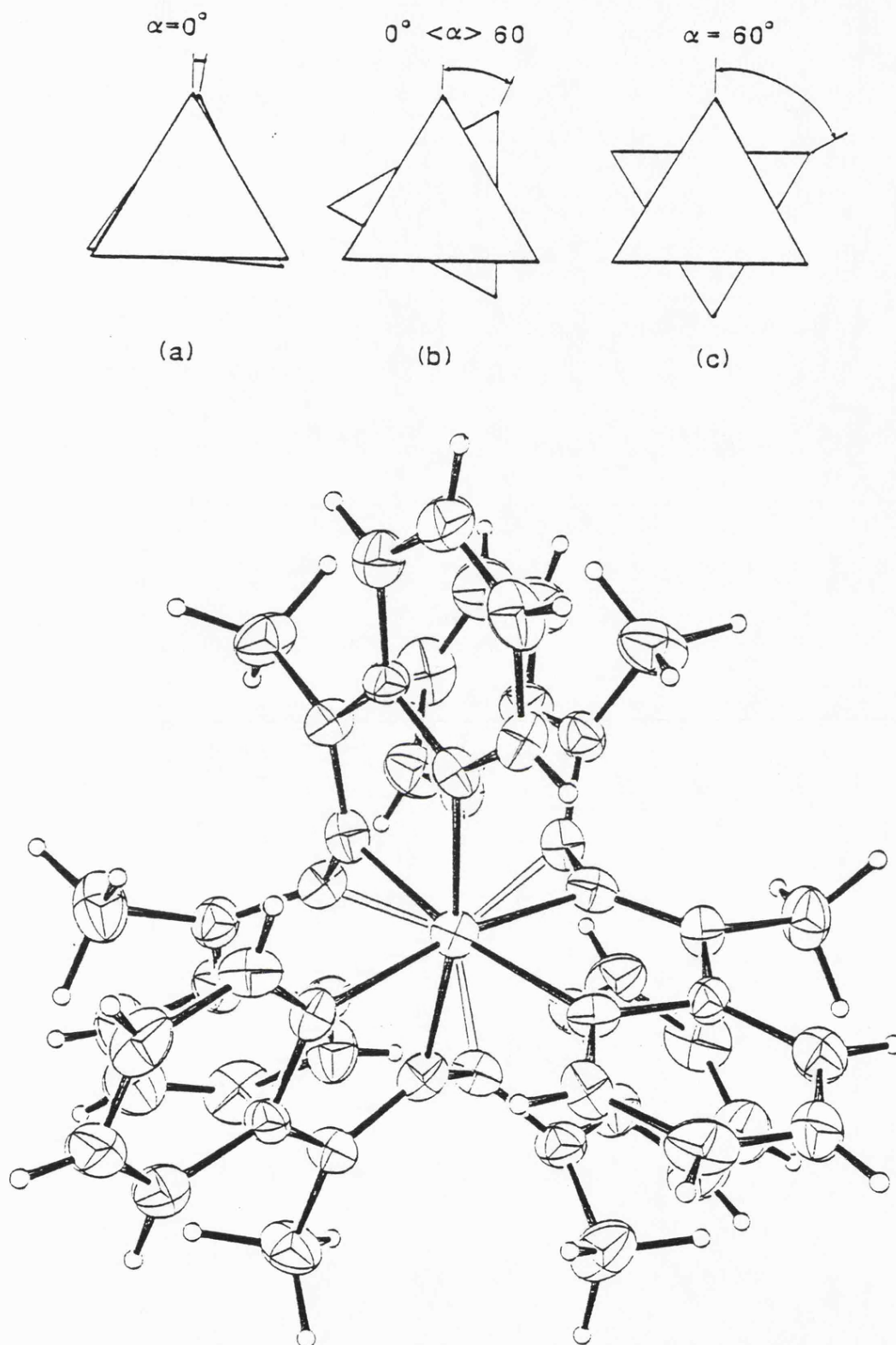


Figure 5.3 Illustration of the skew angles in the $[\text{Fe}_2(\text{pmk})_3]^{4+}$ cation.

5.3.2 Solution NMR.

Peak assignment in NMR spectra is most often achieved using empirical correlation tables. Advances in equipment and in theoretical aspects of Fourier transform NMR spectroscopy have led to the development of new pulse sequences and spin-decoupling techniques. Such advances have enabled the detailed assignment of complex structures, and have proved particularly useful in detailing the reactivity of coordinated ligands [155].

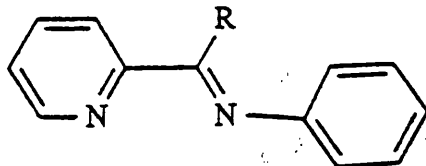
The ^1H NMR spectrum of $[\text{Fe}_2(\text{pmk})_3]^{4+}$ is shown in Figure 5.4, from which the methyl groups can be immediately assigned as the (3H) singlet at 1.49 ppm. The 3 other multiplets centred at 7.8 ppm (2H), 7.4 ppm (1H) and 7.2 ppm (1H) are the remaining 4 pyridyl protons (H_a to H_d).

The BBD ^{13}C and $^{13}\text{C} \leftrightarrow ^1\text{H}$ DEPT spectra are shown in Figure 5.5. Again, the methyl group is easily assigned as the signal at 13.12 ppm. The quaternary imine carbons (H_e and H_f) can be extracted from the DEPT spectrum as the peaks at 177.69 ppm and 158.30 ppm respectively, with the protonated carbons (H_a to H_d) accounting for the remaining peaks. The saturation of the methyl signal at 48 Hz (1.49 ppm) resulted in a negative (phase) enhancement of the peak at 7.40 ppm in the NOE difference spectrum and, on the basis of this, this peak can be assigned as that of proton H_d . From the $^1\text{H} \leftrightarrow ^1\text{H}$ COSY spectrum (Figure 5.6) it is possible to further assign the signal at 7.25 ppm as that of proton H_c . This multiplet appears as a triplet of doublets (dt), rather than the doublet of doublet of doublets (ddd) as one would intuitively expect. This is due simply to equal coupling to protons H_b and H_d ($J_{b \leftrightarrow c} = J_{c \leftrightarrow d} = 4.5$ Hz), split further by coupling to H_a ($J_{a \leftrightarrow c} = 2$ Hz).

Unfortunately, due to the virtual superimposition of the resonances of H_a

and H_b , deconvolution of the multiplet is not possible beyond the reciprocal of those coupling constants already mentioned. The chemical shifts can be seen more clearly from the $^{13}\text{C} \leftrightarrow ^1\text{H}$ correlation (Figure 5.7) as peaks at 7.81 ppm and 7.85 however ¹ – and can be tentatively assigned on the basis of previous spectra ^[151] to be H_a and H_b respectively. The ^{13}C and ^1H NMR data are summarised in Table 5.2

Some insight into the intramolecular motion of co-ordinated diimine ligands has been provided using NMR spectroscopy. In particular, for a series of tris diimine cations, $[\text{Fe}(\text{LL})_3]^{2+}$, the fluxionality of the N-phenyl ring was shown to be dependent on the size of R



Free rotation was observed for $R = \text{H}$, but was restricted for more sterically demanding groups such as Me and Ph ^[151].

In the present case, and although considerable steric methyl \leftrightarrow methyl strain is highlighted from the crystal structure, no evidence of restricted rotation is seen in the ^1H spectrum, with the methyl resonances appearing as singlets.

¹extrapolated from the centre of the 2D contour

Complex	Chemical shift /ppm						
	Methyl	A	B	C	D	E	F
$[\text{Fe}_2(\text{pmk})_3]^{4+}$ ^1H	1.49	7.81	7.85	7.25	7.40	-	-
	^{13}C 13.12	131.7	142.6	131.9	153.2	177.69	158.30
$[\text{Zn}_2(\text{pmk})_3]^{4+}$ ^1H	2.1	8.75	8.0	8.5	8.4	-	-

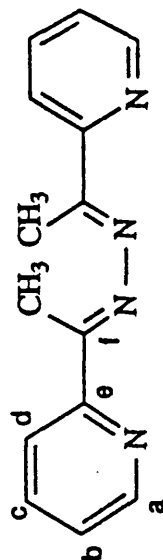


Table 5.2 ^1H and ^{13}C data for the $[\text{Fe}_2(\text{pmk})_3]^{4+}$ cation including ^1H data for the Zn^{2+} cation [149].

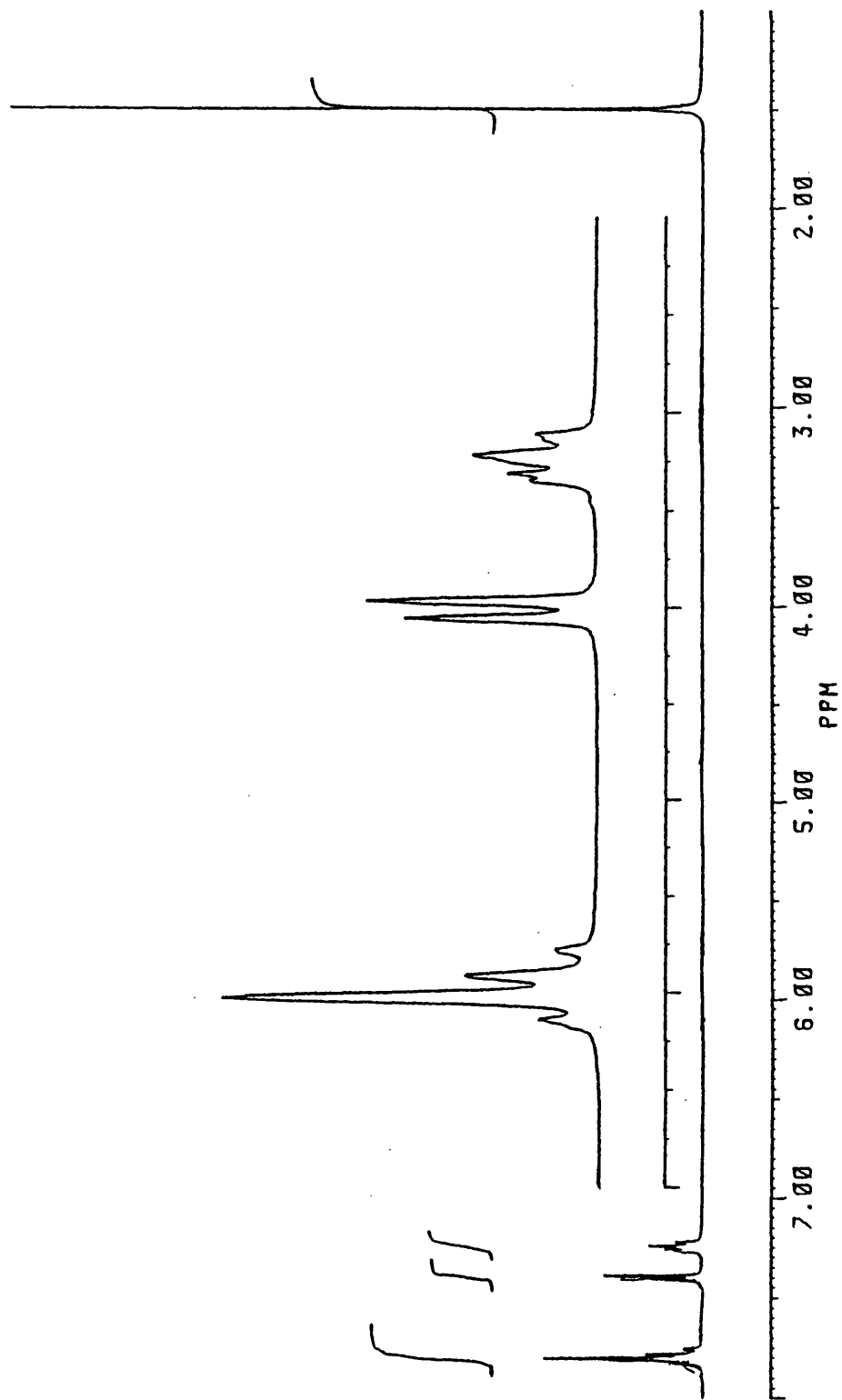


Figure 5.4 ^1H nmr spectrum of the $[\text{Fe}_2(\text{pmk})_3]^{4+}$ cation.

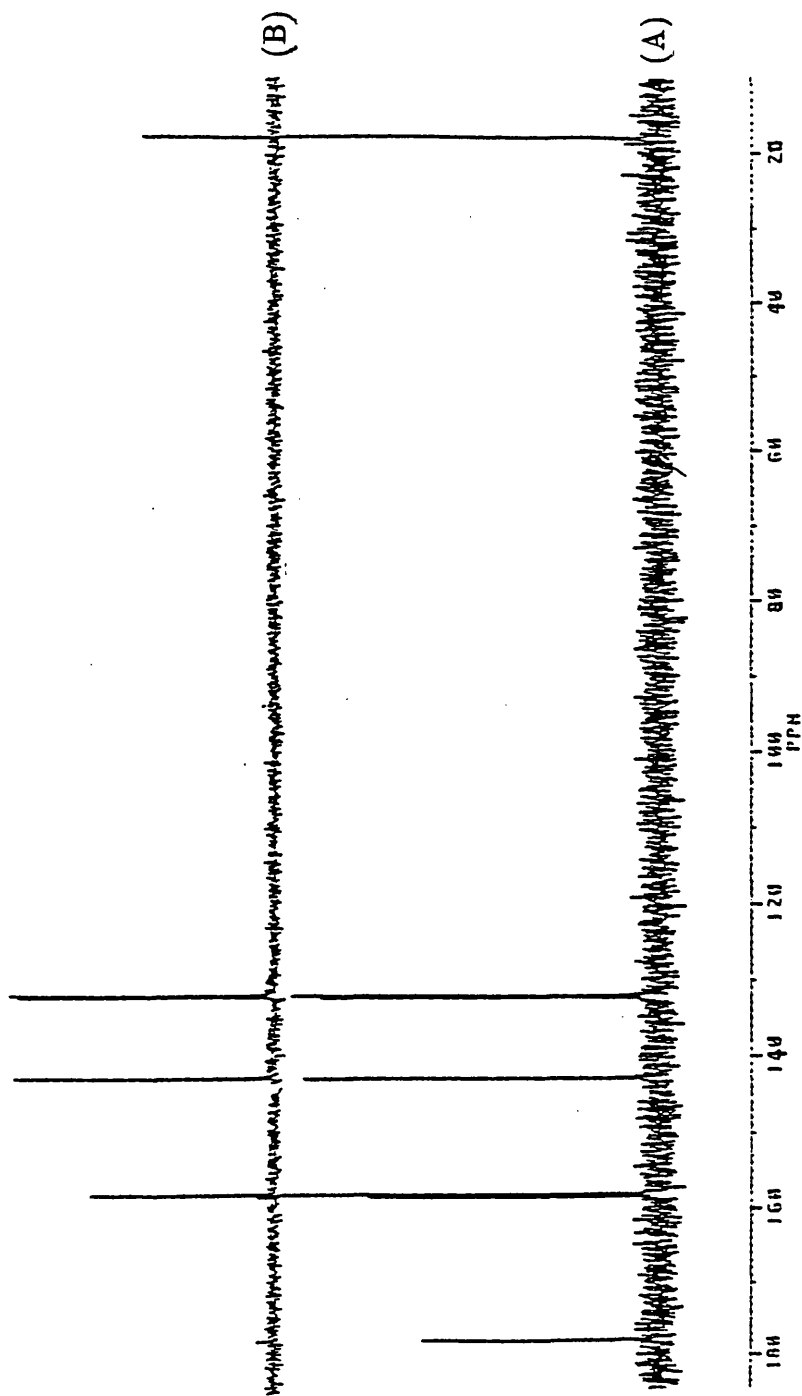


Figure 5.5 ^{13}C BBD (A) and DEPT (B) spectra of the $[\text{Fe}_2(\text{pmk})_3]^{4+}$ cation.

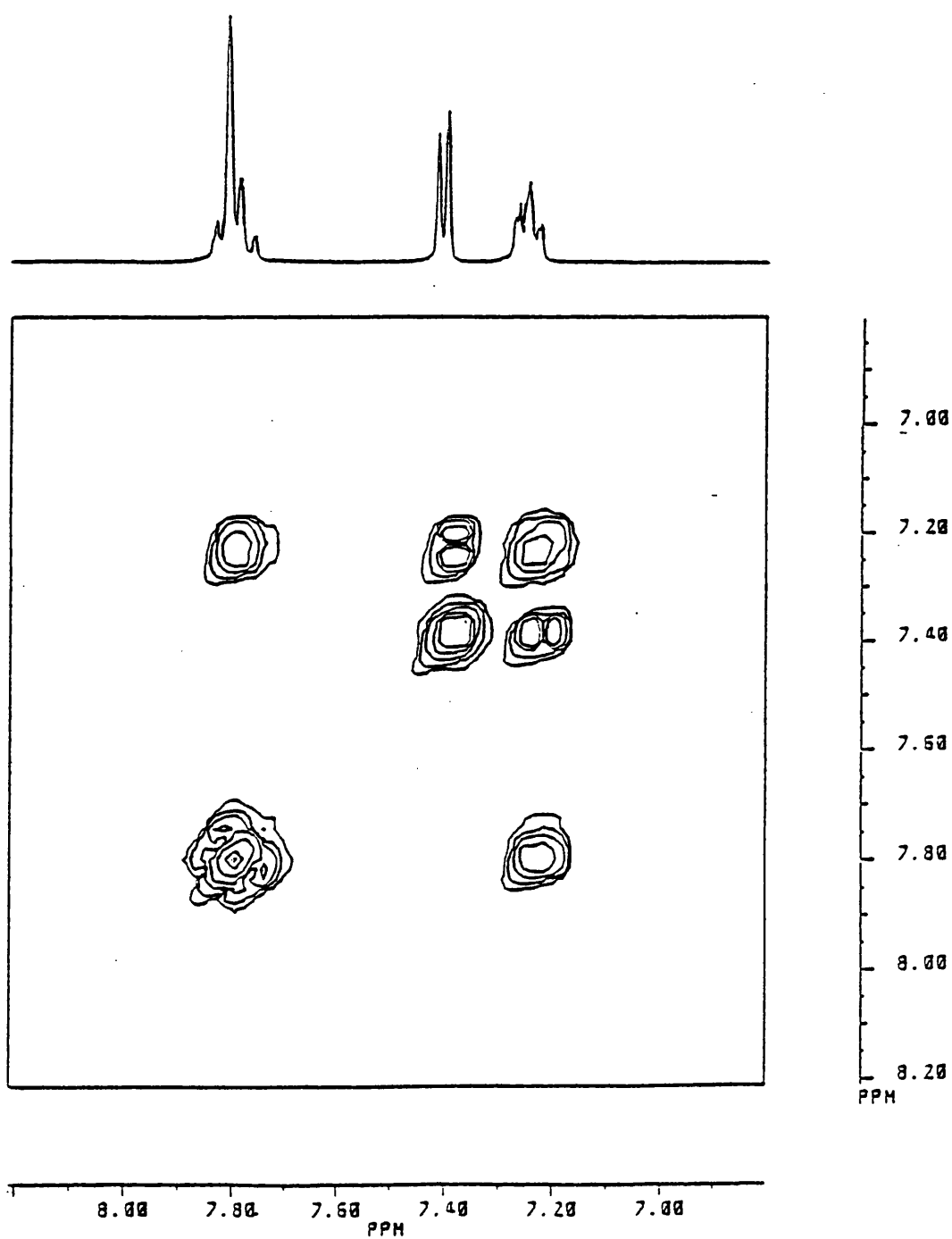


Figure 5.6 $^1\text{H} \leftrightarrow ^1\text{H}$ COSY spectrum of the $[\text{Fe}_2(\text{pmk})_3]^{4+}$ cation.

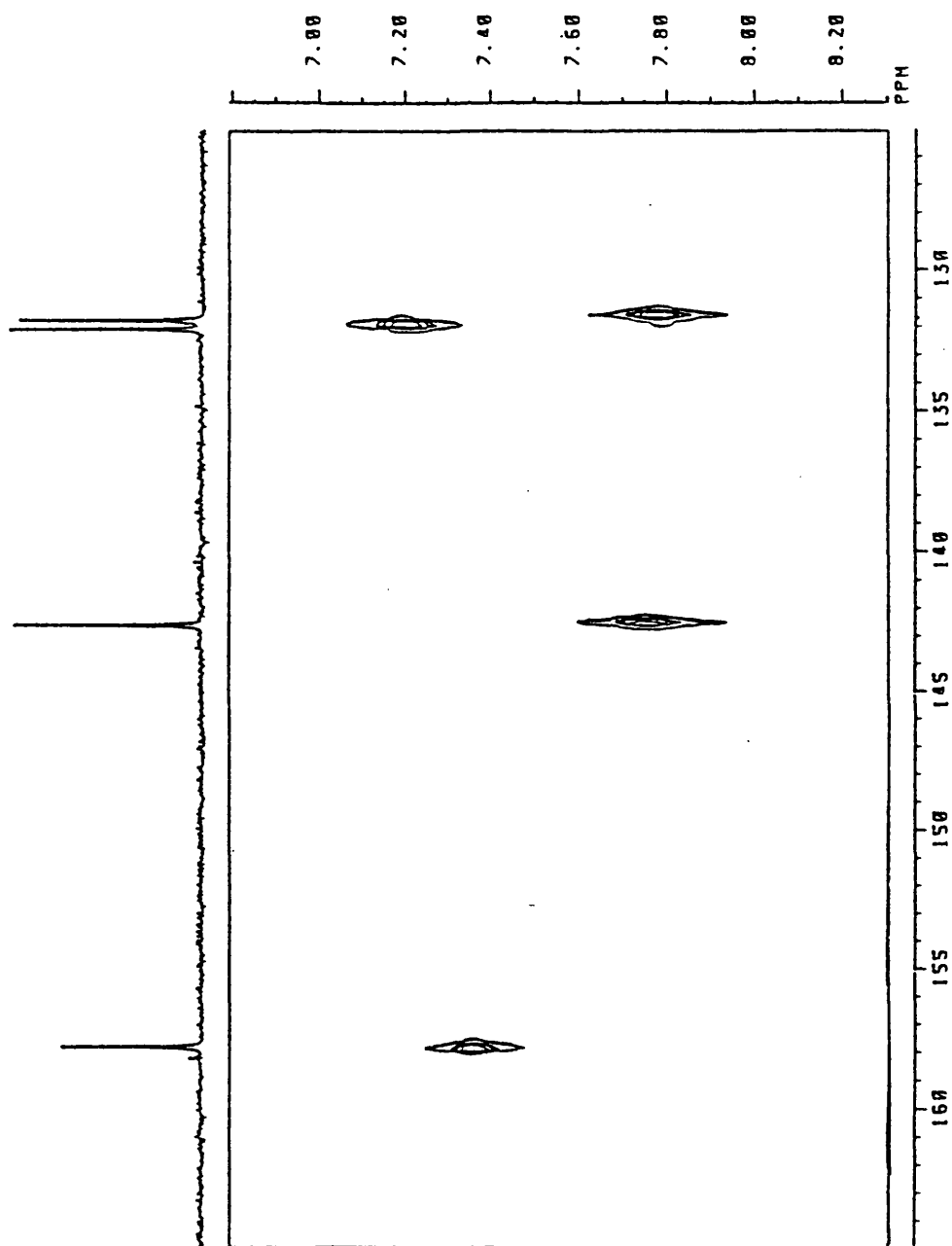


Figure 5.7 $^1\text{H} \leftrightarrow ^{13}\text{C}$ COSY spectrum of the $[\text{Fe}_2(\text{pmk})_3]^{4+}$ cation.

5.3.3 Metal–metal Interaction.

Crystallographic structural data have been of considerable benefit when examining the extent of metal–metal interaction in polymetallic mixed valence complexes.

In the present case the degree of interaction would be expected to be significant because of the fully conjugated nature of the ligand framework, and also the close proximity of the metal centres ($\text{Fe—Fe} = 3.47 \text{ \AA}$) – especially when one considers that there is significant interaction across 7.65 \AA in the binuclear $[\text{Fe}_2(\text{Mebpy-bpyMe})_3]^{4+}$ cation ^[156].

The N—N azide bond length is probably the best parameter to gauge the extent of this interaction for the $[\text{Fe}_2(\text{pmk})_3]^{4+}$ cation. Table 5.3 therefore includes this and other relevant data.

Bond type	Molecule	N—N / \AA	Ref.
N—N	hydrazine	1.45	[111]
N=N		1.20	[111]
N—N	$[\text{Fe}(\text{bdh})_3]^{2+}$	1.39	[112]
N—N	$[\text{Co}_2(\text{pmk})_3]^{4+}$	1.43 (av.)	[154]
N—N	$[\text{Fe}_2(\text{pmk})_3]^{4+}$	1.42	^a

^a This work.

Table 5.3 Selected N—N bond lengths.

Using this criterion, the bridging N—N bond in both the iron(II) and cobalt(II) complexes appears to be a single bond, with rather surprisingly, very little apparent delocalisation between the metal centres.

5.3.4 Solvation.

The dependences of absorption of saturated solutions on solvent composition for the perchlorate salt of the $[\text{Fe}_2(\text{pmk})_3]^{4+}$ cation for aqueous DMSO are given in Table 5.4. Also included in this Table are the derived transfer chemical potentials for the $[\text{Fe}_2(\text{pmk})_3]^{4+}$ cation.

The transfer chemical potential trends for the $[\text{Fe}_2(\text{pmk})_3]^{4+}$ cation in DMSO–water mixtures are illustrated in Figure 5.8. This Figure also includes data for a wide variety of mononuclear iron(II) complexes for comparison ^[75].

The $[\text{Fe}_2(\text{pmk})_3]^{4+}$ cation is quite dramatically stabilised as the DMSO content of the solution increases. The magnitude of this stabilisation is rather greater than one would predict, and is greater than that for complexes with considerably more hydrophobic character. Also included in Figure 5.8 is the trend for the ‘mononuclear equivalent’, $[\text{Fe}(\text{pmk})_{1.5}]^{2+}$. This fits slightly better into the overall picture, but even this is still slightly more stabilised than the more hydrophobic $[\text{Fe}(\text{phen})_3]^{2+}$ cation.

Vol % DMSO :	0	20	40	60
$[\text{Fe}_2(\text{pmk})_3](\text{ClO}_4)_4$				
Abs.sat.soln.	31	88	163	446
$\delta_m \mu^\theta$ (salt)	—	-12.9	-20.6	-33.0
$4\delta_m \mu^\theta (\text{ClO}_4^-)^a$	—	+2.8	+5.2	+6.8
$\delta_m \mu^\theta$ (cation)	—	-16	-26	-40

^a Taken from ref. [75].

Table 5.4 Solubilities and transfer chemical potentials for $[\text{Fe}_2(\text{pmk})_3]^{4+}$
in water-DMSO mixtures (kJ mol^{-1} ; 298.2 K).

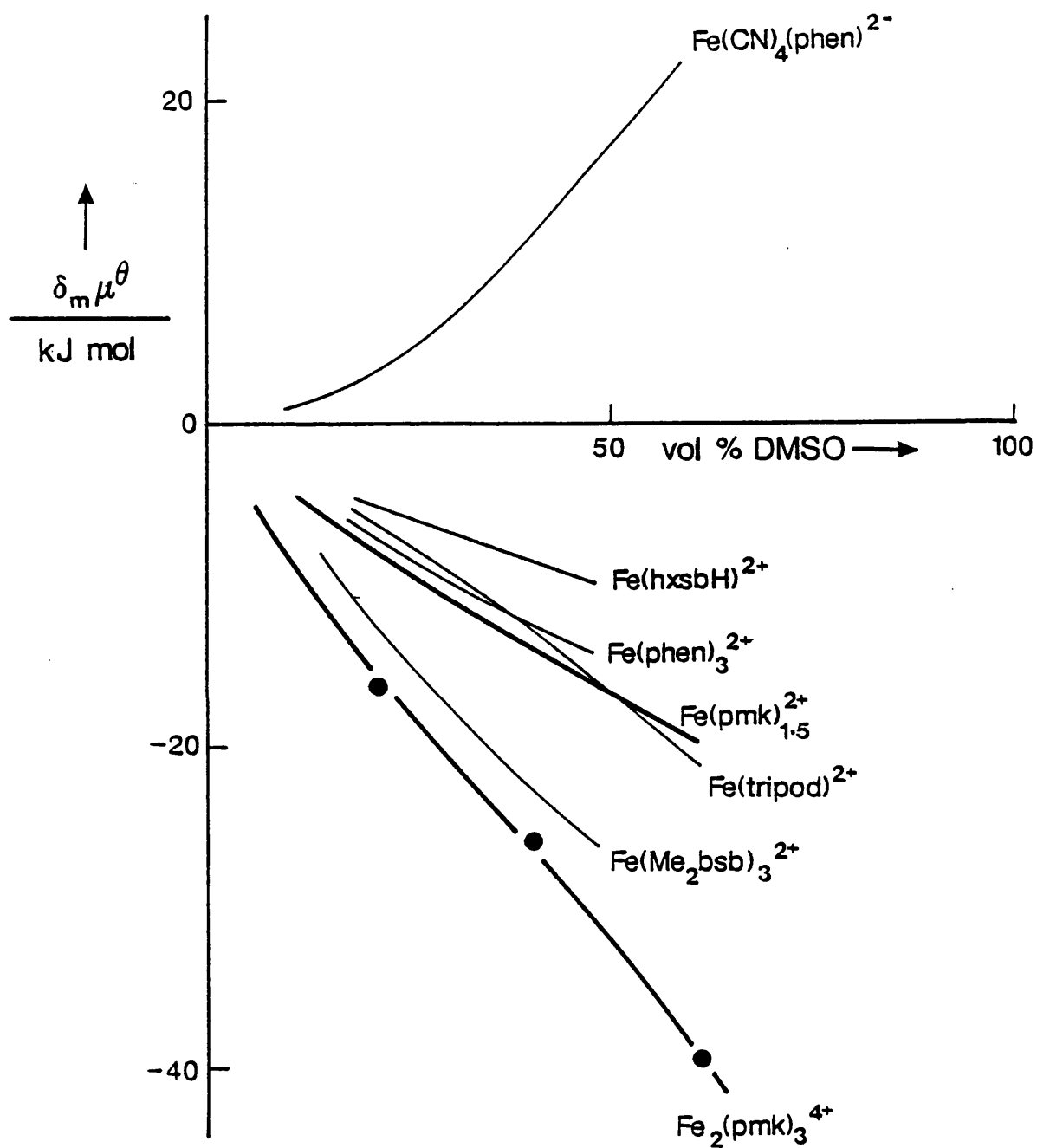


Figure 5.8 Transfer chemical potential trends for the binuclear iron(II) complexes in DMSO–water mixtures ($T = 298.2 \text{ K}$).

The solubilities and derived transfer chemical potential data for the perchlorate and iodide salts of the $[\text{Fe}_2(\text{pmk})_3]^{4+}$ for methanol–water mixtures are given in Table 5.5. The transfer chemical potential trends are shown in Figure 5.9, with data for comparison ^[164A].

The agreement between the data obtained for the two salts in methanol is reasonable up to 60% methanol, but considerably less so for 80% and 100%. The results in these media are dependant not only on the assumption about negligible ion–pairing but also on the accuracy of the transfer chemical potential data for the iodide and perchlorate counter–ions. Any error in these is multiplied four times when transmitted to the value derived for the cation.

Rather surprisingly, the $[\text{Fe}_2(\text{pmk})_3]^{4+}$ cation is destabilised on transfer from water to water–methanol mixtures. The extent of this destabilisation is of a similar magnitude to that seen for more hydrophilic species such as $[\text{Fe}(\text{CN})_4(\text{bipy})]^{2-}$ and even $[\text{Fe}(\text{CN})_5(\text{NO})]^{2-}$. The hydrophilicity conferred by the 4+ charge must therefore overwhelm the hydrophobicity of the essentially hydrocarbon periphery. It may be that solvent structural effects are of greater significance for these exceptionally large complex ions. Measured solvation trends may therefore be significantly different from those extrapolated from mononuclear analogues.

Iron(II) chemistry is clearly an area which, at present, is unable to provide a sufficient variety of stable binuclear complexes to probe solvation trends. A relatively wide variety of binuclear Co(III) complexes exist ^[157], and transfer chemical potential trends for several such complexes in methanol–water mixtures are given in Table 5.6, and illustrated in Figure 5.10.

The trends shown in this Figure are generally consistent with the charge and hydrophobic/hydrophilic criteria used for mononuclear analogues. Thus,

the highly hydrophilic $[(\text{ox})_2\text{Co}(\mu\text{-OH})_2\text{Co}(\text{ox})_2]^{4-}$ anion is quite dramatically destabilised on addition of methanol.

Several rather encouraging trends can be seen from this Figure when one compares mono- and binuclear complexes. Firstly, trends for $[(\text{H}_3\text{N})_3\text{Co}(\mu\text{-CO}_3)(\mu\text{-OH})_2\text{Co}(\text{NH}_3)_3]^{2+}$ and $[(\text{H}_3\text{N})_4\text{Co}(\mu\text{-NH}_2)(\mu\text{-OH})\text{Co}(\text{CO}_3)_2]$, a rather similar pair of binuclear species, are close to that for 2 moles of their mononuclear analogue $[\text{Co}(\text{NH}_3)_4(\text{CO}_3)]^+$. The difference between the trends for the $[(\text{H}_3\text{N})_4\text{Co}(\mu\text{-NH}_2)(\mu\text{-OH})\text{Co}(\text{NH}_3)_4]^{4+}$ binuclear complex and its dien analogue is similar to that between the trends for $[\text{Co}(\text{NH}_3)_6]^{3+}$ and $[\text{Co}(\text{en})_3]^{3+}$.

Trends for a considerably larger range of binuclear complexes need to be established before detailed understanding is achieved. In particular, groups in terminal and bridging positions may have significantly different affects.

Vol % MeOH :	0	20	40	60	80	100
$[\text{Fe}_2(\text{pmk})_3](\text{ClO}_4)_4$						
Abs.sat.soln.	5.25	3.47	2.56	1.98	1.67	0.165
$\delta_m \mu^\theta$ (salt)	—	+5.2	+8.9	12.1	14.1	42.9
$4\delta_m \mu^\theta (\text{ClO}_4^-)^a$	—	+0.4	-0.8	2.4	+9.2	+25.2
$\delta_m \mu^\theta$ (cation)	—	+4.8	+9.7	+9.7	+4.9	+17.7
$[\text{Fe}_2(\text{pmk})_3](\text{I})_4$						
Abs.sat.soln.	27.5	20.1	14.7	7.65	2.14	0.40
$\delta_m \mu^\theta$ (salt)	—	+3.9	+7.8	+15.9	+31.6	+52.4
$4\delta_m \mu^\theta (\text{I}^-)^a$	—	-0.4	+0.8	+4.0	+13	+28
$\delta_m \mu^\theta$ (cation)	—	+4.2	+7.0	+11.9	+19	+24
Mean $\delta_m \mu^\theta$ (cation)	—	+4.6	+8.4	+10.8	+12	+21

^a Taken from ref. [40].

Table 5.5 Solubilities and transfer chemical potentials for $[\text{Fe}_2(\text{pmk})_3]^{4+}$
in water–MeOH mixtures (kJ mol⁻¹; 298.2 K).

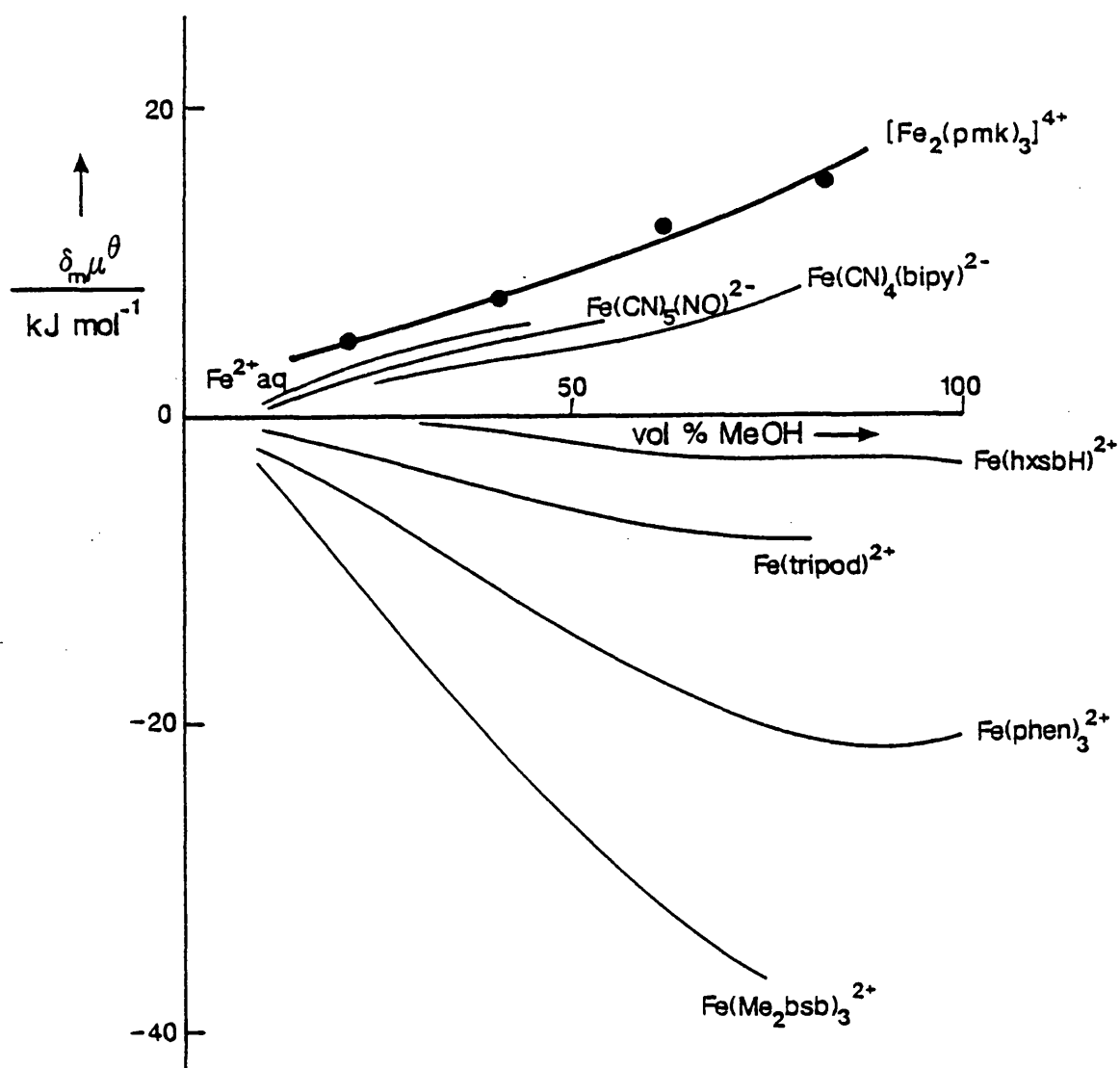


Figure 5.9 Transfer chemical potentials trends for the binuclear iron(II) complexes in water-methanol mixtures.

Vol % MeOH :	0	20	40	60
$[(\text{H}_3\text{N})_4\text{Co}(\mu\text{-NH}_2)(\mu\text{-OH})\text{Co}(\text{NH}_3)_4](\text{Cl})_4$				
$\delta_m\mu^\theta$ (salt)	—	+9.4	+20.4	+52.5
$\delta_m\mu^\theta$ (Cl^-) ^a	—	+0.8	+2.0	+7.5
$\delta_m\mu^\theta$ (cation)	—	+6.2	+12	+23
$[(\text{H}_3\text{N})_3\text{Co}(\mu\text{-OH})_2(\mu\text{-CO}_3)\text{Co}(\text{NH}_3)_3](\text{ClO}_4)_2$				
$\delta_m\mu^\theta$ (salt)	—	+8.6	+11.5	+18.5
$\delta_m\mu^\theta$ (ClO_4^-) ^a	—	+0.1	-0.1	+0.3
$\delta_m\mu^\theta$ (cation)	—	+8.4	+11.7	+17.9
$[(\text{dien})\text{Co}(\mu\text{-OH})_2(\mu\text{-CO}_3)\text{Co}(\text{dien})](\text{ClO}_4)_2$				
$\delta_m\mu^\theta$ (salt)	—	+1.2	+3.8	
$\delta_m\mu^\theta$ (ClO_4^-) ^a	—	+0.1	-0.1	
$\delta_m\mu^\theta$ (cation)	—	+1.0	+4.0	
$[(\text{H}_3\text{N})_4\text{Co}(\mu\text{-OH})(\mu\text{-NH}_2)\text{Co}(\text{CO}_3)_2]$				
$\delta_m\mu^\theta$ (complex)	—	+8.2	+15.8	+26.7
$[(\text{ox})_2\text{Co}\mu\text{-OH})_2\text{Co}(\text{ox})_2](\text{ClO}_4)_2$				
$\delta_m\mu^\theta$ (salt)	—	+1.2		
$\delta_m\mu^\theta$ (ClO_4^-) ^a	—	+0.1		
$\delta_m\mu^\theta$ (cation)	—	+26		

^a Taken from ref. [40].

Table 5.6 Transfer chemical potentials for the
binuclear Co(III) complexes in water–MeOH mixtures (kJ mol⁻¹; 298.2 K).

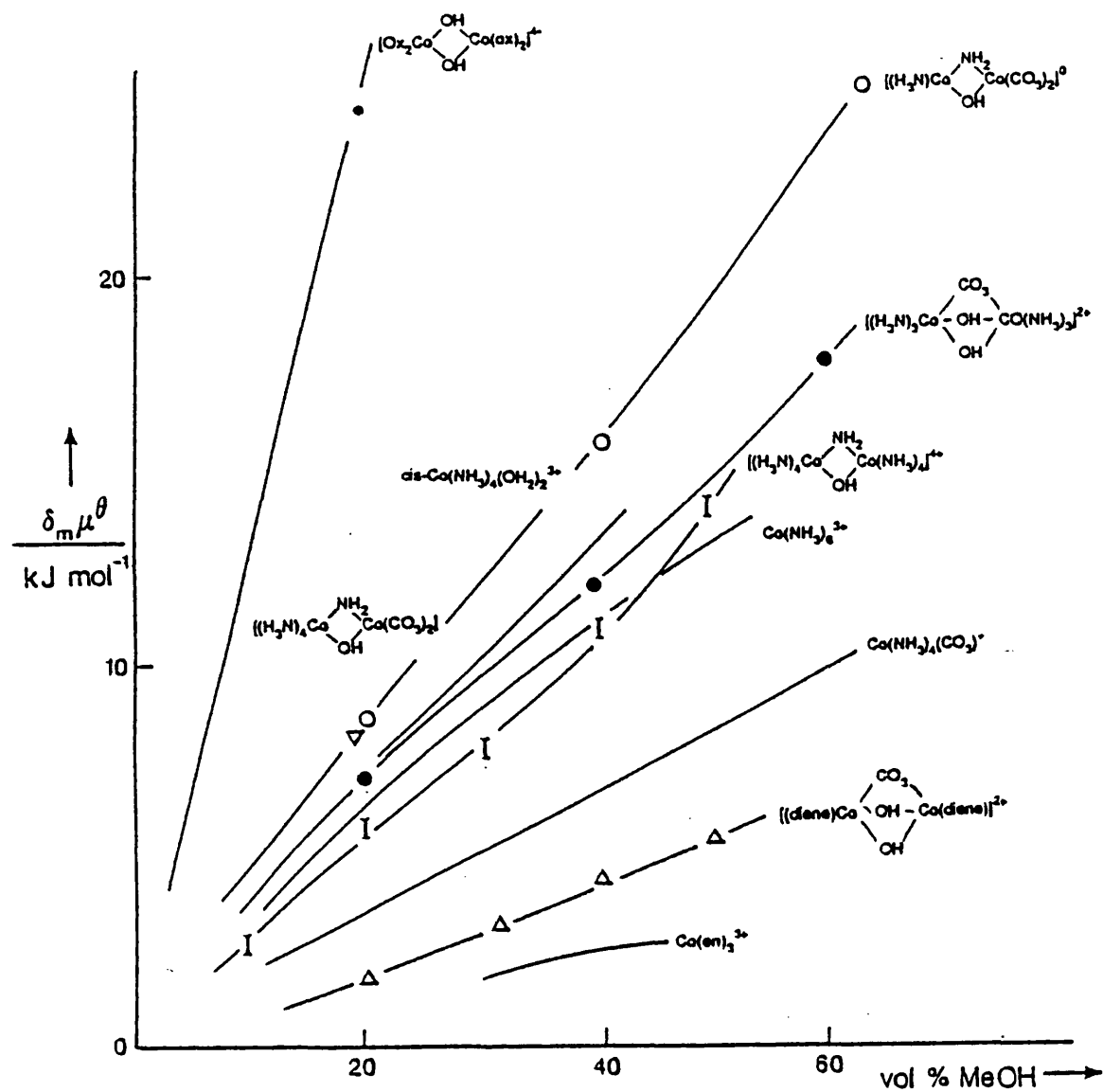


Figure 5.10 Transfer chemical potentials trends for the binuclear cobalt(II) complexes in water-methanol mixtures.

Chapter 6

Reactivity of Binuclear

Iron(II)-diimine Complexes

6.1 Introduction.

In the previous Chapter the extent of the metal–metal interaction was examined. The selective oxidation of one of these metal centres introduces the possibility of forming a mixed valence complex. Such structures have been particularly useful as models for inner–sphere electron transfer transition states.

The classification of binuclear mixed valence complexes was introduced in 1967 ^[158]. It divides them into three classes depending on the extent of electron delocalisation between the metal centres. Class I compounds are those in which there is essentially no delocalisation (the metals having discrete valences), with a prohibitively large barrier to electron transfer. Class III complexes are essentially fully delocalised, with the metal centres having equal (often fractional) formal oxidation states. The HOMO now incorporates both metal centres and bridging ligands, with the electron transfer being from a metal–ligand bonding to antibonding orbital. Only for Class II species is electron transfer meaningful, where the metal centres retain the properties of the discrete valence Class I species, but the much greater delocalisation is often accompanied by a metal to metal charge transfer (MMCT) band in the near-IR. It is from the shape and solvatochromism of this band that classification is often made ^[159].

Complex stability in solution has therefore become one of the main considerations in the design of potential mixed valence binuclear complexes. Consequently, ligand (and hence spin) constraints have meant that the vast majority of mixed valence complexes involve $\text{Ru}^{2+/3+}$ centres, although growing number of $\text{Fe}^{2+/3+}$ species are being reported ^[158,160]. In particular, the discovery that oxygen–bridged binuclear sites occur in many non-heme proteins and enzymes has led to a resurgence in models for such sites ^[161].

In this Chapter the reactivity of several binuclear iron(II) complexes is examined and compared with mononuclear analogues. On the basis of the results from this, preliminary redox studies are reported.

6.2 Experimental.

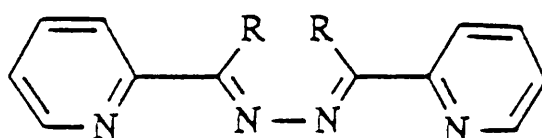
The binuclear cations $[\text{Fe}_2(\text{LL})_3]^{4+}$ (LL = paa, pmk, and pbk) were prepared as described in the previous Chapter. The required hydroxide and chloride solutions were prepared from the respective sodium salts (AnalaR).

The kinetics were measured at 298.2 K and, unless otherwise stated, at an ionic strength of 0.33 mol dm^{-3} (NaCl). The reaction was analysed from the decrease in absorbance of the iron(II)–diimine complex against time, and was followed for 2.5 half-lives. The concentration of hydroxide was much greater than that of the iron(II) complex. Good first-order kinetics were observed over the stated range with

$$-\frac{d[\text{complex}]}{dt} = k_{\text{obs}}[\text{complex}]$$

Observed first-order rate constants for the base hydrolysis of the $[\text{Fe}_2(\text{pbk})_3]^{4+}$ cation were obtained on a Hi-Tech Scientific stopped-flow machine (Model SF-3L) by C. D. Hubbard. All other kinetic measurements were obtained on either the HP 8451A or SP 1800 spectrophotometers described in Section 2.3.

Electrochemical measurements were conducted as described in Section 2.3.6.



R=H (paa)

R=Me (pmk)

R=Ph (pbk)

6.3 Results and Discussion.

6.3.1 Nucleophilic Attack.

The kinetics of base hydrolysis of, and nucleophilic attack, at iron(II)–diimine complexes have been extensively studied. Rates of hydrolysis of the parent diimine complexes $[\text{Fe}(\text{bipy})_3]^{2+}$ and $[\text{Fe}(\text{phen})_3]^{2+}$ ^[162] gave the familiar rate law with an ascending power series for the nucleophile concentration and a unimolecular aquation term (k_1)

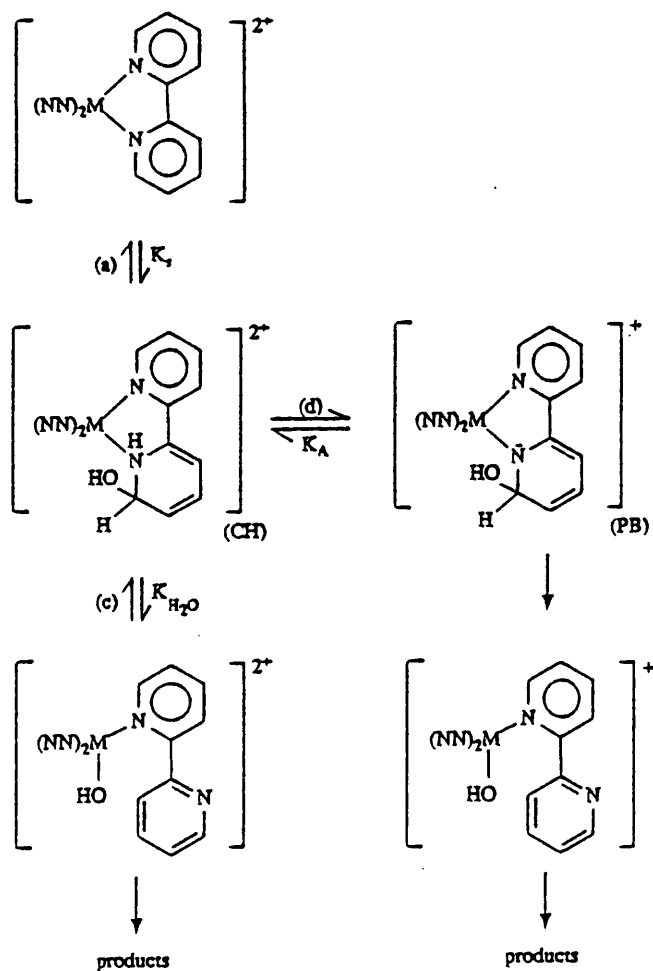
$$k_{obs} = k_1 + k_2[\text{Nu}^-] + k_3[\text{Nu}^-]^2 + k_4 [\text{Nu}^-]^3 + \dots$$

with k_3 and higher terms only being important at high nucleophile concentrations (or in some solvent mixtures). Subsequently, base hydrolysis reactivity of a large range of bis–diazadiimine ligand complexes (1–4) and several Schiff–base bidentate (5), tridentate (6), linear hexadentate (7), semicage (8) and finally fully encapsulated Schiff–base diimine complexes (9–10) have been reported (see Scheme 6.1 for ligand formulae). The rate constants for hydrolysis span over nine orders of magnitude for these complexes ^[112]. Even for the closely related bidentate complexes, (1–4), rate constants span 6 orders of magnitude ^[163].

Solvent modification of reactivity for many of these complexes has subsequently been analysed satisfactorily into initial– and transition–state contributions for a variety of binary aqueous solvent mixtures ^[41,164]. Kinetics in heterogeneous microemulsion systems have also been reported ^[165]. The presence of added cosolvents does not drastically alter the rate law (and presumably the mechanism) of nucleophilic attack for the majority of these complexes except that in organic cosolvent rich media k_3 and k_4 terms become more prominent. In contrast, microemulsions have been shown to alter the normal first–order

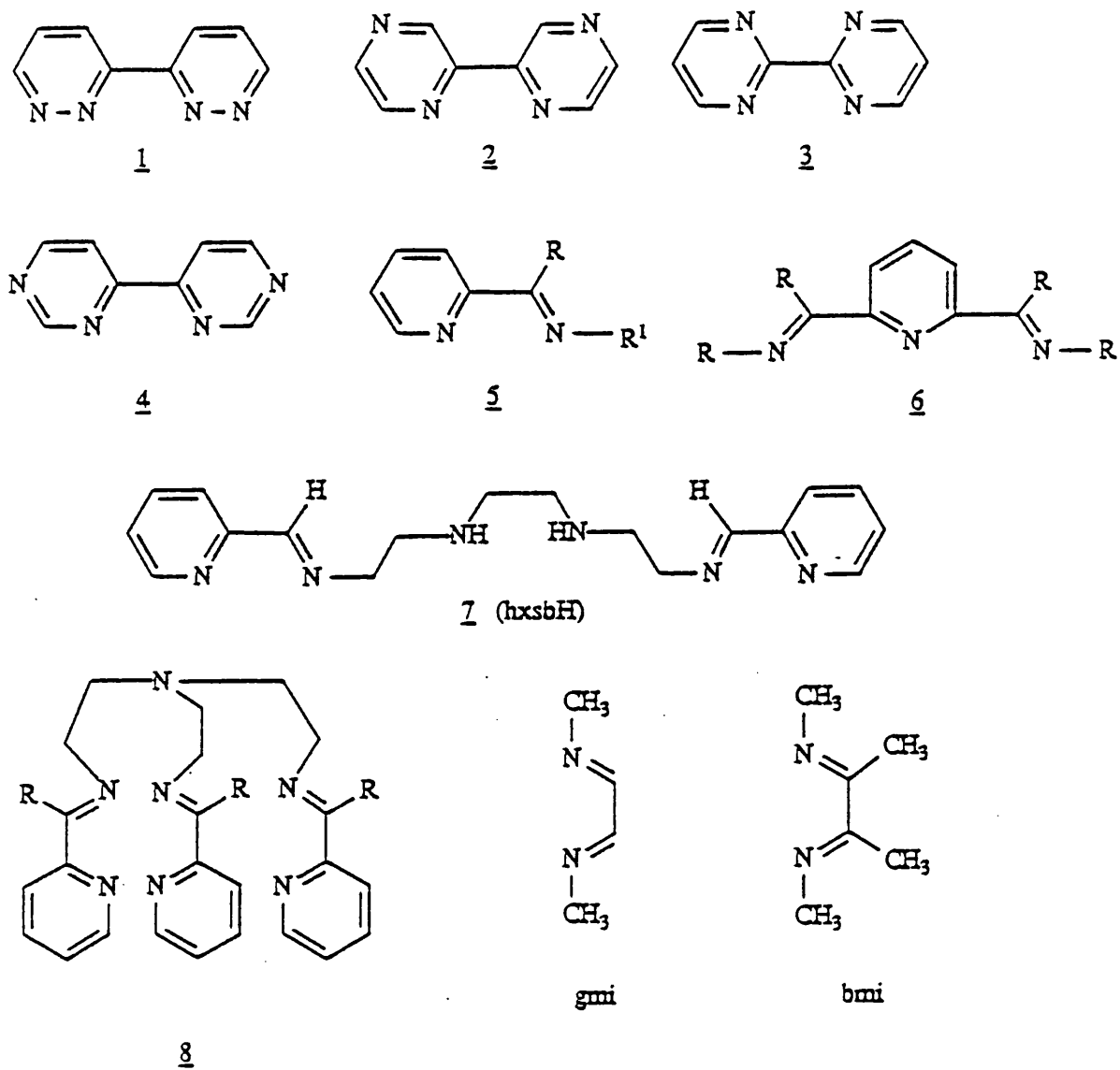
nucleophile dependence to zero-order for hydroxide attack at the hexadentate complex $[\text{Fe}(\text{hxsbH})]^{2+}$ [165].

The exact mechanism of nucleophilic attack remains one of some controversy [166], with initial nucleophilic attack either at the central metal atom [167], or at the ligand [168]. Early evidence in support of the latter route came predominantly from spectroscopic and kinetic experiments [169]. More recently, nmr experiments [170] and MO calculations [171] have been used to speculate as to the most likely site of attack (or deprotonation). The proposed reaction scheme for base hydrolysis of the $[\text{Fe}(\text{bipy})]^{2+}$ cation is illustrated below [168]

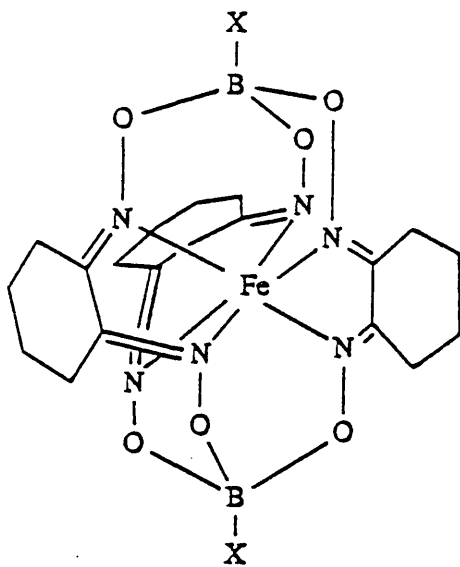


The initial equilibrium (K_S) involves the formation of a covalent hydrate (or solvate in protic media) by the addition of $H-OH$ ($R-OH$) across the $C=N$. It has been noted that this is very similar to the product of direct hydroxide attack at the ligand ^[172]. Subsequent addition of base involves deprotonation to form the pseudo base (PB). Intramolecular hydroxide transfer to the iron leads eventually to the products.

Although an identical mechanism for this ligand attack approach is unlikely for all of the various types of diimine ligands, the fast pre-equilibrium between the complex and some sort of ligand substituted intermediate remains central. Persuasive but not incontrovertible evidence has been reported which favours such intermediates, although as yet, only for highly activated ring systems, such as those illustrated (11–12), has the equilibrium constant been of sufficient magnitude for any intermediates to be seen spectroscopically ^[169].

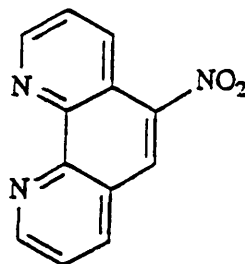


Scheme 6.1 General ligand formulae.

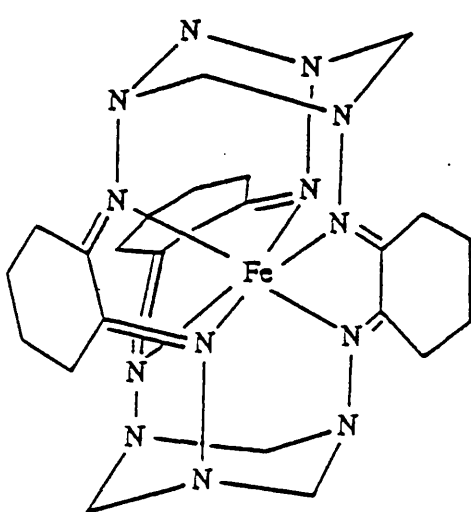


Bcx cage

9



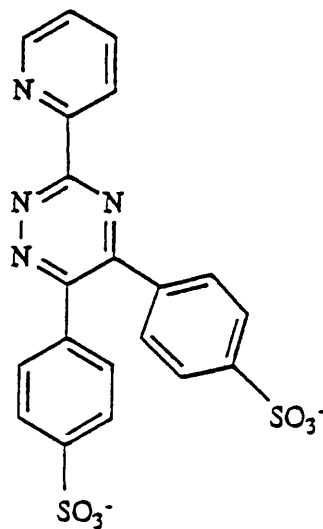
11



C₃N₃ cx cage

10

2+



12

Scheme 6.1 (cont.) General ligand formulae.

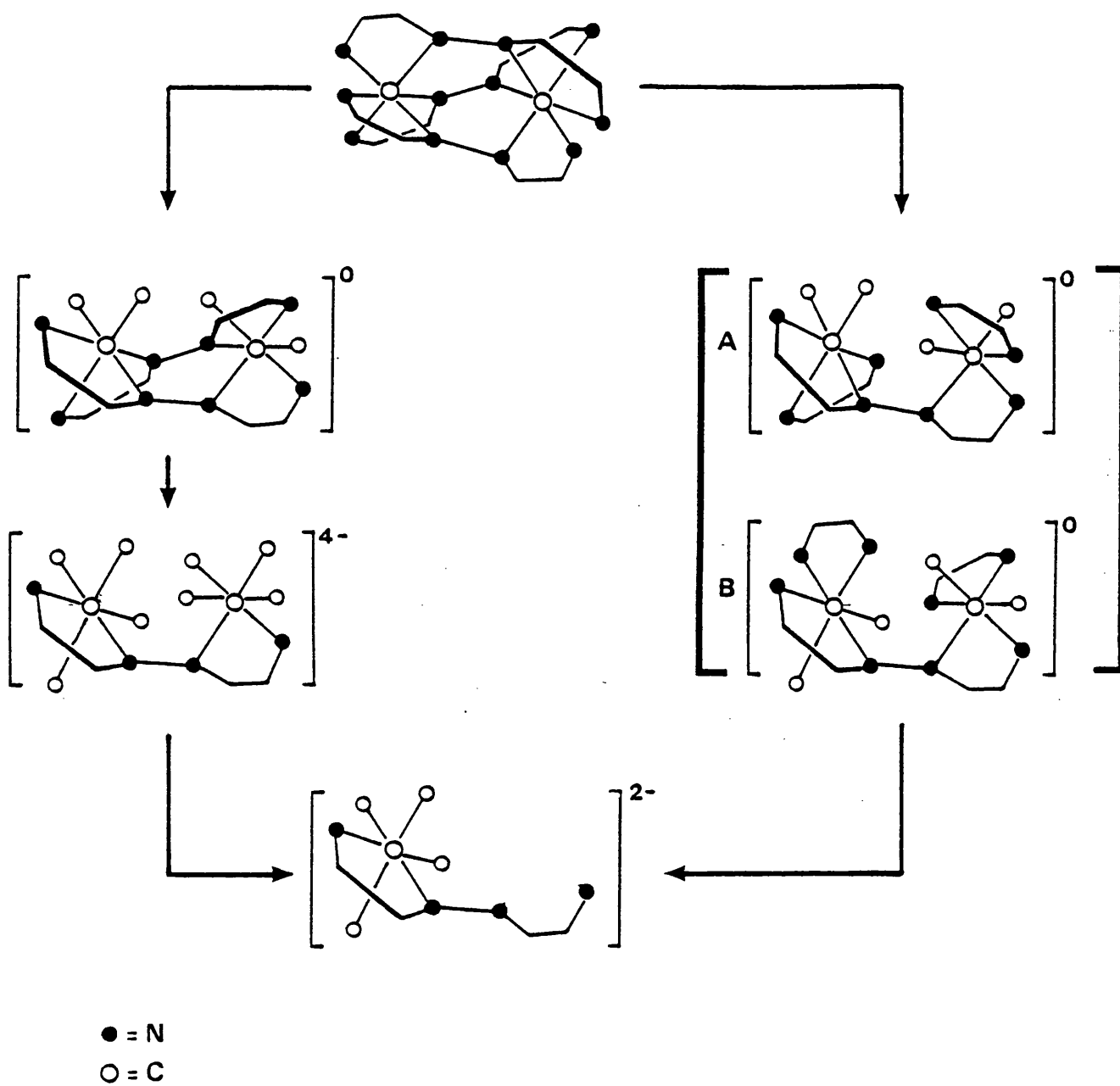
Cyanide attack.

The reaction of $[\text{Fe}_2(\text{pmk})_3]^{4+}$ with cyanide should theoretically lead to the formation of binuclear ternary iron–cyanide–diimine complexes in an analogous manner to the preparations undertaken in Chapter 3. After reaction, definitive product assignment was not possible because of the very complicated product distribution. Modifications to Schilt's method ^[88] were unsuccessful in cleanly separating bis- and tetra-cyano complexes. Partial product separation was achieved by eluting the reaction mixture on an alumina column, firstly with dichloromethane and finally methanol – leaving excess KCN on the column. The MeOH and CH_2Cl_2 fractions were rotary evaporated to dryness and analysed. The UV/visible spectra, solvatochromic shifts and TLC traces all appeared to indicate single products for both fractions, but ^1H and ^{13}C NMR spectra were incompatible with any proposed products – possibly due to the incorporation of cyanide nucleophiles into the organic ligand framework. Further purification of the methanol fraction was achieved by eluting a concentrated aqueous solution down an anion exchange column (DEAE Sephadex) initially with water and finally with aqueous KI (0.1 mol dm^{-3}). From their relative mobilities it appeared that the fractions contained anions of 2- and 4- charge respectively, although again, structures remained unresolved because of incompatible NMR data.

Scheme 6.2 shows several intermediates that are possible from the reaction of cyanide with the $[\text{Fe}_2(\text{pmk})_3]^{4+}$ cation. After substitution of one diimine moiety by 2 CN^- nucleophiles at one end of the binuclear complex, additional nucleophilic attack can occur at 3 distinct sites. If substitution occurs at the other end of the diimine ligand then a di-bridged binuclear complex results.

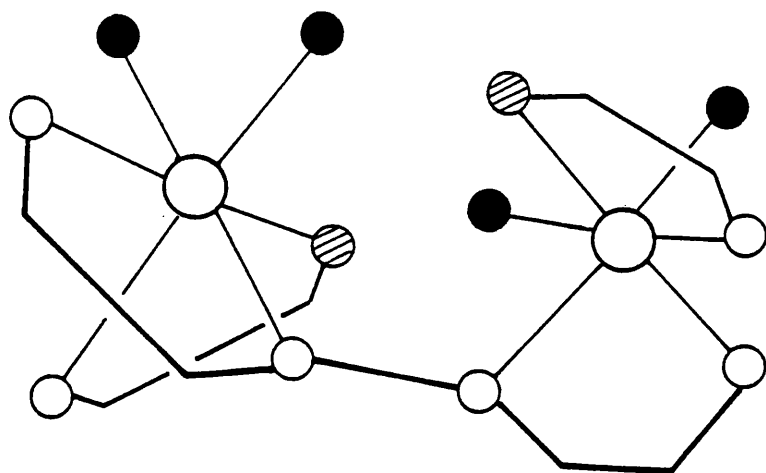
Attack can also occur at the 2 other diimine units leading to 2 mono-bridged geometric isomers with a pendant arm bonded to each iron centre. Each metal centre in the respective isomer has the same configuration; both are shown in Scheme 6.3.

The problem of product assignment is much easier for base hydrolysis of these low-spin iron(II)-diimine complexes, with the iron(II)-hydroxide being oxidised by dissolved oxygen to give ultimately $\text{Fe}_2\text{O}_3 \cdot n\text{H}_2\text{O}$. The kinetics of base hydrolysis for several of these binuclear complexes follows.

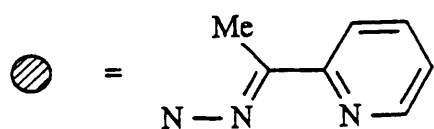
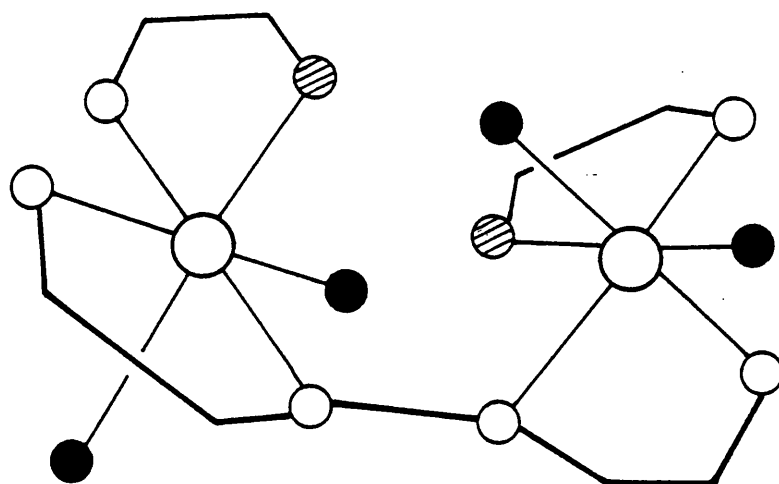


Scheme 6.2 Reaction scheme of possible products for the reaction between the $[\text{Fe}_2(\text{pmk})_3]^{4+}$ cation and cyanide.

A



B



Scheme 6.3 Diagram showing the di-bridged isomers following cyanide attack.

Base Hydrolysis.

The hydrolysis of the $[\text{Fe}_2(\text{pmk})_3]^{4+}$ and $[\text{Fe}_2(\text{pbk})_3]^{4+}$ cations both occur in two stages. For the latter complex, it was possible to merge these two processes into a single exponential by altering the hydroxide concentration. For the former, the rates of these two processes are so different that both can be measured with some confidence. The reaction involves the fast conversion to an intermediate followed by slow decomposition to the products. The latter step is taken as the observed first-order rate constant which is given in Table 6.1. Estimated second-order rate constants are also included in this Table. Figure 6.1 puts these estimated second-order rate constants into perspective with existing data on mononuclear iron(II)–diimine complexes.

Altering the R-group from Me to H to Ph results in rate constants dramatically changing by a factor of ca. 10^6 . Such a substituent effect on rate constants is considerably larger than for the other structures given in Figure 6.1. Presumably steric effects here must be more important than for mononuclear analogues because of the geometrical constraints imposed by the binuclear nature of the cations.

Complex ^a	$[\text{OH}^-] / \text{mol dm}^{-3}$	k_{obs} / s^{-1}	$k_2 / \text{mol}^{-1} \text{dm}^3 \text{s}^{-1}$	$\text{Log}_{10}(k_2)$
$[\text{Fe}_2(\text{paa})_3]^{4+}$	0.02	5.0×10^{-4}	2.5×10^{-2}	-1.6
$[\text{Fe}_2(\text{pmk})_3]^{4+}$	0.08	2.0×10^{-5}	2.5×10^{-4}	-3.6
$[\text{Fe}_2(\text{pbk})_3]^{4+}$	0.02	2.4	120	2.1

^a Ligand formulae defined in text.

Table 6.1 Observed first-order, and estimated second-order rate constants
for the base hydrolysis of binuclear iron(II) cations (298.2 K).

The spectroscopic changes that take place when hydroxide is added to a solution of $[\text{Fe}_2(\text{pmk})_3]^{4+}$ are shown in Figure 6.2. On addition, complete conversion to an intermediate occurs ($k_{\text{obs}} = \text{ca. } 3 \times 10^2 \text{ s}^{-1}$; $[\text{OH}^-] = 0.01 \text{ mol dm}^{-3}$) with corresponding changes in λ_{max} from 506 nm ($\epsilon = 1.5 \times 10^4$) to 520 nm ($\epsilon = 1.2 \times 10^4$). This conversion exhibits pH reversibility, reconversion to $[\text{Fe}_2(\text{pmk})_3]^{4+}$ is achieved on addition of acid.

With a +4 charge it is likely that ion-pairing with anions will occur in solution. No spectroscopic changes are observed on addition of concentrated (1.0 mol dm^{-3}) solutions of anions ($\text{X} = \text{Cl}^-$, F^- and SO_4^{2-}) however. Therefore, the observed changes in the UV/visible spectrum are not due to ion-pairing. Instead, they must be due to an intermediate formed by the direct interaction of the hydroxide ion with the complex. Whether this process involves nucleophilic attack at the ligand (as shown above), or ligand deprotonation is unclear. Certainly, there are no acidic C—H protons, or electrophilic carbon atoms obvious from the ^1H and ^{13}C spectra reported in the previous Chapter.

The rate constant for the formation of this intermediate is such that ligand deprotonation most likely, with the hydroxide acting as a base rather than a nucleophile. In either case, the +4 charge will electrostatically favour such a pre-equilibrium, and could consequently lead to a high intermediate concentration. Additionally, it would appear from the UV/visible spectrum that, irrespective of the exact nature of the interaction, both iron centres are affected equally by the addition of OH^- . This must be the result of either a symmetrical interaction at each end of the complex or, less likely, incorporation of OH^- into the inter-metal cavity.

The $[\text{Fe}_2(\text{pmk})_3]^{4+}$ cation is extremely stable in water at pH 7. Solvolysis of this cation occurs in binary aqueous solvents containing protic media (i.e.

alcohol–water mixtures) to give a stable iron(II) complex with significantly different λ_{max} and ϵ values. The rate constants for these solvolysis reactions is dependent on the cosolvent present, but typically, almost complete conversion occurs in ca. 120 minutes. The spectroscopic properties (ϵ and λ_{max}) also depend on the nature of the cosolvent used. Solvolysis leads to a product with a smaller λ_{max} and a larger extinction coefficient; values for MeOH and Bu^tOH are 481 and 476 nm. Consistent values for the extinction coefficients were unobtainable, but are around 10% larger than for the $[\text{Fe}_2(\text{pmk})_3]^{4+}$ cation. On prolonged standing, solid samples reconverted back to the $[\text{Fe}_2(\text{pmk})_3]^{4+}$ cation. The rate of this reversion varied slightly with temperature and with pressure (i.e. in a dessicator).

Samples of these solvolysis products were isolated as their PF_6^- salts. Satisfactory elemental analysis of these salts could not be achieved. Dissolution in water did not lead to the reversion to the $[\text{Fe}_2(\text{pmk})_3]^{4+}$ cation. Instead, both solutions are stable for several days at pH 7. Base hydrolysis of the MeOH and Bu^tOH solvolysed samples is first-order. First-order rate constants ($[\text{OH}^-] = 0.1 \text{ mol dm}^{-3}$) are $1.4 \times 10^{-3} \text{ s}^{-1}$ and $5.2 \times 10^{-3} \text{ s}^{-1}$ respectively. No significant spectroscopic changes are seen during the reaction except for the absorbance decrease normally associated with reactions of this type.

The above description of the reactivity of the binuclear pmk cation is therefore consistent with many of the ideas proposed by Gillard *viz.* covalent hydrates and pseudo bases, and is clearly an area which warrants further investigation.

Complicated rate laws can arise from the existence of intermediates of reduced coordination having significant lifetimes. In particular, intermediates in which one iron–nitrogen bond is ruptured, so that the ligand is still bound to the iron via a bidentate chelating unit, may be sufficiently stable to give consec-

utive kinetics. The acid hydrolysis of $[\text{Fe}(\text{bipy})_3]^{2+}$ ^[174] exhibits such biphasic kinetics. Here, after the initial conversion to the intermediate good first-order kinetics are observed for 3 half-lives, without the evidence to suggest further intermediates. Decomposition of both iron(II)-diimine units therefore occurs in a single stage.

Mean observed first-order rate constants (Table 6.2) calculated from the decay of spectrum B are reported as functions of hydroxide concentration and solvent composition in Table 6.2. These observed first-order rate constants are shown in Figure 6.3 . As can be seen from this Figure, the data can only be accommodated with the inclusion of k_3 and possibly higher terms. Even in water, the kinetics deviate to a small, but nevertheless significant, degree from a linear dependence.

Figure 6.1 puts these estimated second-order rate constants into perspective with existing data on mononuclear iron(II)-diimine complexes.

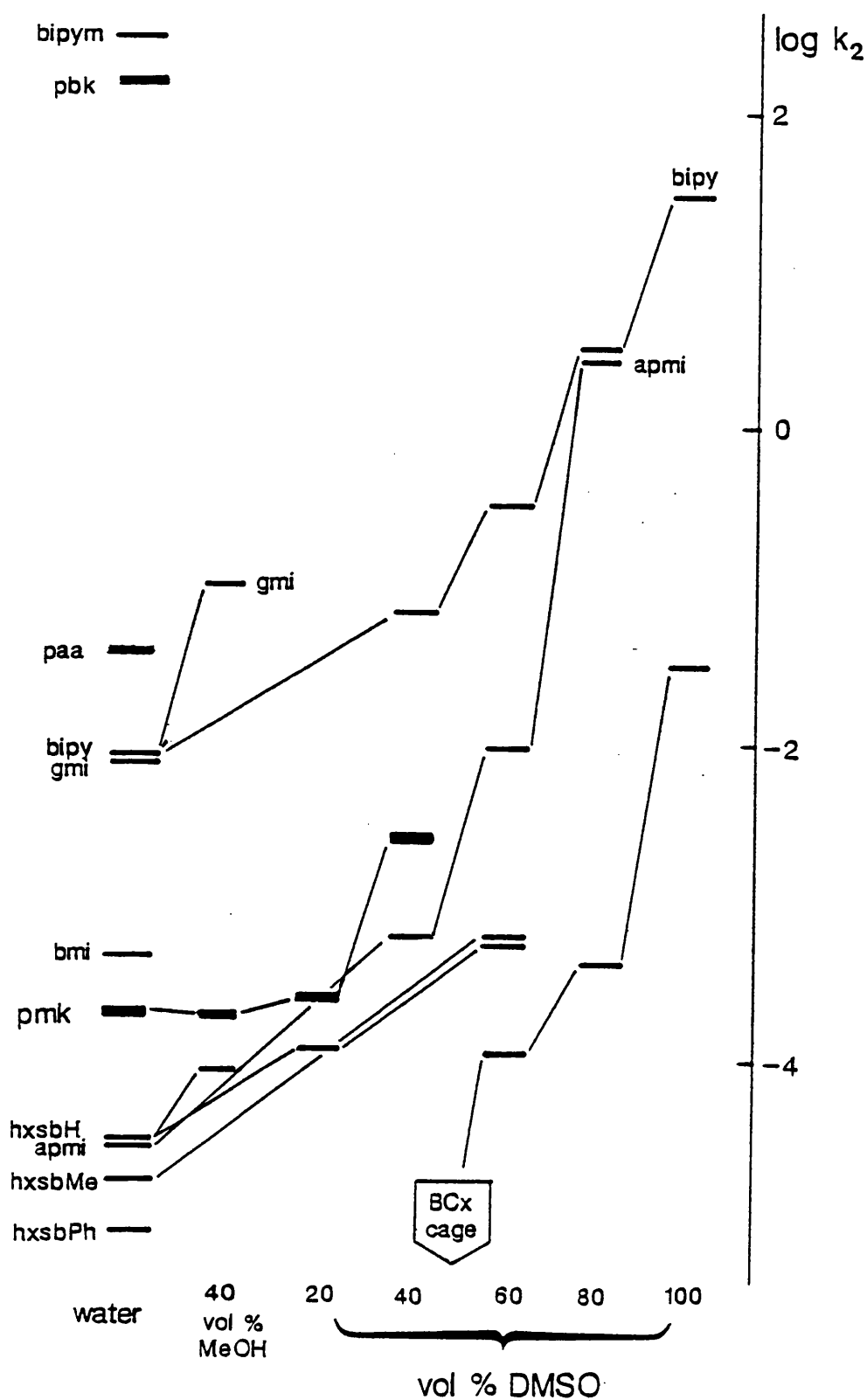


Figure 6.1 Comparisons of rate constants for base hydrolysis for iron(II)-diimine complexes.

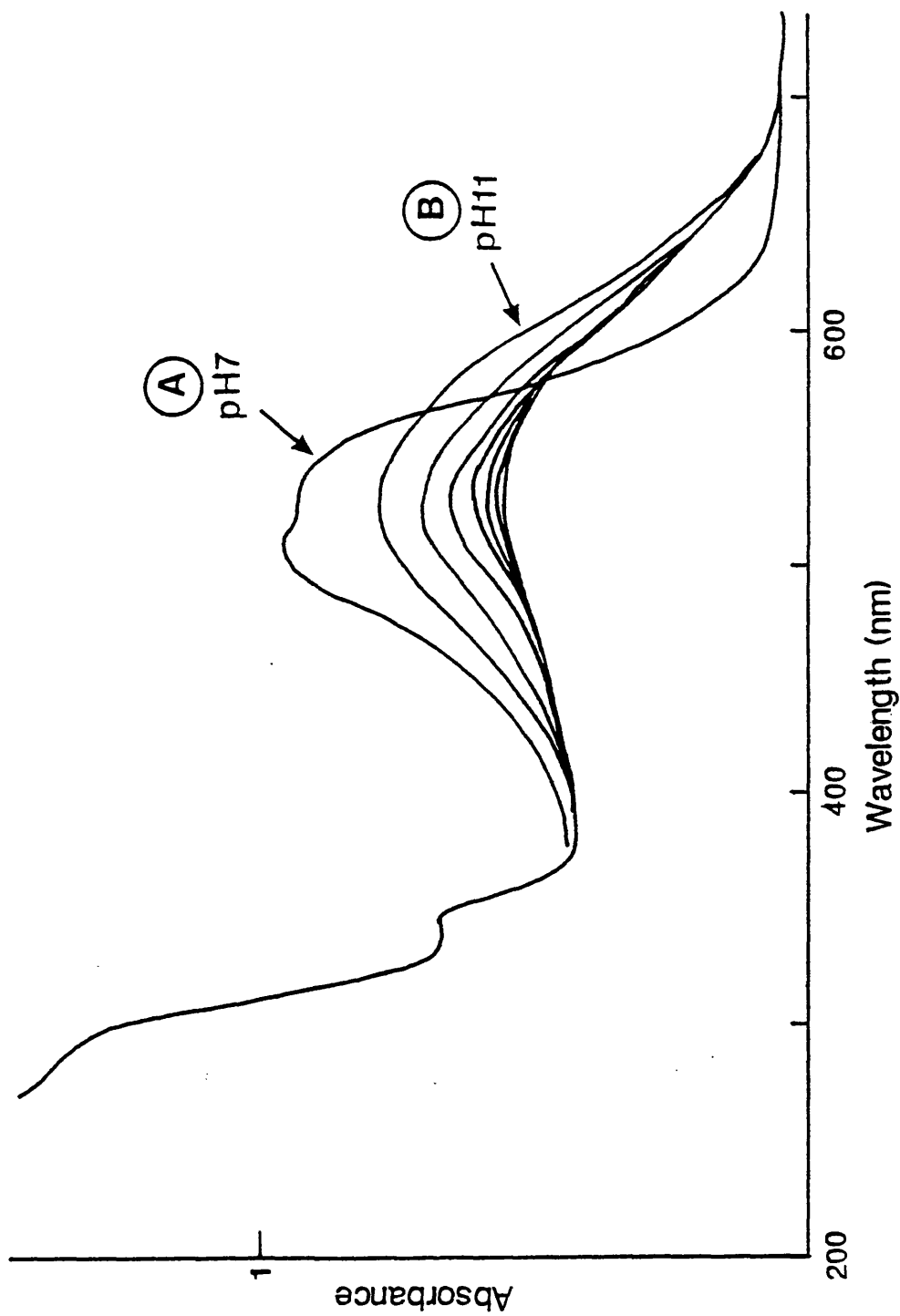


Figure 6.2 Spectroscopic changes accompanying addition of base
to the $[\text{Fe}_2(\text{pmk})_3]^{4+}$ cation.

$10^5 k_{obs} / s^{-1}$											
Solvent	$[OH^-] / mol\ dm^{-3}$										
	0.01	0.02	0.04	0.05	0.06	0.08	0.10	0.15	0.20	0.26	0.33
water						2.0	3.2	4.0	5.3	7.3	
40% MeOH				1.0			1.5	2.2	2.8	3.7	5.3
20% Pr ⁱ OH				3.2	4.2	4.6	5.6	10.9	16.1		
40% Pr ⁱ OH	6.5						14	26			
20% DMSO					4.7		4.7	5.4	5.8	16	21
40% DMSO		30	34		39	47	54	82	113		

Table 6.2 Observed first-order rate constants for the base hydrolysis of the $[Fe_2(pm_k)_3]^{4+}$ cation in binary aqueous solvent mixtures.

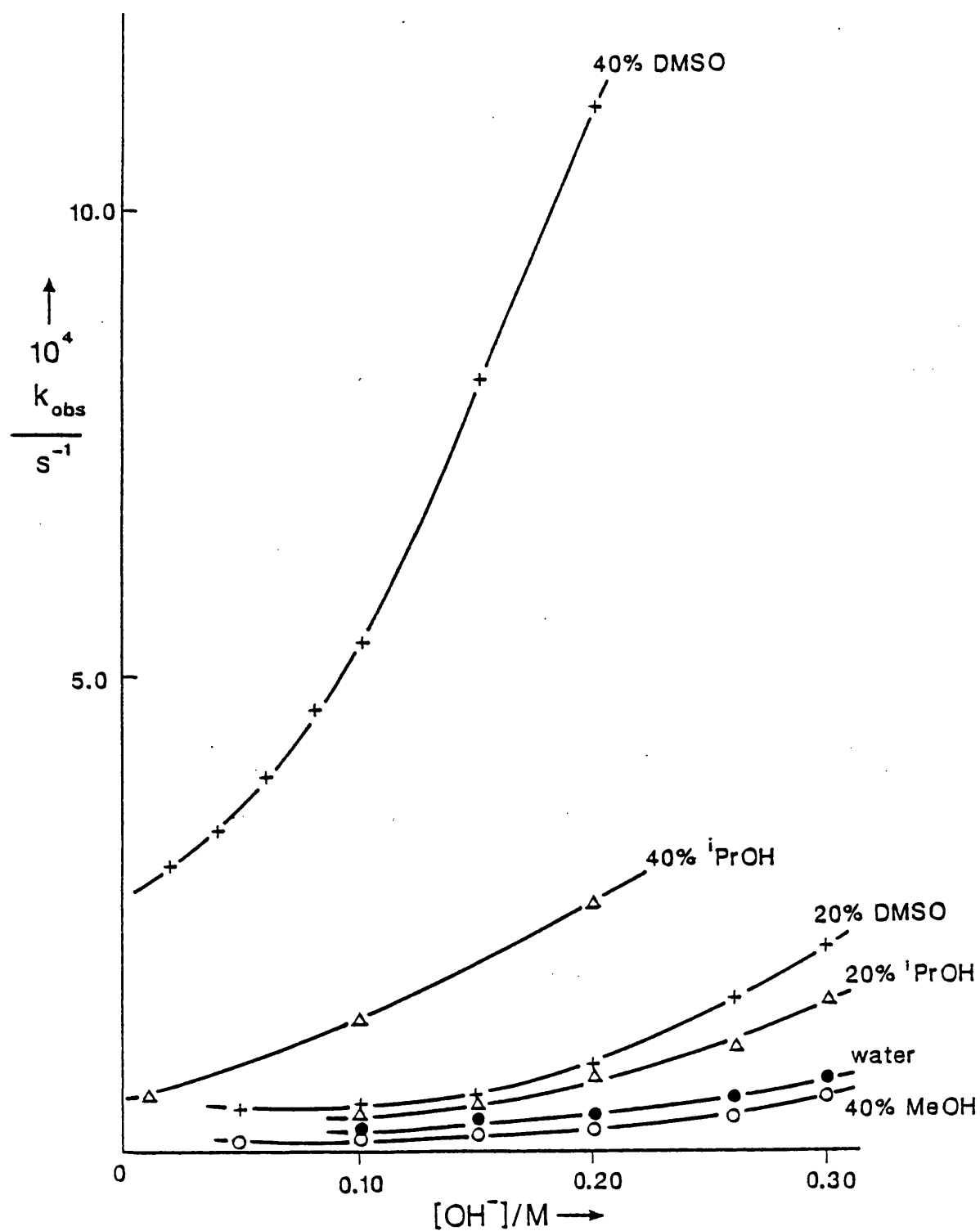


Figure 6.3 Observed first-order rate constant trends for the base hydrolysis of the $[\text{Fe}_2(\text{pmk})_3]^{4+}$ cation in binary aqueous solvent mixtures.

Interpretation of these rate constants is clouded by the complexity introduced because of the coupled pre-equilibrium and subsequent reaction. Certainly, the k_1 term is no longer a true reflection of the solvolysis of the $[\text{Fe}_2(\text{pmk})_3]^{4+}$ cation.

Solvent acceleration of the base hydrolysis is, as expected, in line with the increased chemical potential of the hydroxide ion in various binary aqueous mixtures. Such increases in chemical potential reflect a decrease in solvation of the highly hydrated hydroxide ion, and hence an increase in its effective nucleophilicity. Estimated k_2 values in binary aqueous mixtures are shown in Figure 6.1.

The slight discrepancy between observed first-order rate constants in water and 40% MeOH are due to the competing solvolysis of the complex (see above). For the latter solvent mixture the rate constant for base hydrolysis is of a similar magnitude to that of solvolysis. The base hydrolysis rate enhancement afforded by the other solvent mixtures is such that the two processes are kinetically distinct, with the rate of base hydrolysis being the fastest route.

6.3.2 Redox Behaviour.

The preceeding section has established the stability of the $[\text{Fe}_2(\text{LL})_3]^{4+}$ ($\text{LL} = \text{paa}, \text{pmk}, \text{pbk}$) cations in aqueous solution. The only suitable candidate for a mixed valence complex, using the stability of each complex in aqueous-containing media as the prime criterion, is that derived from the pmk ligand. The redox behavior of this cation is therefore analysed below by 'wet' and electrochemical techniques.

Complete oxidation of the $[\text{Fe}_2(\text{pmk})_3]^{4+}$ cation needed 12 equivalents of the $\text{Ce(IV)}/\text{H}_2\text{SO}_4$ oxidant. No clear metal-centred oxidation process was observed.

This most probably involved the oxidation of the —CH_3 groups to $\text{—CH}_2\text{OH}$ in analogy with that observed for several mononuclear complexes ^[138].

Oxidation with either 1 or 2 equivalents of $\text{S}_2\text{O}_8^{2-}$ was extremely slow ($k_{\text{obs}} = \text{ca. } 10^{-7} \text{ s}^{-1}$, with $[\text{S}_2\text{O}_8]^{2-} = 1 \times 10^{-4} \text{ mol dm}^{-3}$). In contrast to Ce(IV) the repeat scan UV/visible spectrum showed metal-centred oxidation, but the rate of oxidation was too slow to distinguish with any great certainty between oxidation and solvolysis pathways.

Electrochemistry.

Electrochemistry in non-aqueous solvents has proved to be a far more effective method with which to achieve metal oxidation of mononuclear iron(II)–diimine complexes ^[175] without complications from ligand-centred processes.

The cyclic voltammograms of the ligands (1–3) are shown in Figure 6.4. Clearly, no analogous ligand oxidation to that observed above occurs here. An irreversible reduction does occur however for all three ligands between approximately 1.3 to 1.6 V. Upon coordination to the redox-inactive Zn^{2+} cation, further redox processes occur as shown in Figure 6.5(b). Here, 2 irreversible reductions take place at approximately -1.5 V . These, and the oxidations noted above most probably correspond to the addition or removal of electrons from the pyridine π electron system. Figure 6.5(b) shows the cyclic voltammogram of the $[\text{Co}_2(\text{pmk})_3]^{4+}$ cation, which again has several irreversible reductions between -1.0 and -1.5 V . In addition, two irreversible reductions at ca. -0.7 V and a quasi-reversible oxidation at ca. $+0.5 \text{ V}$ also occur. The latter feature is most probably associated with the $\text{Co}^{2+} \rightleftharpoons \text{Co}^{3+}$ redox couple, with no indication of a stable mixed valence species.

Cyclic voltammograms of the binuclear $[\text{Fe}_2(\text{pmk})_3]^{4+}$ cation are shown in

Figure 6.6 as a function of the scan rate. From this Figure it can be seen that there is no clear indication of a mixed valence cation, although one can presume that the waves at positive potential are associated with metal oxidation. More interestingly, several reductive processes occur between -0.5 and -1.4 V. The stability of the reduction products is seen as a function of the scan rate, with two distinct waves at low scan rates merging into a single wave as the scan rate increases. Products from such a reduction are extremely difficult to identify at this stage and could involve ligand radicals or even possibly iron(I) metal centres.

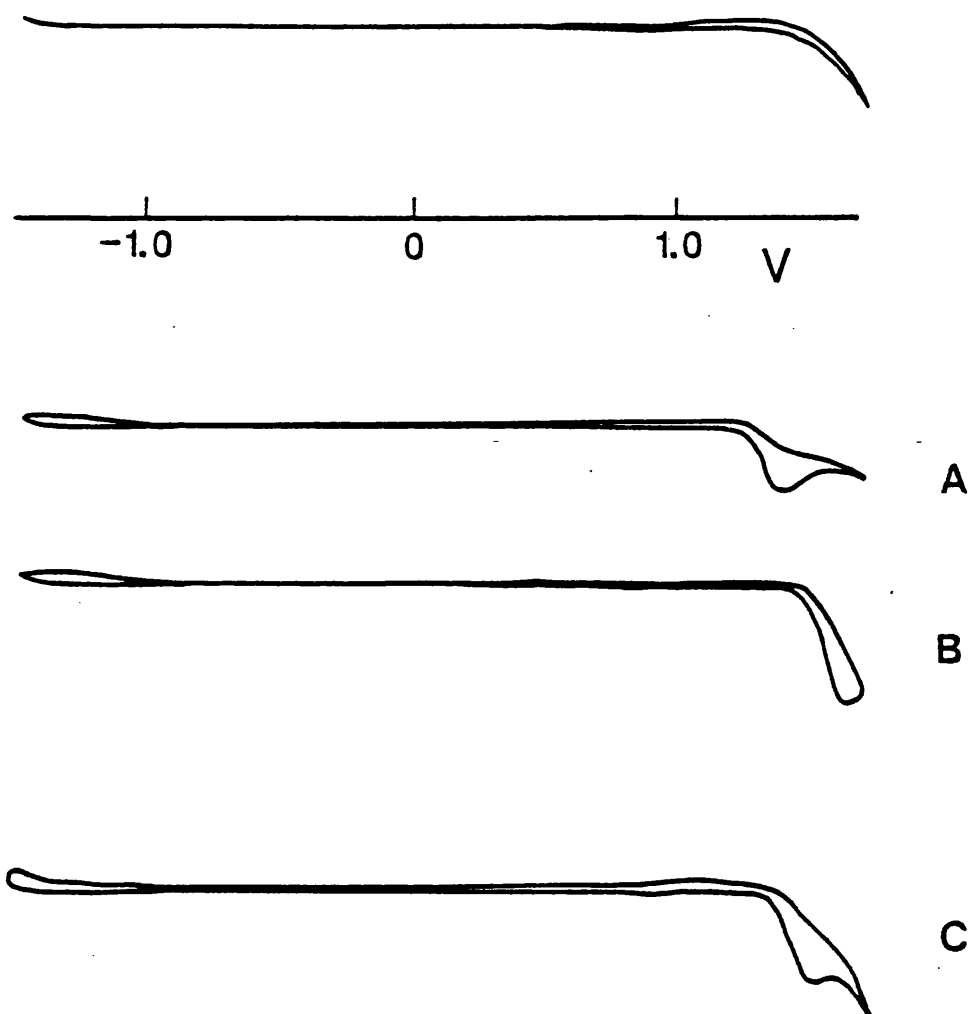


Figure 6.4 Cyclic voltammogram for the terdentate ligands; (a) paa (b) pmk (c) pbk.

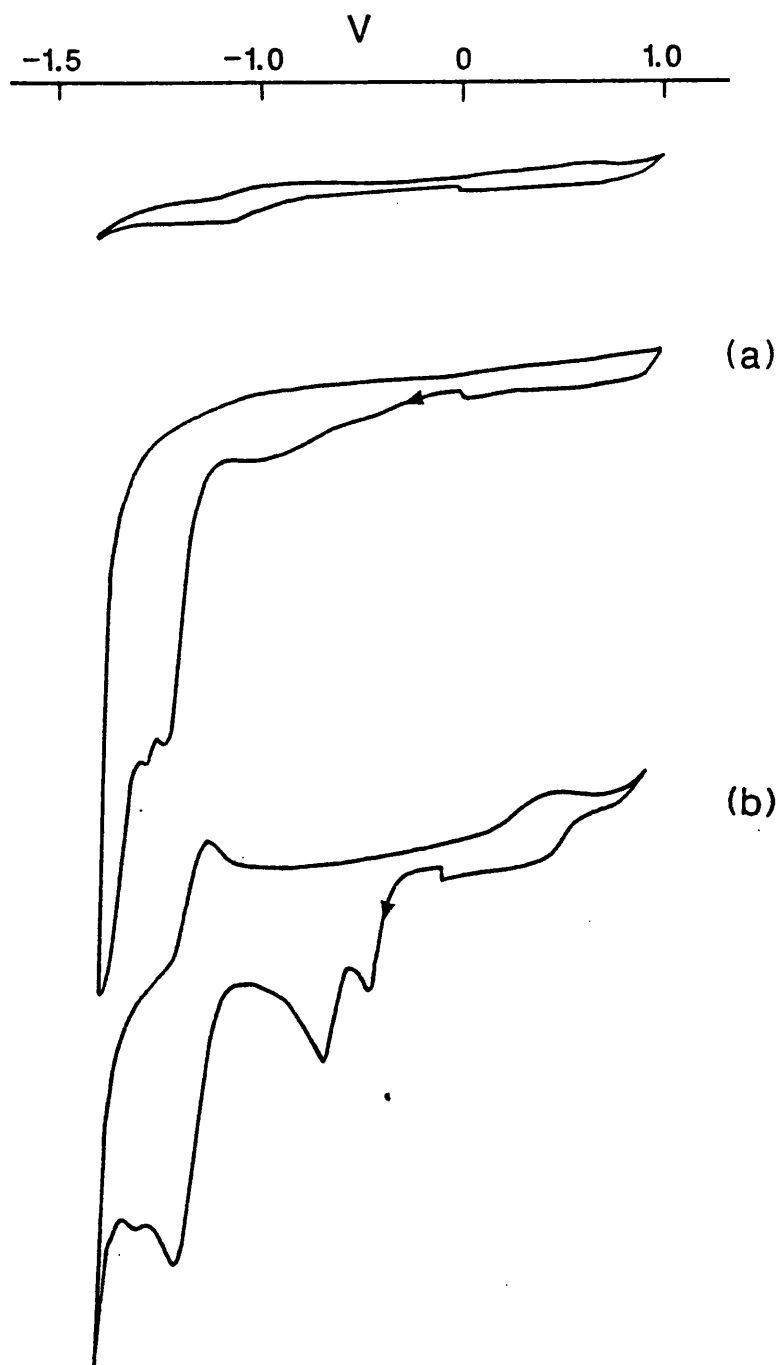


Figure 6.5 Cyclic voltammograms for the $[\text{M}_2(\text{LL})_3]^{4+}$
cations; $\text{M} = \text{(a)} : \text{Zn}^{2+}$, $\text{(b)} : \text{Co}^{3+}$.

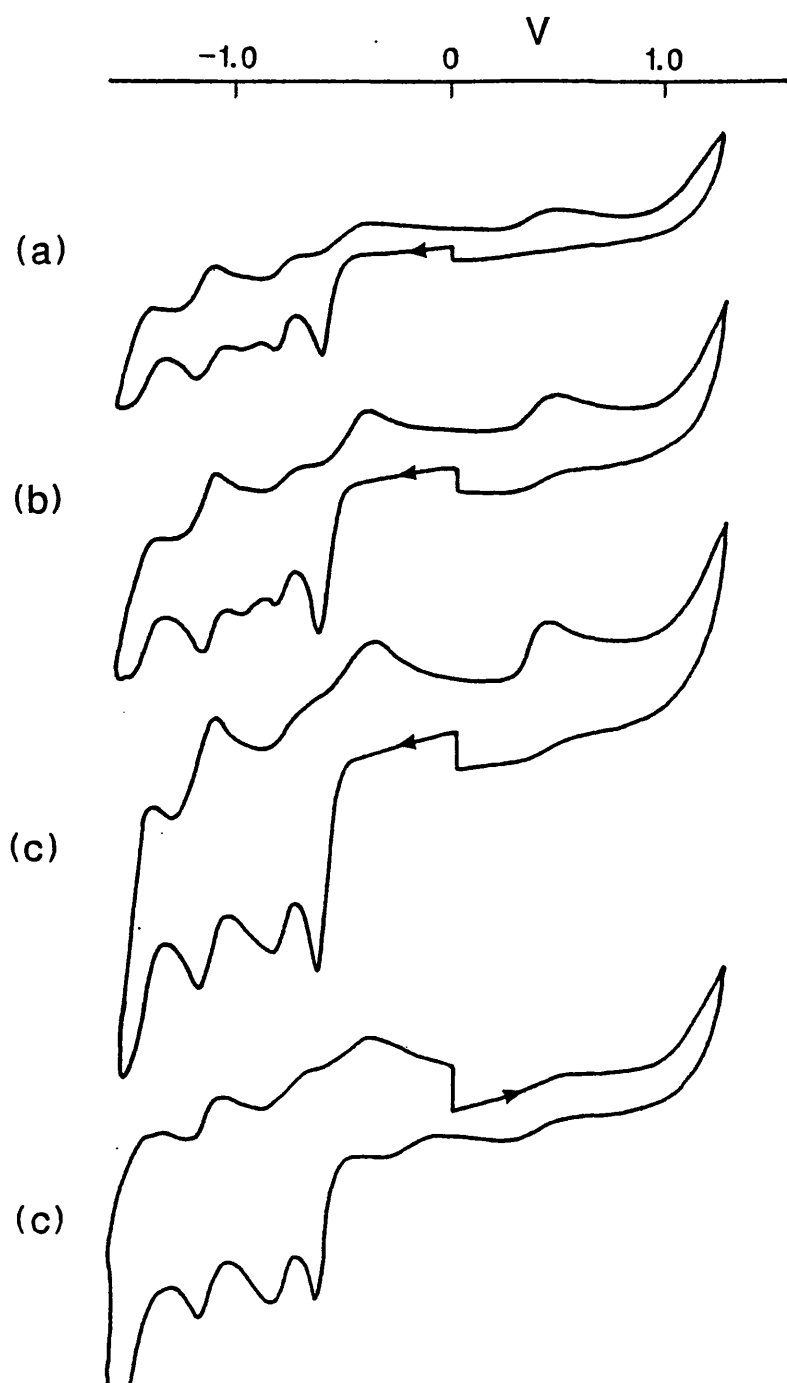


Figure 6.6 Cyclic voltammograms for the $[\text{Fe}_2(\text{pmk})_3]^{4+}$ cation;
scan rate = ; (a) 50 mV s^{-1} , (b) 100 mV s^{-1} , (c) 200 mV s^{-1} .

References

References.

1. H. Eyring and F. Daniels, *J.Am.Chem.Soc.*, 52, 1473 (1930).
2. F. Daniels and E. H. Johnston, *J.Am.Chem.Soc.*, 43, 53 (1921); R. H. Lueck
J.Am.Chem.Soc., 44, 757 (1922).
3. J. R. Eyler and D. E. Richardson, *J.Am.Chem.Soc.*, 107, 6130 (1985).
4. G. E. McManis, R. M. Nielson, A. Gochev, and M. J. Weaver,
J.Am.Chem.Soc., 111, 5533 (1989).
5. N. Menshutkin, *Z.Phys.Chem.*, 6, 41 (1890).
6. C. K. Ingold, "*Structure and Mechanism in Organic Chemistry*", Cornell
University Press, Ithaca, New York see p. 458-9.
7. P. Sykes, "*A Guidebook to Mechanism in Organic Chemistry*", 4th.edn.,
Longman, Harlow (1975), p. 193.
8. J. I. Zink and M. J. Incorvia, *J.Chem.Soc., Chem.Comm.*, 730 (1977).
9. D. R. Prasad and G. Ferraudi, *Inorg.Chem.*, 21, 4241 (1982).
10. J. M. Fukuto, D. A. Newman, and F. R. Jensen, *Organometallics*, 6 , 415
(1987).
11. E. Grunwald and S. Winstein, *J.Am.Chem.Soc.*, 70, 846 (1948); A. H.
Fainberg and S. Winstein, *J.Am.Chem.Soc.*, 78, 2770 (1956).
12. H. G. Grimm, H. Ruf, and H. Wolff, *Z.Phys.Chem.*, B13, 301 (1931).
13. M. Gielen and J. Nasielski, *J.Organomet.Chem.*, 1 , 173 (1963).

14. W. Belluco, A. Orio, and M. Martelli, *Inorg.Chem.*, 5, 1370 (1966).
15. J. J. Savage and R. H. Wood, *J.Soln.Chem.*, 5, 733 (1976).
16. W. Blokzijl, J. Jager, J. B. F. N. Engberts, and M. J. Blandamer,
J.Am.Chem.Soc., 108, 6411 (1986).
17. J. G. Kirkwood and F. P. Buff, *J.Phys.Chem.*, 13, 774 (1951).
18. A. Ben-Naim, *Cell Biophys.*, 12 , 255 (1988).
19. R. van Eldik in “*Inorganic High Pressure Chemistry*” , ed. R. van Eldik,
Elsevier, Amsterdam (1986) see chapter 1.
20. C. D. Hubbard, *personal communication*.
21. M. A. Bergkamp, J. Brannon, D. Madge, R. J. Watts, and P. C. Ford
J.Am.Chem.Soc., 101, 4549 (1979).
22. M. A. Bergkamp, R. J. Watts, and P. C. Ford *J.Am.Chem.Soc.*, 102, 2627
(1980).
23. C. Moralego and C. H. Langford, *Inorg.Chem.*, 30, 567 1991.
24. J. Burgess, *Spectrochim.Acta*, 45A, 159 (1989).
25. J. P. Chang, E. Y. Fung, and J. C. Curtis, *Inorg.Chem.*, 25, 4233 (1986); J. T.
Hupp, G. A. Neyhart, and T. J. Meyer, *J.Am.Chem.Soc.*, 108, 5349 (1986).
26. U. Sinha, M. D. Lowery, W. S. Lowery, W. S. Hammack, D. N. Hendrickson,
and H. G. Drickamer, *J.Am.Chem.Soc.*, 109, 7340 (1987).
27. T. -Y. Dong, D. N. Hendrickson, C. G. Pierpoint, and M. F. Moore,
J.Am.Chem.Soc., 108, 963 (1986).

28. W. S. Hammack, H. G. Drickamer, M. D. Lowery, and D. N. Hendrickson, *Chem. Phys. Lett.*, **132**, 231 (1986); *Inorg. Chem.*, **27**, 1307 (1988).
29. S. M. Oh, D. N. Hendrickson, K. L. Hassett, and R. E. Davis, *J. Am. Chem. Soc.*, **107**, 8009 (1985); S. E. Woehler, R. J. Wittebort, S. M. Oh, D. N. Hendrickson, D. Inniss, and C. E. Strouse, *J. Am. Chem. Soc.*, **108**, 2938 (1986).
30. H. G. Jang, S. J. Geib, Y. Kaneko, M. Nakano, M. Sorai, A. L. Rheingold, B. Montez, and D. N. Hendrickson, *J. Am. Chem. Soc.*, **111**, 173 1989.
31. A. W. Hakin, Ph.D. Thesis, University of Leicester (1987).
32. I. M. Horn, Ph.D. Thesis, University of Leicester (1991).
33. Perkin-Elmer Handbook (1988).
34. R. bin Ali, Ph.D. Thesis, University of Leicester (1986).
35. N. Hallinen, P. McArdle, J. Burgess, and P. Guardado, *J. Organomet. Chem.*, **77**, 333 (1987).
36. A. I. Vogel, "*Textbook of Practical Organic Chemistry*", 4th edn. , Longman (1987), Chapter 2.
37. Y. Marcus, "*Ion Solvation*" , Wiley (1985).
38. B. Case and R. Parsons, *Trans. Faraday Soc.*, **63**, 1224 (1967); D. Feakins and P. Watson, *J. Chem. Soc.*, 473 (1963); C. F. Wells, *J. Chem. Soc., Faraday Trans. I*, **69**, 984 (1973).
39. M. H. Abraham, T. Hill, H. C. Ling, R. A. Schultz, and R. A. C. Watts, *J. Chem. Soc., Faraday Trans. I*, **80**, 489 (1984).

40. M. J. Blandamer, J. Burgess, B. Clark, P. P. Duce, A. W. Hakin, N. Gosal, S. Radulovic, P. Guardado, F. Sanchez, C. D. Hubbard, and E. A. Abu-Gharib, *J.Chem.Soc., Faraday Trans. I*, **82**, 1471 (1986).
41. S. J. Dickson and J. B. Hyne., *Canad.J.Chem.*, **49**, 2394 (1971).
42. T. Asano and W. J. le Noble, *Chem.Rev.*, **78**, 407 (1978).
43. W. J. le Noble, *Prog.Phys.Org.Chem.*, **5**, 207 (1967).
44. e.g. T. W. Swaddle, *Inorg.Chem.*, **19**, 3203 (1989).
45. H. Kelm and D. A. Parker, in "*High Pressure Chemistry*", ed. H. Kelm, Reidel, Dordrecht 1978 p. 281.
46. J. Burgess and C. D. Hubbard, *J.Chem.Soc., Chem.Comm.*, 1482 (1983); *J.Am.Chem.Soc.*, **106**, 1717 (1984); J. Burgess and C. D. Hubbard, *Inorg.Chem.*, **27**, 2548 (1988).
47. J. Burgess, A. J. Duffield, and R. Sherry, *J.Chem.Soc., Chem.Comm.*, 350 (1980).
48. F. J. Millero, *Chem.Rev.*, **71**, 147 (1971).
49. A. Indelli and R. Zamboni, *J.Chem.Soc., Faraday Trans. I*, **68**, 1831 (1972).
50. K.Yoshitani, *Bull.Chem.Soc.Jpn.*, **58**, 2327 (1985); G.A.Bottomley, L.G.Glossop, and W.P.Staunton, *Aust.J.Chem.*, **32**, 699 (1979); G.Wada, E.Nagao, N.Kawamura, and K.Kinamoto, *Bull.Chem.Soc.Jpn.*, **51**, 1937 (1978); K.Kurotaki and S.Kawamura, *J.Chem.Soc., Faraday Trans. I*, **77**, 217 (1981); F.Kawaizumi, K.Matsumoto, and H.Nomura, *J.Phys.Chem.*, **87**, 3161 (1983); Y.Kitamura, S.Nariyuki, and K.Yoshitani, *Inorg.Chem.*, **24**, 3021 (1985).

51. D. A. Palmer and H. Kelm, *Aus.J.Chem.*, 32, 1415 (1979).
52. M. Kotowski and R. van Eldik in *"Inorganic High Pressure Chemistry"*, ed. R. van Eldik, Elsevier, Amsterdam (1986), chap 4.
53. O. Redlich and D. M. Meyer, *Chem.Rev.*, 64, 221 (1964).
54. M. Kotowski and R. van Eldik, *Coord.Chem.Rev.*, 93, 19 (1989); R. van Eldik, T. Asano, and W. J. Le Noble, *Chem.Rev.*, 89, 549 (1989).
55. G. Stochel and R. van Eldik, *Inorg.Chem.*, 29, 2075 (1990).
56. e.g. C. R. Johnson and R. E. Shepperd, *Inorg.Chem.*, 22, 2439 (1983).
57. M. L. Myrick, R. L. Blakley, M. K. DeArmond, and M. L. Arthur, *J.Am.Chem.Soc.*, 110, 1325 (1988).
58. S. J. Milder, *Inorg.Chem.*, 28, 868 (1988).
59. F. M. van Meter and H. M. Neumann, *J.Am.Chem.Soc.*, 98, 1382 (1976).
60. M. J. Blandamer, J. Burgess, and T. Digman, *Transition Met.Chem.*, 10, 274 (1985).
61. H. Saito, J. Fujita, and K. Saito, *Bull.Chem.Soc.Jpn.*, 41, 863 (1968).
62. R. bin Ali, P. Banerjee, J. Burgess, and A. E. Smith, *Transition Met.Chem.*, 13, 107 (1988).
63. J. Bjerrum, A. W. Adamson and O. Bostrup, *Acta Chem.Scand.*, 10, 329 (1956).
64. M. Kotowski, R. van Eldik, R. bin Ali, J. Burgess and S. Radulovic, *Inorg.Chim.Acta*, 131, 225 (1987).

65. R. bin Ali, J. Burgess, M. Kotowski and R. van Eldik, *Transition Met.Chem.*, 12, 230 (1987).
66. J. Burgess, S. Radulovic, and F. Sanchez, *Transition Met.Chem.*, 12, 529 (1987).
67. A. Al-Alousy and J. Burgess, *Inorg.Chim.Acta*, 169, 167 (1990).
68. M. J. Blandamer and J. Burgess, *Transition Met.Chem.*, 13, 1 (1988).
69. A. A. Schilt, *J.Am.Chem.Soc.*, 82, 3000 (1960).
70. V. L. Goedken, *J.Chem.Soc., Chem.Comm.*, 207 (1972).
71. G. C. Christoph and V. L. Goedken, *J.Am.Chem.Soc.*, 95, 3869 (1973).
72. J. E. Figard and J. D. Petersen, *Inorg.Chem.*, 17, 1059 (1978).
73. J. Burgess and M. S. Patel, *Inorg.Chim.Acta*, 170, 241 (1990).
74. M. J. Blandamer, J. Burgess, and A. J. Duffield, *J.Chem.Soc., Dalton Trans.*, 1 (1980).
75. M. J. Blandamer and J. Burgess, *manuscript in preparation*.
76. E. G. McRae, *J.Phys.Chem.*, 61, 562 (1957).
77. E. S. Dodsworth and A. B. P. Lever, *Inorg.Chem.*, 29, 499 (1990).
78. B. S. Brunshwig, S. Ehrenson and N. Sutin *J.Phys.Chem.*, 90, 3657 (1986).
79. V. Gutmann and E. Wyckera, *Inorg.Nucl.Chem.Lett.*, 2, 257 (1966); U. Mayer, *Pure Appl.Chem.*, 41, 291 (1975).
80. U. Mayer, V. Gutmann, and W. Gerger, *Monatsh.Chem.*, 106, 1235 (1975); U. Mayer, W. Gerger, and V. Gutmann, *Monatsh.Chem.*, 108, 489 (1977).

81. C. Creutz and M. H. Chou, *Inorg.Chem.*, 26, 2995 (1987).
82. H. E. Toma and M. S. Takasugi, *J.Soln.Chem.*, 12, 547 (1983).
83. J. R. Winkler and N. Sutin, *Inorg.Chem.*, 26, 221 (1987).
84. J. R. Winkler, C. Creutz, and N. Sutin, *J.Am.Chem.Soc.*, 109, 3470 (1987).
85. K. Shinozaki, Y. Kaizu, H. Hirai, and H. Kobayashi, *Inorg.Chem.*, 28, 3675 (1989).
86. A. Horvath and Zs. Uzonyi, *Inorg.Chim.Acta*, 170, 1 (1990).
87. R. bin Ali and J. Burgess, *manuscript in preparation*.
88. A. A. Schilt, *J.Am.Chem.Soc.*, 85, 904 (1963).
89. For a more detailed discussion see J. Burgess and E. Pelizzetti, *Prog.React.Kinet.*, in press
90. K. Dimroth, C. Reichardt, T. Siepmann, and F. Bohlmann, *Annalen*, 1, 661 (1962).
91. J. G. Dawber, J. Ward, and R. A. Williams., *J.Chem.Soc., Faraday Trans. I*, 84, 713 (1988).
92. B. G. Cox, R. Natarajan, and W. E. Waghorne, *J.Chem.Soc., Faraday Trans. I*, 75, 1780 (1979).
93. See Ref. [80B].
94. J. R. Haak and J. B. F. N. Engberts, *Rec.Trav.Chim.*, 105, 307 (1986).
95. R. Willstaetter and A. Pfannenstiel, *Ber.Dtsch.Chem.Ges.*, 38, 2348 (1905).
96. L. H. Staal, D. J. Stufkens and A. Oskam, *Inorg.Chim.Acta*, 26, 255 (1978).

97. P. C. Servas, H. K. van Dijk, T. L. Snoeck, D. J. Stufkens, and A. Oskam, *Inorg.Chem.*, 24, 4494 (1985).
98. A. B. P. Lever, “*Inorganic Electronic Spectroscopy*” , Elsevier, Amsterdam, 1984, p. 208.
99. M. Suzuki, S. Tokura, M. Suhara, and A. Uehara, *Chem.Lett.*, 477 (1988).
100. H. tom Dieck and I. W. Renk, *Angew.Chem., Int.Ed.Engl.*, 9, 793 (1970).
101. J. Reinhold, R. Benedix, P. Birner, and H. Hennig, *Inorg.Chim.Acta*, 33, 209 (1979).
102. L. F. Warren, *Inorg.Chem.*, 16, 2814 (1977).
103. G. Milazzo, S. Caroli, V. K. Sharma, “*Tables of Standard Electrochemical Potentials*” , Wiley-Interscience, New York (1978).
104. A. B. P. Lever, *Inorg.Chem.*, 29, 1271 (1990), see ref. [110].
105. T. Saji, S. Aoyagui, *J.Electroanal.Chem.Interfacial Electrochem.*, 60, 1 (1975).
106. S. J. Amer, G. Sadler, P. M. Henry, G. Ferguson, and B. L. Ruhl, *Inorg.Chem.*, 24, 1517 (1985).
107. U. Sinha, M. D. Lowery, W. S. Hammack, D. N. Hendrickson, and H. G. Drickamer, *J.Am.Chem.Soc.*, 109, 7340 (1987).
108. Y. Kuroda, M. Goto and T. Saki, *Bull.Chem.Soc.Jpn.*, 60, 3917 (1987).
109. A. J. Duffield, Ph.D. Thesis, University of Leicester (1980).
110. L. Christiansen, D. N. Hendrickson, H. Toftlund, S. R. Wilson and C. L. Xie, *Inorg.Chem.*, 25, 2813 (1986).

111. CRC "*Handbook of Chemistry and Physics*" , 62nd. edn. , ed. R. C. Weast, CRC Press, Boca Raton, Florida (1981/1982); L. Pauling, "*The Nature of the Chemical Bond*" , 2nd. edn., Cornell University Press, Ithaca, NY, 1948; B. R. Eggins, "*Chemical Structure and Reactivity*" , Macmillan, London, 1972; M. F. C. Ladd, "*Structure and Bonding in Solid State Chemistry*" , Ellis Horwood, Chichester, 1979.
112. A. Al-Alousy, Ph.D. Thesis, University of Leicester (1990).
113. Y. Kuroda, N. Tanaka, M. Goto and T. Saki, *Inorg.Chem.*, 28, 997 (1989).
114. M. E. Garcia Posse, M. A. Juri, P. J. Aymonino, O. E. Piro H. A. Negri and E. E. Castellano, *Inorg.Chem.*, 23, 948 (1984).
115. L. Johansson, M. Molund and A. Oskarson, *Inorg.Chim.Acta*, 31, 117 (1978); A. Zalkin, D. H. Templeton and T. Ueki, *Inorg.Chem.*, 12, 1641 (1973).
116. M. J. Blandamer, J. Burgess, J. Fawcett, S. Radulovic, and D. R. Russell, *Transition Met.Chem.*, 13, 120 (1988).
117. S. Radulovic, Ph.D. Thesis, University of Leicester (1988).
118. S. Peng, C. Chen, D. Liaw, C. Chen and Y. Wang, *Inorg.Chim.Acta*, *L31* (1985).
119. G. Gallois, J-A. Real, C. Hauw, and J. Zarembowitch, *Inorg.Chem.*, 29, 1152 (1990).
120. B. S. Brunschwig, C. Creutz, D. H. Macartney, T-K. Sham, and N. Sutin, *Faraday Discuss.Chem.Soc.*, 74, 113 (1982).
121. S. K. Doorn and J. T. Hupp, *J.Am.Chem.Soc.*, 111, 4704 (1989).

122. R. L. Blackbourn and J. T. Hupp, *Inorg.Chem.*, 28, 3786 (1989).
123. J. C. Curtis, R. L. Blackbourn, K. S. Ennix, S. Hu, J. A. Roberts, and J. T. Hupp, *Inorg.Chem.*, 28, 3791 (1990).
124. J. T. Hupp, *J.Am.Chem.Soc.*, 112, 1563 (1990).
125. T. Swaddle in “*Inorganic High Pressure Chemistry*”, ed. R. van Eldik, Elsevier, Amsterdam (1986) p. 280.
126. P. Braun and R. van Eldik, *J.Chem.Soc., Chem.Comm.*, 1349 (1985).
127. J. Burgess and C. D. Hubbard, *Inorg.Chim.Acta*, 64, L71 (1982).
128. R. van Eldik, *Inorg.Chem.*, 21, 2501 (1982).
129. R. van Eldik and H. Kelm, *Inorg.Chim.Acta*, 73, 91 (1983).
130. L. Spiccia and T. W. Swaddle, *Inorg.Chem.*, 26, 2265 (1987).
131. M. J. Blandamer, J. Burgess, P. P. Duce, and R. I. Haines, *J.Chem.Soc., Dalton Trans.*, 2442 (1980).
132. J. Burgess and R. H. Prince, *J.Chem.Soc. A*, 211 (1970).
133. J. Burgess, *J.Chem.Soc., Dalton Trans.*, 203 (1972).
134. D. R. Stranks, *Pure Appl.Chem.*, 38, 303 (1974).
135. M. J. Blandamer, J. Burgess, M. Balon, P. Guardado, and A. Maestre, *Transition Met.Chem.*, 13, 313 (1988).
136. J. K. Hovey and P. R. Tremaine, *J.Phys.Chem.*, 89, 554 (1985).
137. L. G. Hepler, *Canad.J.Chem.*, 56, 1871 (1978).

138. D. Soria, M. L. De Castro, and H. L. Chum, *Inorg.Chim.Acta*, 42, 121 (1980).
139. N. S. Gosal, Ph.D. Thesis, University of Leicester, 1984.
140. R. bin Ali, M. J. Blandamer, J. Burgess, P. Guardado, and F. Sanchez, *Inorg.Chim.Acta*, 131, 59 (1987)
141. P. Guardado and R. van Eldik, *Inorg.Chem.*, 29, 3473 (1990).
142. J. Burgess, Ph.D. Thesis, University of Cambridge (1963).
143. J. Burgess, *J.Chem.Soc. A* , 2114 (1970).
144. W. J. Stratton and D. H. Busch, *J.Am.Chem.Soc.*, 80, 3191 (1958).
145. W. J. Stratton and D. H. Busch, *J.Am.Chem.Soc.*, 82, 4834 (1960).
146. W. J. Stratton, *Inorg.Chem.*, 9, 517 (1970).
147. A. G. Torres, M. Valcarcel, and F. Pino, *Talanta*, 20, 919 (1973).
148. M. Valcarcel, D. P. Bendito and F. Pino, *Inf.Quim.Anal.*, 25, 39 (1971).
149. I. Bertini, C. Owens, C. Luchinat, and R. S. Drago, *J.Am.Chem.Soc.*, 109, 5208 (1987); C. Owens, R. S. Drago, I. Bertini, C. Lucinat, and L. Banci, *J.Am.Chem.Soc.*, 108, 3298 (1986); C. Benelli, A. Dei, and D. Gatteschi, *Inorg.Chem.*, 21, 1284 (1982); A. Dei, D. Gatteschi, and E. Piergentili, *Inorg.Chem.*, 18, 89 (1979).
150. D. Onaggo, J. M. Hook, D. Rae, and H. A. Goodwin, *Inorg.Chim.Acta*, 173, 19 (1990).
151. D. L. Elvidge, Ph.D. Thesis, University of Leicester (1989).

152. M. J. Blandamer, J. Burgess, D. L. Elvidge, P. Guardado, A. W. Hakin, L. J. S. Prouse, S. Radulovic and D. R. Russell, *Transition Met.Chem.*, 16, 76 (1991).
153. A. Al-Alousy, D. L. Elvidge and J. Burgess, *manuscript in preparation*.
154. P. D. W. Boyd, M. Gerloch, and G. M. Sheldrick, *J.Chem.Soc., Dalton Trans.*, 1097 (1974).
155. E. Constable, "*Ligand Reactivity*" , Ellis Horwood, (1990).
156. B. S. Serr, K. A. Anderson, C. M. Elliot, and O. P. Anderson, *Inorg.Chem.*, 27, 4499 (1988).
157. J. A. Weil and A. G. Sykes, *Prog.Inorg.Chem.*, 13, 1 (1970).
158. M. B. Robin and P. Day, *Adv.Inorg.Chem.Radiochem.*, 10, 247 (1967).
159. C. Creutz, *Prog.Inorg.Chem.*, 30, 1 (1983).
160. eg. K. J. Brewer, W. R. Murphy, and J. D. Petersen, *Inorg.Chem.*, 26, 3376 (1987).
161. S. J. Lippard, *Angew.Chem.Int.Ed. Engl.*, 27, 344 (1988); B. S. Snyder, G. S. Patterson, A. J. Abrahamson, and R. H. Holm, *J.Am.Chem.Soc.*, 111, 5214 (1989).
162. D. W. Margerum, *J.Am.Chem.Soc.*, 79, 2728 (1957); J. Burgess and R. H. Prince, *J.Chem.Soc.*, 6061 (1965).
163. D. W. Clack and R. D. Gillard, *Transition Met.Chem.*, 10, 419 (1985).
164. M. J. Blandamer, J. Burgess, A. W. Hakin, P. Guardado, S. Nuttall, and S. Radulovic, *J.Chem.Soc., Faraday Trans. I*, 83, 559 (1987); M. J. Blandamer,

- B. Briggs, J. Burgess, D. Elvidge, P. Guardado, A. W. Hakin, S. Radulovic, and C. D. Hubbard, *J.Chem.Soc., Faraday Trans. I*, 84, 2703 (1988); M. J. Blandamer, B. Briggs, J. Burgess, P. Guardado, S. Radulovic, and C. D. Hubbard, *J.Chem.Soc., Faraday Trans. I*, 84, 1243 (1988).
165. M. J. Blandamer, J. Burgess, B. Clark, P. P. Duce, and J. M. W. Scott, *J.Chem.Soc., Faraday Trans. I*, 80, 739 (1984).
166. N. Serpone, G. Ponterini, M. A. Jamieson, F. Boletta, and M. Maestri, *Coord.Chem.Rev.*, 50, 209 (1983).
167. P. Lay, *Inorg.Chem.*, 23, 45 (1984) and refs. therein.
168. R. D. Gillard, *Coord.Chem.Rev.*, 16, 67 (1975).
169. M. J. Blandamer, J. Burgess, P. P. Duce, K. S. Payne, R. Sherry, and P. Wellings, *Transition Met.Chem.*, 9, 163 (1984).
170. E. C. Constable, *Polyhedron*, 8, 83 (1989); J. A. A. Sagues, R. D. Gillard, and P. A. Williams, *Transition Met.Chem.*, 14, 110 (1989).
171. D. W. Clack, L. A. P. Kane-Maguire, D. W. Knight, and P. A. Williams, *Transition Met.Chem.*, 5, 376 (1980); E. C. Constable and C. E. Housecroft, *Transition Met.Chem.*, 13, 19 (1988); D. W. Clack and R. D. Gillard, *Inorg.Chim.Acta*, 141, 37 (1988).
172. J. W. Bunting, *Adv.Heterocyclic Chem.*, 25, 1 (1979).
173. R. D. Gillard, C. T. Hughes, and P. A. Williams, *Transition Met.Chem.*, 1, 51 (1976); M. J. Blandamer, J. Burgess, and P. Wellings, *Transition Met.Chem.*, 4, 95 (1979).

174. F. Basolo and R. G. Pearson, "*Mechanisms of Inorganic Reactions*", Edn. 1, Wiley, NY, 1957 p. 152.
175. H. L. Chum and M. Rock, *Inorg.Chim.Acta*, 37, 113 (1979).

Appendix A

Crystallographic Data for

the $K_2[Fe(CN)_4(en)] \cdot 3H_2O$ Complex

Bond angles and lengths for the $K_2[Fe(CN)_4(en)] \cdot 3H_2O$ complex.

Bond lengths

N(1)—Fe	2.067(11)	N(2)—Fe	2.083(10)
C(3)—Fe	1.911(11)	C(4)—Fe	1.917(12)
C(5)—Fe	1.878(13)	C(6)—Fe	1.921(11)
H(31)—N(1)	1.080(0)	H(32)—N(1)	1.080(0)
C(1)—N(1)	1.468(18)	H(41)—N(2)	1.080(0)
H(42)—N(2)	1.080(0)	C(2)—N(2)	1.450(19)
N(3)—C(3)	1.133(13)	N(4)—C(4)	1.128(14)
N(5)—C(5)	1.164(16)	N(6)—C(6)	1.161(13)
H(11)—C(1)	1.080(0)	H(12)—C(1)	1.080(0)
C(2)—C(1)	1.449(19)	H(21)—C(2)	1.080(0)
H(22)—C(2)	1.080(0)	H(1)—O(1)	0.939(0)
H(2)—O(1)	0.945(0)	H(3)—O(2)	1.16(11)
H(4)—O(2)	0.77(10)	H(5)—O(3)	0.840(0)
H(6)—O(3)	0.885(0)		

Bond Angles

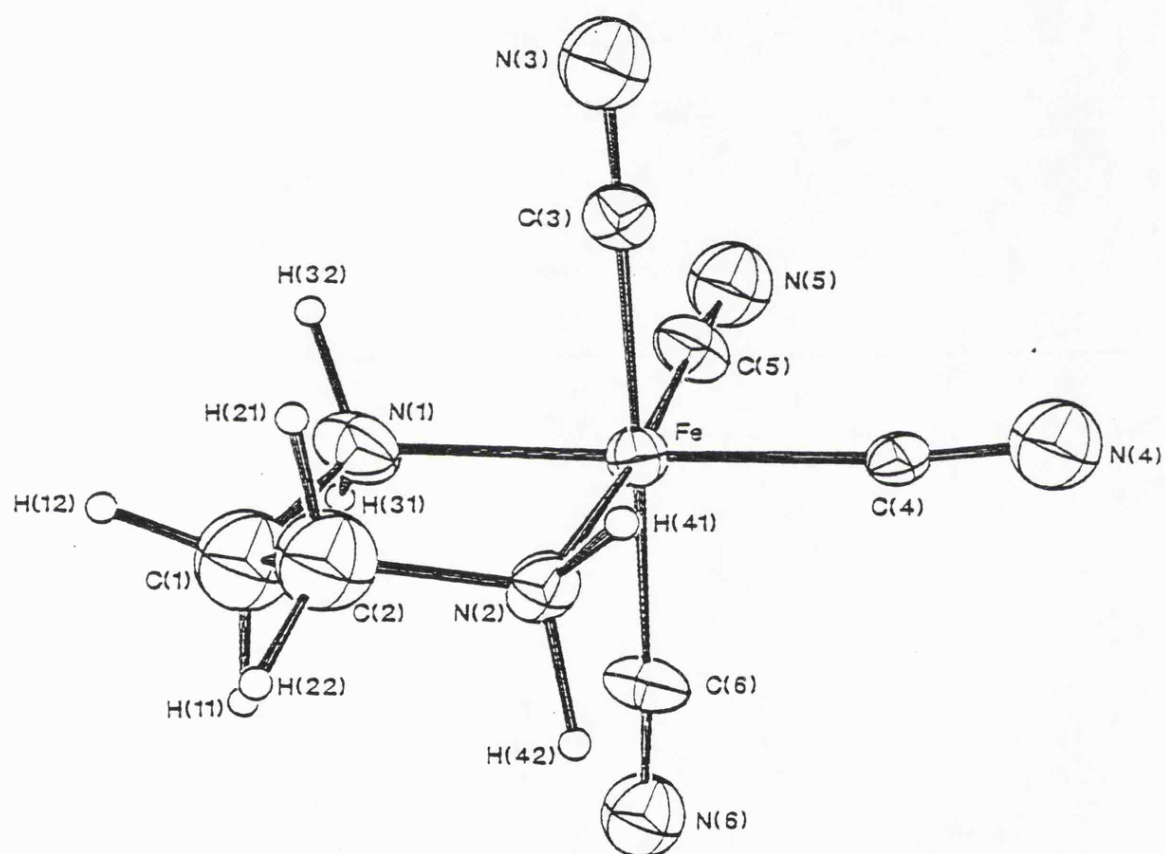
N(2)—Fe—N(1)	82.3(3)	C(3)—Fe—N(1)	88.7(5)
C(3)—Fe—N(2)	88.3(4)	C(4)—Fe—N(1)	173.8(5)
C(4)—Fe—N(2)	92.7(4)	C(4)—Fe—C(3)	87.5(5)
C(5)—Fe—N(1)	92.9(5)	C(5)—Fe—N(2)	175.2(5)
C(5)—Fe—C(3)	90.6(5)	C(5)—Fe—C(4)	92.0(5)
C(6)—Fe—N(1)	89.7(5)	C(6)—Fe—N(2)	90.4(4)
C(6)—Fe—C(3)	178.0(5)	C(6)—Fe—C(4)	94.0(5)
C(6)—Fe—C(5)	90.6(5)	H(31)—N(1)—Fe	109.5(3)
H(32)—N(1)—Fe	109.3(3)	H(32)—N(1)—H(31)	109.5(0)
C(1)—N(1)—Fe	109.4(8)	C(1)—N(1)—H(31)	110.0(7)
C(1)—N(1)—H(32)	109.1(8)	H(41)—N(2)—Fe	109.4(3)
H(42)—N(2)—Fe	109.4(3)	H(42)—N(2)—H(41)	109.5(0)
C(2)—N(2)—Fe	109.2(7)	C(2)—N(2)—H(41)	110.1(7)
C(2)—N(2)—H(42)	109.2(7)	N(3)—C(3)—Fe	178.8(10)
N(4)—C(4)—Fe	174.0(10)	N(5)—C(5)—Fe	176.3(11)
N(6)—C(6)—Fe	176.5(12)	H(11)—C(1)—N(1)	108.9(8)

H(12)—C(1)—N(1)	109.0(8)	H(12)—C(1)—H(11)	109.5(0)
C(2)—C(1)—N(1)	111.6(13)	C(2)—C(1)—H(11)	108.9(8)
C(2)—C(1)—H(12)	109.0(10)	C(1)—C(2)—N(2)	111.5(14)
H(21)—C(2)—N(2)	109.0(7)	H(21)—C(2)—C(1)	108.9(8)
H(22)—C(2)—N(2)	109.0(7)	H(22)—C(2)—C(1)	109.0(9)
H(22)—C(2)—H(21)	109.5(0)	H(2)—O(1)—H(2)	101.6(0)
H(4)—O(2)—H(3)	93(9)	H(6)—O(3)—H(5)	97.8(0)

Non-bonded Contacts

K(1)...Fe	4.106	1, 0.0000, 0.0000, -1.0000
H(31)...Fe	2.632	H(32)...Fe 2.630
H(41)...Fe	2.646	H(42)...Fe 2.646
C(1)...Fe	2.905	C(2)...Fe 2.903
N(3)...Fe	3.045	N(4)...Fe 3.041
N(5)...Fe	3.041	N(6)...Fe 3.081
C(4)...K(1)	3.201	1, 0.0000, 0.0000, 1.0000
C(5)...K(1)	3.222	1, 0.0000, 0.0000, 1.0000
N(4)...K(1)	3.059	1, 0.0000, 0.0000, 1.0000
N(5)...K(1)	3.074	1, 0.0000, 0.0000, 1.0000
O(2)...K(1)	2.782	1, 0.0000, 0.0000, 1.0000
H(4)...K(1)	3.201	1, 0.0000, 0.0000, 1.0000
O(3)...K(1)	2.914	1, 0.0000, 0.0000, 1.0000
K(2)...K(1)	4.173	2, 0.0000, 0.0000, 0.0000
C(3)...K(1)	3.395	2, 0.0000, 1.0000, 0.0000
N(3)...K(1)	2.840	2, 0.0000, 1.0000, 0.0000
N(3)...K(1)	2.891	O(1)...K(2) 2.868
O(3)...K(2)	3.366	1, 0.0000, 0.0000, 1.0000
K(2)...K(2)	4.087	2, 0.0000, 0.0000, -1.0000
C(3)...K(2)	3.193	2, 0.0000, 0.0000, 0.0000
C(4)...K(2)	3.301	2, 0.0000, 0.0000, 0.0000
N(3)...K(2)	2.989	2, 0.0000, 0.0000, 0.0000
N(4)...K(2)	3.058	2, 0.0000, 0.0000, 0.0000
O(1)...K(2)	2.683	2, 0.0000, 0.0000, 0.0000
O(2)...K(2)	2.814	2, 0.0000, 0.0000, 0.0000
H(3)...K(2)	3.199	2, 0.0000, 0.0000, 0.0000
H(4)...K(2)	3.238	2, 0.0000, 0.0000, 0.0000
O(3)...K(2)	2.875	2, 0.0000, 0.0000, 1.0000

H(2)...K(2)	2.935	2, 0.0000, 0.0000, 0.0000
H(6)...K(2)	2.271	2, 0.0000, 0.0000, 1.0000
H(1)...K(2)	2.451	N(2)...N(1) 2.732
C(3)...N(1)	2.782	C(5)...N(1) 2.863
C(6)...N(1)	2.815	H(11)...N(1) 2.085
H(12)...N(1)	2.086	C(2)...N(1) 2.412
H(32)...H(31)	1.764	C(1)...H(31) 2.099
C(4)...H(31)	2.647	4, 1.0000, -1.0000, 0.0000
C(3)...H(32)	2.588	C(1)...H(32) 2.088
H(12)...H(32)	2.253	C(3)...N(2) 2.785
C(4)...N(2)	2.896	C(6)...N(2) 2.842
C(1)...N(2)	2.397	H(21)...N(2) 2.071
H(22)...N(2)	2.071	H(42)...H(41) 1.764
C(2)...H(41)	2.084	H(21)...H(41) 2.255
O(1)...H(41)	2.242	H(2)...H(41) 1.845
C(6)...H(42)	2.648	C(2)...H(42) 2.074
C(5)...H(42)	2.524	4, 1.0000, 0.0000, 0.0000
N(5)...H(42)	2.513	4, 1.0000, 0.0000, 0.0000
H(22)...H(42)	2.244	C(4)...C(3) 2.648
C(5)...C(3)	2.694	C(5)...C(4) 2.729
C(6)...C(4)	2.806	C(6)...C(5) 2.701
H(21)...C(1)	2.069	H(22)...C(1) 2.070
H(12)...H(11)	1.764	C(2)...H(11) 2.069
C(2)...H(12)	2.070	H(22)...H(21) 1.764
O(1)...N(4)	2.854	1, 0.0000, 0.0000, -1.0000
H(1)...N(4)	2.373	1, 0.0000, 0.0000, -1.0000
O(2)...N(5)	2.867	2, 0.0000, 1.0000, -1.0000
H(3)...N(5)	1.713	2, 0.0000, 1.0000, -1.0000
H(2)...N(6)	2.044	4, 1.0000, -1.0000, 0.0000
H(5)...N(6)	2.137	3, -1.0000, 0.0000, 1.0000
O(2)...N(6)	2.927	3, -1.0000, 0.0000, 1.0000
H(4)...N(6)	2.192	3, -1.0000, 0.0000, 1.0000
O(3)...N(6)	2.939	3, -1.0000, 0.0000, 1.0000
O(1)...N(6)	2.928	4, 1.0000, -1.0000, 0.0000
H(2)...H(1)	1.460	H(4)...H(3) 1.424
H(6)...H(5)	1.301	



Atom numbered diagram of $\text{K}_2[\text{Fe}(\text{CN})_4(\text{en})] \cdot 3\text{H}_2\text{O}$ complex.

Appendix B

Crystallographic Data for

the $H[Fe(CN)_4(bipy)].2H_2O$ Complex

Bond angles and lengths for the $\text{H}[\text{Fe}(\text{CN})_4(\text{bipy})]\cdot 2\text{H}_2\text{O}$ complex.

Bond lengths

N(1)—Fe	1.983(3)	N(2)—Fe	1.984(4)
C(1)—Fe	1.909(5)	C(2)—Fe	1.950(6)
C(3)—Fe	1.923(5)	C(4)—Fe	1.941(6)
H(1)—O(1)	1.01(6)	H(0)—O(1)	1.12(12)
H(3)—O(2)	0.68(4)	C(5)—N(1)	1.350(6)
C(9)—N(1)	1.348(6)	C(10)—N(2)	1.338(6)
C(14)—N(2)	1.343(6)	C(1)—N(3)	1.134(5)
C(2)—N(4)	1.145(6)	C(3)—N(5)	1.138(6)
C(4)—N(6)	1.145(6)	H(5)—C(5)	0.93(5)
C(6)—C(5)	1.366(7)	H(6)—C(6)	0.91(5)
C(7)—C(6)	1.367(8)	H(7)—C(7)	1.02(5)
C(8)—C(7)	1.364(8)	H(8)—C(8)	0.88(4)
C(9)—C(8)	1.383(7)	C(10)—C(9)	1.470(7)
C(11)—C(10)	1.385(7)	H(11)—C(11)	0.81(4)
C(12)—C(11)	1.370(9)	H(12)—C(12)	0.93(5)
C(13)—C(12)	1.343(9)	H(13)—C(13)	0.87(5)
C(14)—C(13)	1.369(8)	H(14)—C(14)	0.92(5)

Bond Angles

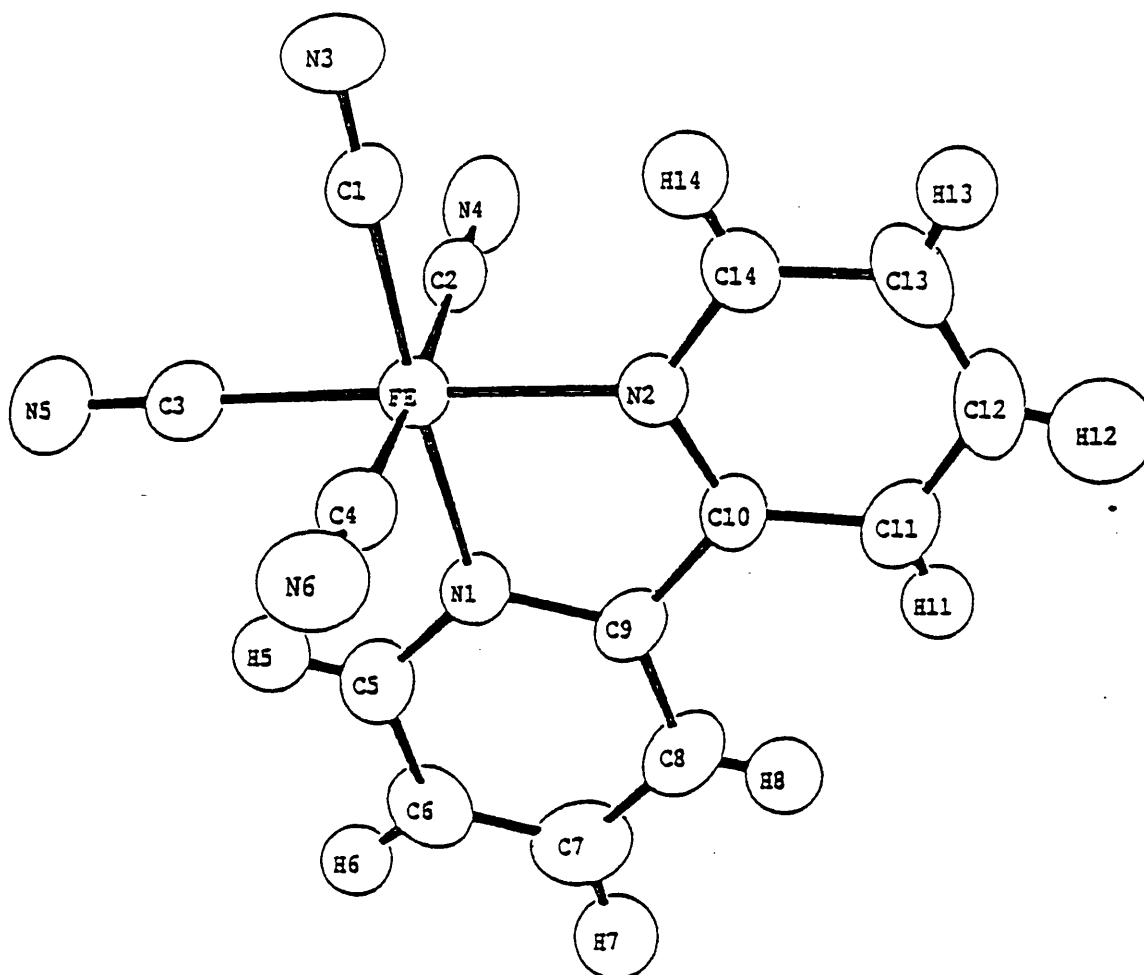
N(2)—Fe—N(1)	80.8(2)	C(1)—Fe—N(1)	176.5(2)
C(1)—Fe—N(2)	6.1(2)	C(2)—Fe—N(1)	91.3(2)
C(2)—Fe—N(2)	90.1(2)	C(2)—Fe—C(1)	87.1(2)
C(3)—Fe—N(1)	97.6(2)	C(3)—Fe—N(2)	178.3(2)
C(3)—Fe—C(1)	85.5(2)	C(3)—Fe—C(2)	90.5(2)
C(4)—Fe—N(1)	91.7(2)	C(4)—Fe—N(2)	92.3(2)
C(4)—Fe—C(1)	90.0(2)	C(4)—Fe—C(2)	176.5(2)
C(4)—Fe—C(3)	87.2(2)	H(0)—O(1)—H(1)	84(5)
C(5)—N(1)—Fe	125.9(4)	C(9)—N(1)—Fe	115.1(3)
C(9)—N(1)—C(5)	119.0(4)	C(10)—N(2)—Fe	115.7(3)
C(14)—N(2)—Fe	126.1(4)	C(14)—N(2)—C(10)	118.2(5)
N(3)—C(1)—Fe	178.1(5)	N(4)—C(2)—Fe	176.2(5)
N(5)—C(3)—Fe	178.3(5)	N(6)—C(4)—Fe	176.9(6)
H(5)—C(5)—N(1)	114.8(28)	C(6)—C(5)—N(1)	121.6(6)
C(6)—C(5)—H(5)	123.5(29)	H(6)—C(6)—C(5)	115.3(29)
C(7)—C(6)—C(5)	119.6(6)	C(7)—C(6)—H(6)	125.0(29)

H(7)—C(7)—C(6)	119.2(27)	C(8)—C(7)—C(6)	119.2(6)
C(8)—C(7)—H(7)	121.5(27)	H(8)—C(8)—C(7)	122(3)
C(9)—C(8)—C(7)	119.8(6)	C(9)—C(8)—H(8)	118(3)
C(8)—C(9)—N(1)	120.7(5)	C(10)—C(9)—N(1)	114.3(4)
C(10)—C(9)—C(8)	125.0(5)	C(9)—C(10)—N(2)	114.1(5)
C(11)—C(10)—N(2)	121.6(5)	C(11)—C(10)—C(9)	124.3(5)
H(11)—C(11)—C(10)	116(4)	C(12)—C(11)—C(10)	118.8(6)
C(12)—C(11)—H(11)	125(4)	H(12)—C(12)—C(11)	111(4)
C(13)—C(12)—C(11)	119.7(6)	C(13)—C(12)—H(12)	129(4)
H(13)—C(13)—C(12)	128(3)	C(14)—C(13)—C(12)	119.7(6)
C(14)—C(13)—H(13)	113(3)	C(13)—C(14)—N(2)	122.0(6)
H(14)—C(14)—N(2)	118(3)	H(14)—C(14)—C(13)	119(3)

Non-bonded Contacts

N(3)...Fe	3.043	N(4)...Fe	3.093
N(5)...Fe	3.061	N(6)...Fe	3.085
C(5)...Fe	2.983	H(5)...Fe	3.001
C(9)...Fe	2.833	C(10)...Fe	2.833
C(14)...Fe	2.979	H(14)...Fe	3.053
H(2)...O(1)	1.328	O(2)...O(1)	2.488
H(3)...O(1)	2.567	H(4)...O(1)	1.239
N(6)...O(1)	2.604	1, 0.0000, 0.0000, -1.0000	
N(3)...O(1)	2.564	H(2)...H(1)	1.415
O(2)...H(1)	2.534	H(4)...H(1)	1.339
N(6)...H(1)	2.505	1, 0.0000, 0.0000, -1.0000	
H(1)...H(1)	1.707	-1, 0.0000, 0.0000, 3.0000	
H(0)...H(1)	1.418	H(4)...H(2)	2.224
N(6)...H(2)	1.283	1, 0.0000, 0.0000, -1.0000	
C(4)...H(2)	2.425	1, 0.0000, 0.0000, -1.0000	
H(0)...H(2)	1.990	H(4)...O(2)	1.277
N(4)...O(2)	2.923	-1, 0.0000, 0.0000, 3.0000	
N(5)...O(2)	2.749	-2, 1.0000, 1.0000, 0.0000	
N(5)...H(3)	2.068	-2, 1.0000, 1.0000, 0.0000	
H(4)...H(3)	1.515	H(0)...H(4)	1.979
N(3)...H(0)	1.467	C(1)...H(0)	2.584
N(2)...N(1)	2.571	C(2)...N(1)	2.812
C(3)...N(1)	2.940	C(4)...N(1)	2.816
H(5)...N(1)	1.934	C(6)...N(1)	2.371

C(7)...N(1)	2.750	C(8)...N(1)	2.373
C(10)...N(1)	2.369	C(1)...N(2)	2.896
C(2)...N(2)	2.783	C(4)...N(2)	2.830
C(9)...N(2)	2.357	C(11)...N(2)	2.377
C(12)...N(2)	2.747	C(13)...N(2)	2.373
H(14)...N(2)	1.953	C(2)...C(1)	2.659
C(3)...C(1)	2.601	C(4)...C(1)	2.723
C(14)...C(1)	3.087	H(14)...C(1)	2.584
C(3)...C(2)	2.750	C(4)...C(3)	2.666
H(5)...C(3)	2.574	H(6)...C(5)	1.938
C(7)...C(5)	2.362	C(8)...C(5)	2.708
C(9)...C(5)	2.325	C(6)...H(5)	2.034
H(7)...C(6)	2.068	C(8)...C(6)	2.356
C(9)...C(6)	2.720	C(7)...H(6)	2.031
H(8)...C(7)	1.982	C(9)...C(7)	2.377
C(8)...H(7)	2.089	C(10)...C(8)	2.531
C(11)...C(8)	3.044	C(9)...H(8)	1.959
C(10)...H(8)	2.674	H(11)...H(8)	2.245
C(11)...C(9)	2.525	H(11)...C(9)	2.615
H(11)...C(10)	1.885	C(12)...C(10)	2.371
C(13)...C(10)	2.703	C(14)...C(10)	2.302
H(12)...C(11)	1.914	C(13)...C(11)	2.347
C(14)...C(11)	2.700	C(12)...H(11)	1.952
H(12)...H(11)	2.183	H(13)...C(12)	1.999
C(14)...C(12)	2.345	C(13)...H(12)	2.056
H(14)...C(13)	1.986	C(14)...H(13)	1.886
H(14)...H(13)	2.158		



Atom numbered diagram of $\text{H}[\text{Fe}(\text{CN})_4(\text{bipy})] \cdot 2\text{H}_2\text{O}$ complex.

Appendix C

Crystallographic Data for

the $[\text{Fe}_2(\text{pmk})_3]/\text{I}_4 \cdot 2\text{H}_2\text{O}$ Complex

Bond angles and lengths for the $[\text{Fe}_2(\text{pmk})_3](\text{I})_4 \cdot 3\text{H}_2\text{O}$ complex.

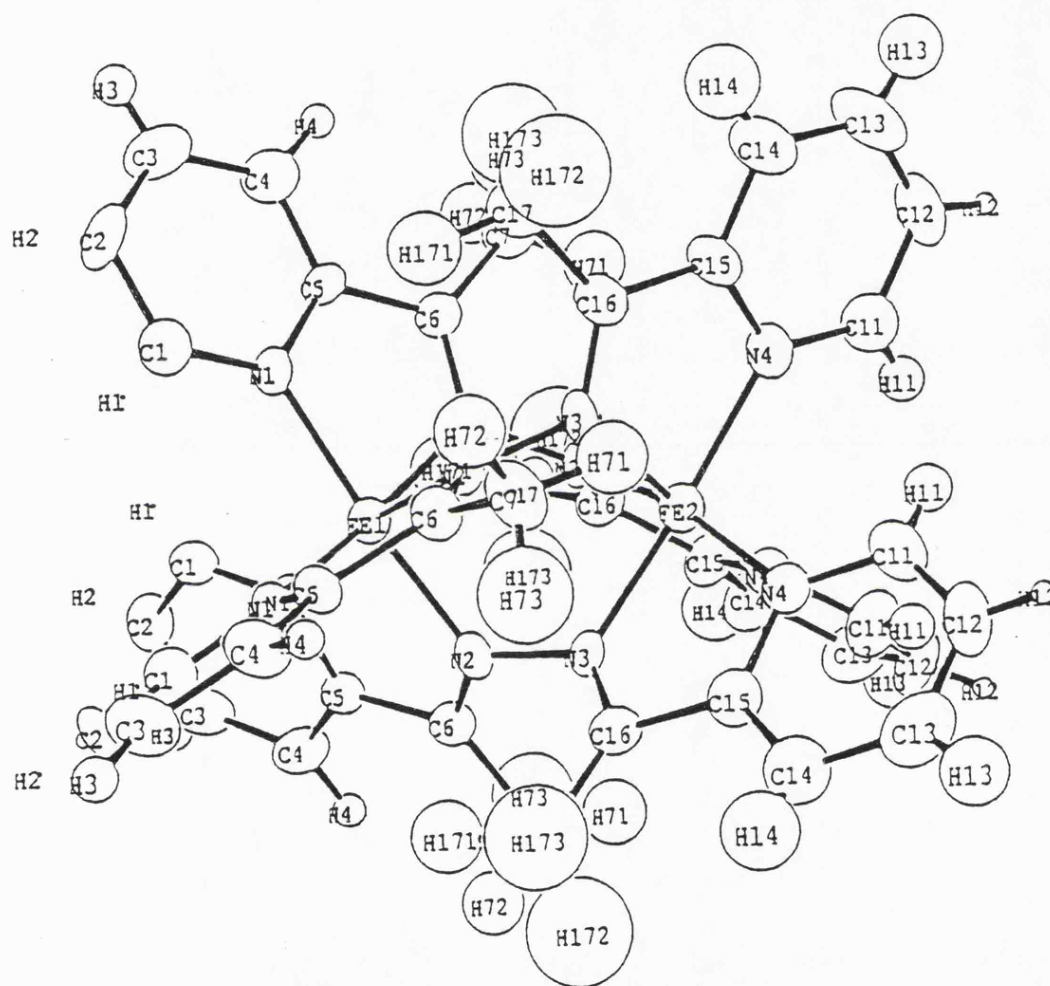
N(2)-Fe(1)-N(1)	78.7(3)	N(4)-Fe(2)-N(3)	79.5(3)
C(1)-N(1)-Fe(1)	125.5(7)	C(5)-N(1)-Fe(1)	114.4(6)
C(5)-N(1)-C(1)	120.0(9)	N(1)-Fe(1)-N(1)	96.4(3)
N(1)-Fe(1)-N(1)	96.4(3)	N(3)-N(2)-Fe(1)	115.6(6)
C(6)-N(2)-Fe(1)	120.9(7)	C(6)-N(2)-N(3)	121.4(8)
N(2)-Fe(1)-N(2)	91.6(3)	N(2)-Fe(1)-N(2)	91.6(3)
N(2)-N(3)-Fe(2)	117.2(6)	C(16)-N(3)-Fe(2)	119.5(7)
C(16)-N(3)-N(2)	120.6(8)	N(3)-Fe(2)-N(3)	90.2(3)
N(3)-Fe(2)-N(3)	90.2(3)	C(11)-N(4)-Fe(2)	126.5(8)
C(15)-N(4)-Fe(2)	114.8(7)	C(15)-N(4)-C(11)	118.7(9)
N(4)-Fe(2)-N(4)	96.3(3)	N(4)-Fe(2)-N(4)	96.3(3)
C(2)-C(1)-N(1)	120.4(10)	C(3)-C(2)-C(1)	120.6(11)
C(4)-C(3)-C(2)	118.4(11)	C(5)-C(4)-C(3)	117.9(10)
C(4)-C(5)-N(1)	122.6(9)	C(6)-C(5)-N(1)	114.6(9)
C(6)-C(5)-C(4)	122.8(9)	C(5)-C(6)-N(2)	111.3(9)
C(7)-C(6)-N(2)	126.1(9)	C(7)-C(6)-C(5)	122.5(9)
C(12)-C(11)-N(4)	121.5(11)	C(13)-C(12)-C(11)	118.9(12)
C(14)-C(13)-C(12)	120.1(12)	C(15)-C(14)-C(13)	116.7(11)
C(14)-C(15)-N(4)	124.0(10)	C(16)-C(15)-N(4)	113.8(10)
C(16)-C(15)-C(14)	122.2(10)	C(15)-C(16)-N(3)	112.0(9)
C(17)-C(16)-N(3)	125.5(10)	C(17)-C(16)-C(15)	122.5(10)

Bond lengths:

N(1)-Fe(1)	1.979(8)	N(2)-Fe(1)	1.926(8)
N(3)-Fe(2)	1.936(8)	N(4)-Fe(2)	1.972(8)
C(1)-N(1)	1.362(13)	C(5)-N(1)	1.351(12)
N(3)-N(2)	1.416(11)	C(6)-N(2)	1.288(12)
C(16)-N(3)	1.294(12)	C(11)-N(4)	1.341(13)
C(15)-N(4)	1.355(13)	C(2)-C(1)	1.410(14)
C(3)-C(2)	1.380(16)	C(4)-C(3)	1.443(15)
C(5)-C(4)	1.397(14)	C(6)-C(5)	1.445(13)
C(7)-C(6)	1.503(14)	C(12)-C(11)	1.424(16)
C(13)-C(12)	1.376(17)	C(14)-C(13)	1.418(16)
C(15)-C(14)	1.390(15)	C(16)-C(15)	1.468(14)
C(17)-C(16)	1.519(15)		

Non-bonded Contacts:

C(1)...I(1)	3.723	7, 1.0000, 0.0000, 0.0000
C(11)...I(1)	3.643	-10, 1.0000, 0.0000, 0.0000
Fe(2)...Fe(1)	3.472	N(3)...Fe(1) 2.842
C(1)...Fe(1)	2.984	C(5)...Fe(1) 2.821
C(6)...Fe(1)	2.814	N(2)...Fe(2) 2.875
C(11)...Fe(2)	2.972	C(15)...Fe(2) 2.822
C(16)...Fe(2)	2.809	N(2)...N(1) 2.476
C(2)...N(1)	2.406	C(3)...N(1) 2.803
C(4)...N(1)	2.411	C(6)...N(1) 2.353
N(1)...N(1)	2.952	5, 0.0000, 0.0000, 0.0000
N(2)...N(1)	2.859	5, 0.0000, 0.0000, 0.0000
N(1)...N(1)	2.952	9, 0.0000, 0.0000, 0.0000
C(5)...N(2)	2.259	C(7)...N(2) 2.490
C(16)...N(2)	2.355	C(17)...N(2) 2.905
N(2)...N(2)	2.762	5, 0.0000, 0.0000, 0.0000
N(3)...N(2)	2.718	5, 0.0000, 0.0000, 0.0000
N(2)...N(2)	2.762	9, 0.0000, 0.0000, 0.0000
N(4)...N(3)	2.499	C(6)...N(3) 2.360
C(7)...N(3)	2.918	C(15)...N(3) 2.291
N(3)...N(3)	2.744	5, 0.0000, 0.0000, 0.0000
N(4)...N(3)	2.875	5, 0.0000, 0.0000, 0.0000
N(3)...N(3)	2.744	9, 0.0000, 0.0000, 0.0000
C(17)...N(3)	2.503	C(12)...N(4) 2.412
C(13)...N(4)	2.790	C(14)...N(4) 2.424
N(4)...N(4)	2.938	5, 0.0000, 0.0000, 0.0000
N(4)...N(4)	2.938	9, 0.0000, 0.0000, 0.0000
C(16)...N(4)	2.364	C(3)...C(1) 2.424
C(4)...C(1)	2.786	C(5)...C(1) 2.350
C(4)...C(2)	2.425	C(5)...C(2) 2.752
C(5)...C(3)	2.433	C(6)...C(4) 2.495
C(7)...C(4)	3.011	C(7)...C(5) 2.585
C(13)...C(11)	2.411	C(14)...C(11) 2.776
C(15)...C(11)	2.318	C(14)...C(12) 2.421
C(15)...C(12)	2.734	C(15)...C(13) 2.391
C(16)...C(14)	2.502	C(17)...C(14) 3.028
C(17)...C(15)	2.618	



Atom numbered diagram of $[\text{Fe}_2(\text{pmk})_3]\text{I}_4 \cdot 3\text{H}_2\text{O}$.